Nanoscale polarizers for light manipulation and sensing applications

Course Coordinator:
Andrea Neviani

Supervisor:
Maria Guglielmina Pelizzo

Co-Supervisor:
Alain Jody Corso

Ph.D. candidate:
Zhuan Zhao

Abstract

Polarized light plays a significant role in various modern applications such as sunglasses, display technologies, navigation, and optical communications, which involve multiple disciplines, such as physics, chemistry, geology, and material science. Polarizers are among the most critical components for the control of polarization states, which can make a specific polarization state pass through while blocking other polarization states.

In this work, two different polarizers have been proposed and optimized for light manipulation. One is a wire gird reflecting polarizer. It works at H_I Ly-α 121.6 nm and aims to measure the magnetic field vector of Solar corona plasma. The optimal solution exhibits a polarization degree more than 99.9 % and TE-reflectance more than 0.2. The other is a TM-pass waveguide polarizer, working at 1.55 µm and aims to realize high-dense PLCs for optical fiber communications. The optimal solution realizes an extinction ratio as high as 60.7 dB and an insertion loss of 2.23 dB at a length of only 5 µm. To our knowledge, this extinction ratio is one of the highest values ever reported. In addition, all those optimal structures show a good tolerance in terms of free parameters, thus providing a large manufacturing possibility.

The fabrication plan for these optimal structures has been worked out through the collaboration between the Laboratory of Microfabrication, Institute of Physics, CAS and CNR-IFN, Padova. According to the existing equipment in these facilities, the specific manufacturing technical routes for each optimal structure are given.

Acknowledgements

Contents

1 Theory

1.1 Polarization of light

Light is an electromagnetic wave in which the transverse electric and transverse magnetic components are oscillate perpendicular to the direction of light propagation. According to the way that the electric fields oscillate in light waves, light falls into unpolarized and polarized light. Unpolarized light refers to the light wave vibrating in all possible directions, and it is difficult to visualize. In general, it is helpful to picture unpolarized light as a wave that has an average of half its vibrations in a horizontal plane and half of its vibrations in a vertical plane. Polarized light means the vibrations of a light wave having a specific orientation in the direction of propagation. In fact, polarization is the process of transforming unpolarized light to polarized light.

1.2 Types of polarization

Assuming that two perpendicular harmonic waves of the same frequency, traveling in the same direction of space, the resultant polarized light is under various states by examining its amplitude and phase. These polarized states can be classified into three types of polarization: linear polarization, circular polarization, and elliptical polarization [1].

1.2.1 Linear polarization

The two perpendicular optical waves can be expressed as

$$\overrightarrow{E}_x(z,t) = \widehat{i} E_{0x} \cos(kz - \omega t) \tag{1.1}$$

$$\overrightarrow{E}_y(z,t) = \widehat{i} E_{0y} \cos(kz - \omega t + \varepsilon) \tag{1.2}$$

where the ε is the phase difference between the two waves, ω is the frequency of light waves, k is the wave number, $(kz - \omega t)$ is the start phase. Both the two waves are traveling in the z-direction. A positive ε denotes that E_y lags E_x. Conversely, a negative ε denotes E_y leads E_x. The resultant wave is the vector sum of two orthogonal waves:

$$\overrightarrow{E}(z,t) = \overrightarrow{E}_x(z,t) + \overrightarrow{E}_y(z,t) \tag{1.3}$$

When $\varepsilon = \pm m\pi$ (m=1, 2, 3, ..., n), equation (1.3) can be further written as:

$$\overrightarrow{E} = \left(\widehat{i} E_{0x} \pm \widehat{j} E_{0y}\right) \cos(kz - wt) \tag{1.4}$$

where the amplitude of the resultant wave is $\left(\widehat{i} E_{0x} \pm \widehat{j} E_{0y}\right)$, and it is fixed. Such condition is linear polarized. One feature of the linear polarization is that the polarized wave oriented in a single plane, as is shown in Figure 3.1, where the

1

resultant linear polarized light is oscillating in the second and fourth quadrants. The tilt angle θ is determined by the amplitude of the original two waves:

$$\theta = \arctan \frac{E_{0y}}{E_{0x}} \tag{1.5}$$

The resultant wave can also oscillate in the first and third quadrants, mainly up to the oscillating direction of original two waves.
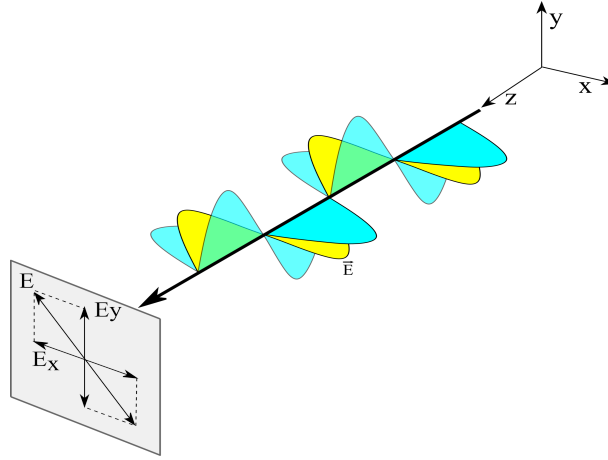
Figure 1.1: Linear polarized light vibrating in the second and fourth quadrants

1.2.2 Circular polarization

When the two orthogonal waves have same amplitudes (i. e. $E_{0x} = E_{0y} = E_0$), and their relative phase difference $\varepsilon = -\pi/2 \pm m\pi$ (m=1, 2, 3, ..., n). The consequent wave is written as:

$$\overrightarrow{E} = E_0[\hat{i}\cos(kz - \omega t) \pm \hat{j}\sin(kz - \omega t)] \tag{1.6}$$

where the amplitude of the resultant wave is a constant, but the oscillating direction is time-varying and not restricted in a single plane, which refers to circular polarization. According to the time-varied direction of $\overrightarrow{E}$, circular falls into right-circular polarization and left-circular polarization, as presented in the following two equations, respectively.

$$\overrightarrow{E} = E_0[\hat{i}\cos(kz - \omega t) + \hat{j}\sin(kz - \omega t)] \tag{1.7}$$

$$\overrightarrow{E} = E_0[\hat{i}\cos(kz - \omega t) - \hat{j}\sin(kz - \omega t)] \tag{1.8}$$

Figure 1.2 reports the case of right-circular polarization. The main feature is that the resultant vector $\overrightarrow{E}$ rotates clockwise along the light propagation.

2

Similarly, when the resultant vector E rotates counterclockwise, the wave is left-circular polarized. Two oppositely circular-polarized waves with the same amplitude can synthesize a linear polarized wave. For example, add the equations1.7 to 1.8 we can obtain

$$\overrightarrow{E} = 2E_0 \cos(kz - \omega t) \tag{1.9}$$

where has fixed amplitude and is therefore linear polarized.
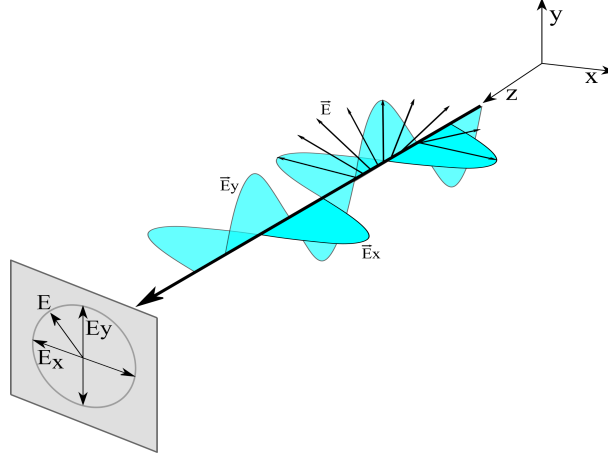
Figure 1.2: Right-circular polarized light

1.2.3   Elliptical polarization

Elliptical polarization refers to the vector $\overrightarrow{E}$ rotating and changing its amplitude at the same time. By combining the equations 1.1 and 1.2, we have

$$(\frac{E_y}{E_{0y}})^2 + (\frac{E_x}{E_{0x}})^2) - 2(\frac{E_x}{E_{0x}})\frac{E_y}{E_{0y}})\cos\varepsilon = \sin^2\varepsilon \tag{1.10}$$

The above equation represents an ellipse that makes an angle α with (E_x, E_y) coordinate system and has the property that

$$\tan 2\alpha = \frac{2E_{0x}E_{0y}\cos\varepsilon}{E_{0x}^2 - E_{0y}^2} \tag{1.11}$$

If here the $\varepsilon = \pm m\pi/2$ (m=1, 3, 5..., 2n-1) , we can obtain familiar form

$$\frac{E_y^2}{E_{0y}^2} + \frac{E_x^2}{E_{0x}^2} = 1 \tag{1.12}$$

This equation is a typical ellipse, if $E_{0x} = E_{0y} = E_0$, inducing to

$$E_y^2 + E_x^2 = E_0^2 \tag{1.13}$$

3

Where the equation represents a circle. The above equations explained that linear polarization and circular polarization are a special case of elliptical polarization. Elliptical polarization also includes right-elliptical polarization and left-elliptical polarization. Figure 1.3 reports the case of right-elliptical polarization. The main feature is that the endpoint of vector E travels out an ellipse perpendicular to the direction of light propagation.
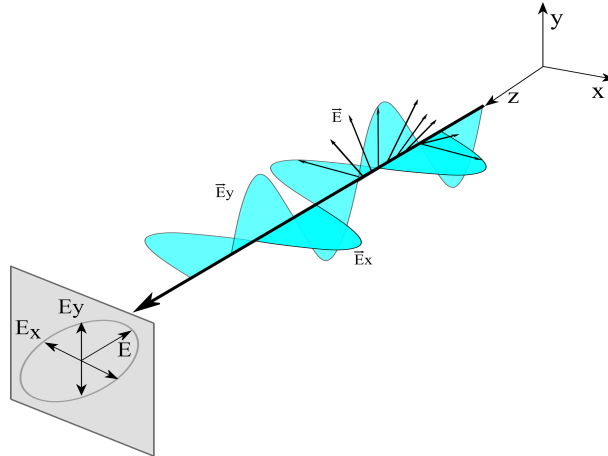
Figure 1.3: Elliptical polarization

1.3 Methods of polarization

The techniques to generate and manipulate the polarization are very important for many applications. A polarizer is a typical device that transfers the unpolarized light to polarized light, which comes in many different configurations. Light polarization is based on four main physical mechanisms: polarization by transmission, polarization by reflection, polarization by scattering, polarization by refraction.

1.3.1 Polarization by transmission

The employment of a Polaroid filter is the most prevalent way for transmission. Polaroid filters are made of special material that can block one of two planes of perpendicular electromagnetic waves. Figure 1.4 shows the basic transmission principle of a Polaroid filter. When the unpolarized light with two perpendicular electromagnetic waves propagates in the Polaroid filter, only one-half of the intensity passed through.

A Polaroid filter can realize polarization mainly due to the chemical composition of the filter material. The filter is regarded as long-chain molecules that are aligned within the filter in the same direction. The long-chain molecules are stretched over the filter during the manufacture, so each molecule is aligned

4

in the vertical direction. The waves oscillating in the vertical direction is absorbed by the filter when unpolarized light strikes it. The polarization axis of the filter is determined by the alignment of these molecules, which only allows vibrations of electromagnetic wave that are parallel to the axis to pass and block any vibrations that are perpendicular to the polarization axis. As a result, a Polaroid filter with long-chain molecules arranges horizontally with a vertical polarization axis. Such filter will prevent all horizontal vibrations while allowing vertical vibrations to pass through.

Unpolarized light   Polarioid filter   Polarized light
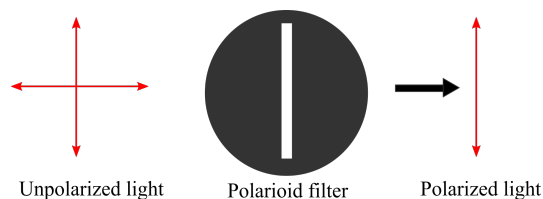
Figure 1.4: The diagram for transmitting one polarization component by using a Polaroid filter

1.3.2   Polarization by reflection

Polarized light can also be realized by reflection from non-metallic surfaces, such as snow, water, and glass. Figure 1.5 describes the phenomenon when a beam of unpolarized light incident on a glass surface. The incident beam has two vibrating components that are perpendicular and parallel to the glass surface, respectively. When it interacts with the glass surface, the component perpendicular to the surface is partially transmitted, while the component parallel to the surface is reflected. In particular, if the refracted ray and reflected ray produces an angle of 90°, the incident angle is called the Brewster angle.

When the incident light passes over the surface, it is absorbed temporarily by atoms in the second medium. Electrons in these atoms oscillate back and forth in the direction of the refracted ray's electric field vectors, which is perpendicular to the direction of the refracted light. The atoms re-emit the light, resulting in reflected and refracted beams. The electric field vectors in light correspond to the direction in which the electrons oscillated, and they must be perpendicular to the direction of wave propagation. When light enters at a Brewster angle the refracted wave has no electric field vectors parallel to the refracted beam, because the electrons don't oscillate in that direction. Similarly, the reflected wave also has no electric field vectors parallel to the reflected ray. The only possible direction is perpendicular to the medium plane, so the reflected ray is linearly polarized. The reflected light is completely polarized when incident angle is a Brewster angle, and the refractive angle and incident angle meet the laws:

$$\tan \theta_1 = \frac{n_1}{n_2} \tag{1.14}$$

where the n_1 is the refractive index in which the incident and reflected light

travel, n_2 is the refractive index of the medium. Hence, the amount of polarization highly depends on the refractive index of the medium involved.
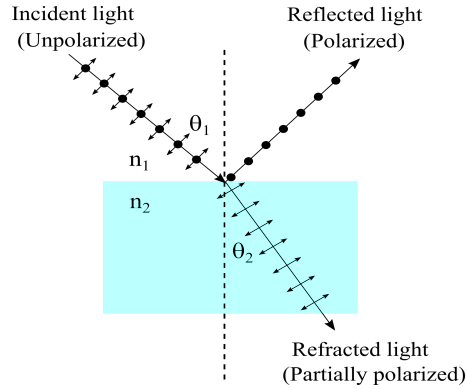
Figure 1.5: Polarization by reflection

1.3.3 Polarization by scattering

When a ray of unpolarized light travels through a medium, it undergoes scattering. A ray of light contains a number of photons, and the medium is composed of numerous atoms. When photons strike the atoms in the medium, the energy is transferred to the atom, which results in a vibration of electrons in the atoms. The vibrating electrons emit electromagnetic radiation in all possible directions. When these atoms strike neighboring atoms, the electrons there will re-emit the radiation with the same frequency as incident radiation. This process continues to spread across the medium. The scattering of light in the medium is caused by the absorption and emission of light radiation.
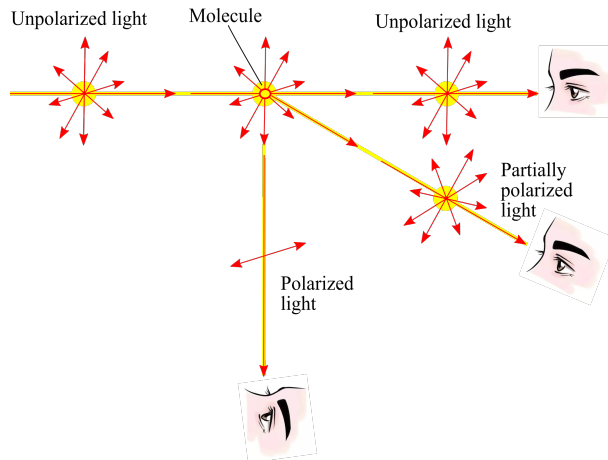
Figure 1.6: Emitted rays of light after scattering

The scattered light is composed of completely polarized light, partially polarized light, and completely unpolarized light, depending on the direction of the generated radiation. As is shown in Figure 1.6, an emitted ray of unpolarized light stroke the air molecules and then generates three different polarization states. The emitted rays that are parallel to the path of original rays are completely unpolarized, and in the perpendicular path of the original ways the emitted rays are completely polarized, while the part scattered in other directions are partially polarized. For example, the light we received from the Sun is partially polarized because it undergoes scattering when it reach Earth's atmosphere.

1.3.4 Polarization by refraction

Polarization also occurs in the refracted light. Refraction occurs when a beam of light passes from one material to another. The traveling path changes its direction at the surface between two materials; the refracted beam is polarized to some extent. In most conditions, the polarization occurs in the plane that is perpendicular to the surface.

When the refractive index depends on the incidence angle and polarization of light, it is called birefringent. Figure 1.7 shows the process of a beam passes through a birefringent material (i.e crystals). The original light is split into two beams upon entering the crystals. Two beams are formed because of two index planes in the medium and cause different speeds. Both the two beams are polarized; one is polarized in the direction parallel to the surface and the other in the direction perpendicular to the surface. If an object is viewed by looking through the crystals, two images can be seen. A polarizing filter can totally block one of the images because these two refractive rays are polarized with perpendicular orientation.
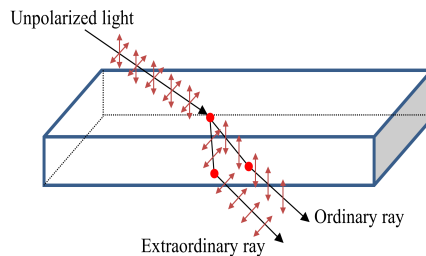
Figure 1.7: Polarization by birefringence

1.4 Fresnel Equations

When light incident from one substance to another substance, Fresnel equations are introduced, which describe the fraction of the incident energy transmitted or reflected at an interface. These properties depend on the difference in refractive index, the incident angle, and the polarization state of incident light.
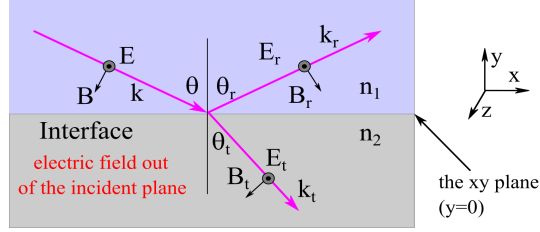
Figure 1.8: s polarization (TE mode)

Figure 1.8 reports a ray of light incident at the interface xz plane, resulting in reflected and transmitted rays since the different refractive index. Assuming that the incident wave expressed by

$$E = E_o e^{i(k \cdot r - wt)} \tag{1.15}$$

where the r is a boundary point, k is the direction of light propagation, which is determined by the direction of E× B. The vector E is perpendicular to the plane of incidence, while the vector B lies in the plane of incidence. In other words, here E field component is in the z-direction, which is in the plane of interface, B field component is in the plane of incidence. Under these conditions, the polarization mode is named transverse electric (TE) mode. The reflected and transmitted waves are expressed by the following two equations, respectively

$$E_r = E_{or} e^{i(k_r \cdot r - w_r t)} \tag{1.16}$$

$$E_t = E_{ot} e^{i(k_t \cdot r - w_t t)} \tag{1.17}$$

At the plane of interface xz, all the three waves exist simultaneously, an equation can reveal the relationship between the three waves, as follows

$$(k \cdot r - wt) = (k_r \cdot r - w_r t) = (k_t \cdot r - w_t t) \tag{1.18}$$

When the boundary point r equal to 0

$$w = w_r = w_t \tag{1.19}$$

So all frequencies are equal no matter the ray is transmitted or reflected. On the other hand, when t equal to 0, equation 1.18 is written as

$$(k - k_r) \cdot r = (k - k_t) \cdot r = (k_r - k_t) \cdot r = 0 \tag{1.20}$$

From the Equation 1.20, we know that k_r and k_t need to lie in the plane decided by vectors k and r. Hence, all three propagation vectors are coplanar in the xy plane. Consider the first two vectors in Equation 1.20, which reveal the relationship between the incident and reflected waves, they are also equivalent to

$$kr \sin \theta = k_r r \sin \theta_r \tag{1.21}$$

8

Since both two waves propagate in the same medium, the wavelength doesn't change, and so k = k_r, the law of reflection also can be obtained

$$\theta = \theta_r \tag{1.22}$$

The last two vectors of Equation 1.20 are equivalent to

$$k_r r \sin\theta_r = k_t r \sin\theta_t \tag{1.23}$$

Let $k_r = w/v_r = n_r w/c$ and $k_t = n_t w/c$, Equation 1.23 can be presented by Snell's law of refraction:

$$n_r \sin\theta_r = n_t \sin\theta_r \tag{1.24}$$

By considering Maxwell's equations at the boundary conditions, the component of E-field that lies in the xz plane is continuous as move across the plane of the interface, all the E-field components are in the z-direction, which is in the plane of the interface, the requirement for the electric field is

$$E + E_r = E_t \tag{1.25}$$

where the total field at the side of the incident boundary is a superposition of incident and reflected waves, and at the other side is a transmitted field alone. In terms of magnetic field components, which are governed by

$$B\cos - B_r \cos\theta = B_t \cos\theta_t \tag{1.26}$$

where the negative sign indicates the B_r component of the reflected beam is along the x direction. The case of transverse magnetic (TM) mode is depicted in Figure 1.9, where the vectors E are lie in the plane of incidence and the vectors B is perpendicular to the plane of incidence. A different notation is used for the reflected field, this leads to a difference in the signs of some equations. In TM modes, the electric field and magnetic field at the boundary conditions are written as

$$B + B_r = B_t \tag{1.27}$$

$$-E\cos + E_r \cos\theta = -E_t \cos\theta_t \tag{1.28}$$
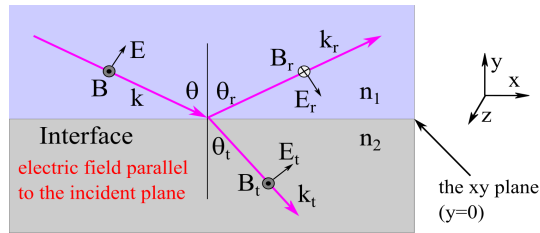
Figure 1.9: p polarization (TM mode)

In addition, there is a relationship between the electric field E and magnetic field B, which governed by

$$E = vB = (\frac{c}{n})B \tag{1.29}$$

where the n is the refractive index of the medium. n_1 and n_2 are the refractive index of the two mediums in Figure 1.8 and 1.9. For both the TE and TM modes, equation 1.25 through 1.28 can be rewrite as follows:

$$\text{TE}: \begin{cases} E + E_r = E_t \\ n_1 E \cos - n_1 E_r \cos\theta = n_2 E_t \cos\theta_t \end{cases} \tag{1.30}$$

$$\text{TM}: \begin{cases} n_1 E + n_1 E_r = n_2 E_t \\ -E \cos + E_r \cos\theta = -E_t \cos\theta_t \end{cases} \tag{1.31}$$

By eliminating E_t in each set of equations (i.e. TE and TM) and solving for the reflection coefficient, which is defined as r $= E_r/E$, follow expressions are obtained

$$\text{TE}: r = \frac{E_r}{E} = \frac{\cos\theta - n\cos\theta_t}{\cos\theta + n\cos\theta_t} \tag{1.32}$$

$$\text{TM}: r = \frac{E_r}{E} = \frac{n\cos\theta - \cos\theta_t}{n\cos\theta + \cos\theta_t} \tag{1.33}$$

where a relative refractive index $n = n_2/n_1$. According to Snell's law, $\sin\theta_t = n\sin\theta$, θ_t can be eliminated using

$$n\cos\theta_t = n\sqrt{1 - \sin^2\theta_t} = \sqrt{n^2 - \sin^2\theta}$$

The reflection coefficient for TE and TM mode can be rewritten as

$$\text{TE}: r = \frac{E_r}{E} = \frac{\cos\theta - \sqrt{n^2 - \sin^2\theta}}{\cos\theta + \sqrt{n^2 - \sin^2\theta}} \tag{1.34}$$

$$\text{TM}: r = \frac{E_r}{E} = \frac{n^2\cos\theta - \sqrt{n^2 - \sin^2\theta}}{n^2\cos\theta + \sqrt{n^2 - \sin^2\theta}} \tag{1.35}$$

If we eliminate E_r instead of E_t in the equation 1.30 and 1.31, transmission coefficient $t = E_t/E$ can be obtained, as follows

$$\text{TE}: t = \frac{E_t}{E} = \frac{2\cos\theta}{\cos\theta + \sqrt{n^2 - \sin^2\theta}} \tag{1.36}$$

$$\text{TM}: t = \frac{E_t}{E} = \frac{2n\cos\theta}{n^2\cos\theta + \sqrt{n^2 - \sin^2\theta}} \tag{1.37}$$

By observing the equations of reflection coefficient and transmission coefficient, we obtained the following relationship

$$\text{TM}: t = r + 1 \tag{1.38}$$

$$TM : nt = r + 1 \tag{1.39}$$

Equations 1.34 through 1.37 are the Fresnel equations.Reflection and transmission coefficient are defined as the ratio of reflected and transmitted electric field amplitudes to the incident electric field amplitude. Reflectance and transmittance are the reflected or transmitted energy power of the incident wave, respectively, defined by

$$R = \frac{P_r}{P_i} = r^2 = (\frac{E_r}{E})^2 \tag{1.40}$$

$$T = \frac{P_t}{P_i} = n(\frac{\cos \theta_t}{\cos \theta_i})t^2 \tag{1.41}$$

1.5   Optical function of the multilayer thin films

The optical functions of calculating a multilayer film are also based on Fresnel equations. Firstly, let's look at a ray of electromagnetic wave incident at an ideal interface without roughness, as is shown in Figure 1.10. The complex index of refraction $n = n + ik$ (where the n is the refractive index and k is the extinction coefficient) is given in two dissimilar materials as n_i and n_j. The incident wave has an electric field E_i with an incident angle θ_i with respect to the z axis. E_i' and E_j are the amplitude of reflected and transmitted electric fields, respectively. According to the Fresnel equations, reflection coefficient and transmission coefficient for s and p polarization are written as

$$TE : \frac{|E_i'|}{|E_i|} = \frac{n_i \cos \theta_i - n_j \cos \theta_j}{n_i \cos \theta_i + n_j \cos \theta_j} = r_{ij}^s \tag{1.42}$$

$$TE : \frac{|E_i'|}{|E_i|} = \frac{2n_i \cos \theta_i}{n_i \cos \theta_i + n_j \cos \theta_j} = t_{ij}^s \tag{1.43}$$

$$TM : \frac{|E_i'|}{|E_i|} = \frac{n_i \cos \theta_j - n_j \cos \theta_i}{n_i \cos \theta_j + n_j \cos \theta_i} = r_{ij}^p \tag{1.44}$$

$$TM : \frac{|E_i'|}{|E_i|} = \frac{2n_i \cos \theta_i}{n_i \cos \theta_j + n_j \cos \theta_i} = t_{ij}^p \tag{1.45}$$

Considering a ray of electromagnetic wave incident on a multilayer stack with a series of N layers and N+1 interface, as is shown in Figure 1.11, where the ith layer has thicknessd_i, optical constants n_i, and interfacial roughness σ. The area above the top layer and below the bottom layer are ambient and substrate, having optical constants n_a and n_s, respectively. In such a multilayer stack, reflection coefficient and transmission coefficient at the ith layer is given by [2]

$$r_i = \frac{r_{ij} + r_j e^{2i\beta_i}}{1 + r_{ij}r_j e^{2i\beta_i}} \tag{1.46}$$

$$t_i = \frac{t_{ij}t_j e^{2i\beta_i}}{1 + r_{ij}r_j e^{2i\beta_i}} \tag{1.47}$$

11
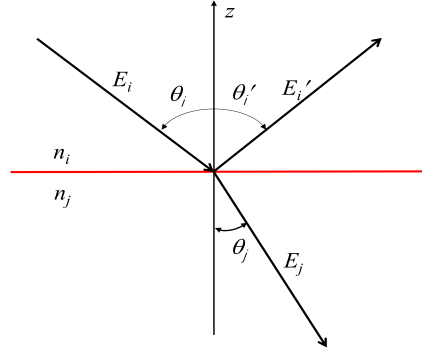
Figure 1.10: Diagram of a plane wave incident at the interface between two different materials
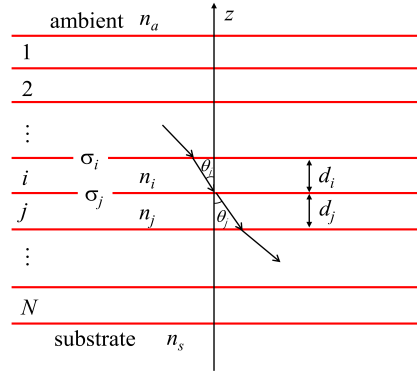
Figure 1.11: Diagram of a plane wave incident at a multilayer stack

where the $\beta = 2\pi d_i n_i \cos\theta_i / \lambda$, r_j and t_j are the net reflection and transmission coefficients of the jth interface, respectively. The procedure to calculate the total reflectance and transmittance is to apply equation 1.46 and 1.47, recursively, starting at the bottom layer. The reflectance and transmittance are given by

$$R = |r^2| \tag{1.48}$$

$$T = \mathrm{Re}\left\{ \frac{n_s \cos\theta_s}{n_a \cos\theta_a} \right\} |t|^2 \tag{1.49}$$

1.6 Polarized light propagates in two dimensional waveguides

The guided light in a waveguide is typically described by two propagating modes: TE (transverse electric) and TM (transverse magnetic) mode. TE mode refers

12

to the electric field that has no component in the direction of propagation, while TM mode refers to the magnetic field that has no component in the direction of propagation.
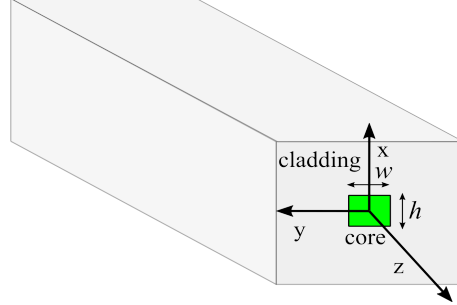
Figure 1.12: the cross section of dielectric waveguide with a three dimensional axis

In two dimensional-waveguides, light mainly confines in two dimensions (x and y-dimensions) and travels in the z-direction, as is reported in Figure 1.12, where the x axis is in the vertical direction, while y axis is in the horizontal direction. In such waveguides, the exact modes is difficult to compute since they are neither TE or TM mod es. All modes have a small $\overrightarrow{E}$ and $\overrightarrow{H}$ component in the direction of propagation.

To study the propagating modes in two-dimensional waveguides. Firstly, we introduced Maxwell's equation, the complex of Maxwell's equations are written as

$$\nabla \times \overrightarrow{E} = i\omega\mu_0 \overrightarrow{H} \tag{1.50}$$

$$\nabla \times \overrightarrow{H} = -i\omega\varepsilon_0 n^2(x)\overrightarrow{E} \tag{1.51}$$

where the μ_0 and ε_0 are the permittivity and permeability of free space, respectively, ω is the angular velocity. Combining the equations 1.50 and 1.51, we obtained

$$\nabla \times \nabla \times \overrightarrow{E} = \frac{\omega^2}{c^2} n^2(x)\overrightarrow{E} \tag{1.52}$$

where the c is light speed in the vacuum. On the other side, $\nabla \times \nabla \times \overrightarrow{E} = \nabla(\nabla \cdot \overrightarrow{E})$-$\nabla^2 \overrightarrow{E}$. In general, $\nabla \cdot \overrightarrow{E} \neq 0$, rather $\nabla[n^2(x)\overrightarrow{E}]=0$. If the refractive index is uniform in different waveguide regions, each region inside may assume $\nabla \cdot \overrightarrow{E} = 0$, we can obtain

$$-\nabla^2 \overrightarrow{E} = \frac{\omega^2}{c^2} n^2(x)\overrightarrow{E} \tag{1.53}$$

Similarly, we also can obtain

$$-\nabla^2 \overrightarrow{H} = \frac{\omega^2}{c^2} n^2(x)\overrightarrow{H} \tag{1.54}$$

13

The electrical field $\overrightarrow{E}$ and magnetic filed $\overrightarrow{H}$ are written as,

$$
\begin{aligned}
\overrightarrow{E}\left(x,y,z\right) &= \left\{\hat{x}E_x\left(x,y\right) + \hat{y}E_y\left(x,y\right) + \hat{z}E_z\left(x,y\right)\right\}e^{i\beta z}\\
&= \left\{\overrightarrow{E}_t\left(x,y\right) + \hat{z}E_z\left(x,y\right)\right\}e^{i\beta z}
\end{aligned}
\tag{1.55}
$$

$$
\begin{aligned}
\overrightarrow{H}\left(x,y,z\right) &= \left\{\hat{x}H_x\left(x,y\right) + \hat{y}H_y\left(x,y\right) + \hat{z}H_z\left(x,y\right)\right\}e^{i\beta z}\\
&= \left\{\overrightarrow{H}_t\left(x,y\right) + \hat{z}H_z\left(x,y\right)\right\}e^{i\beta z}
\end{aligned}
\tag{1.56}
$$

where the β is the propagation constant, and the transverse components of the fields have been defined as follows

$$
\overrightarrow{E}_t\left(x,y\right) = \hat{x}E_x\left(x,y\right) + \hat{y}E_y\left(x,y\right)
\tag{1.57}
$$

$$
\overrightarrow{H}_t\left(x,y\right) = \hat{x}H_x\left(x,y\right) + \hat{y}H_y\left(x,y\right)
\tag{1.58}
$$

Since finding an exact solution is complicated and time-consuming for such waveguides, several levels of approximation are often used and discussed below.

1.7 Mode solutions for 2D waveguides

In order to investigate the mode solutions for 2D waveguides, we need to solve equation [3]

$$
\nabla \times \nabla \times \overrightarrow{E}\left(x,y,z\right) = \frac{\omega^2}{c^2}n^2(x)\overrightarrow{E}\left(x,y\right)\left\{\overrightarrow{H} = \frac{\nabla \times \overrightarrow{E}}{i\omega\mu_0}\right\}
\tag{1.59}
$$

which meet all the proper boundary conditions for the electric and magnetic field at all the interfaces. The operator ∇ is

$$
\nabla = \hat{x}\frac{\partial}{\partial x} + \hat{y}\frac{\partial}{\partial y} + \hat{z}\frac{\partial}{\partial z}
\tag{1.60}
$$

Define,

$$
\nabla_t = \hat{x}\frac{\partial}{\partial x} + \hat{y}\frac{\partial}{\partial y} \Rightarrow \nabla = \nabla_t + \hat{z}\frac{\partial}{\partial z}
\tag{1.61}
$$

From $\nabla \times \overrightarrow{E} = i\omega\mu_0\overrightarrow{E}$, it follows that

$$
\begin{aligned}
&\left(\nabla \times \overrightarrow{E}\right)\cdot\hat{z} = i\omega\mu_0\overrightarrow{H}\cdot\hat{z} = i\omega\mu_0 H_z e^{i\beta z}\\
&\Rightarrow \left(\nabla_t \times \overrightarrow{E}_t\right)\cdot\hat{z} = i\omega\mu_0 H_z\\
&\Rightarrow H_z = \frac{\left(\nabla_t \times \overrightarrow{E}_t\right)\hat{z}}{i\omega\mu_0}
\end{aligned}
\tag{1.62}
$$

Similarly,

$$
E_z = \frac{\left(\nabla_t \times \overrightarrow{H}_t\right)\cdot\hat{z}}{-i\omega\varepsilon_0 n^2}
\tag{1.63}
$$

14

Equations 1.62 and 1.63 demonstrate that understanding the field's transverse components is sufficient since the z-components can be calculated from them. We need to solve

$$\nabla \times \nabla \times \overrightarrow{E} = \frac{\omega^2}{c^2} n^2(x,y) \overrightarrow{E}$$
$$\Rightarrow \nabla(\nabla \cdot \overrightarrow{E}) - \nabla^2 \overrightarrow{E} = \frac{\omega^2}{c^2} n^2(x,y) \overrightarrow{E} \tag{1.64}$$

Taking the transverse component gives,

$$\nabla_t(\nabla \cdot \overrightarrow{E}) - \nabla^2 \overrightarrow{E}_t e^{i\beta z} - \frac{\omega^2}{c^2} n^2 \overrightarrow{E}_t e^{i\beta z} \tag{1.65}$$

For the first two terms on the right hand side, we need to find convenient and useful expressions. Now

$$\nabla \cdot \overrightarrow{E} = \nabla_t \overrightarrow{E}_t e^{i\beta z} + i\beta \overrightarrow{E}_z e^{i\beta z} \tag{1.66}$$

but

$$\nabla \cdot \overrightarrow{E} = 0$$
$$\Rightarrow \nabla_t \left(n^2 \overrightarrow{E}_t \right) + i\beta n^2 \overrightarrow{E}_z = 0$$
$$\Rightarrow i\beta \overrightarrow{E}_z = -\frac{\nabla_t \cdot \left(n^2 \overrightarrow{E}_t \right)}{n^2}$$
$$\Rightarrow \nabla \cdot \overrightarrow{E} = \nabla_t \cdot \overrightarrow{E}_t e^{i\beta z} + i\beta E_z e^{i\beta z} = \nabla_t \cdot \overrightarrow{E}_t e^{i\beta z} - \frac{\nabla_t \cdot \left(n^2 \overrightarrow{E}_t \right)}{n^2} e^{i\beta z}$$
$$\Rightarrow \nabla_t \left(\nabla \cdot \overrightarrow{E} \right) = \nabla_t \left(\nabla_t \cdot \overrightarrow{E}_t \right) e^{i\beta z} - \nabla_t \left[\frac{\nabla_t \cdot \left(n^2 \overrightarrow{E}_t \right)}{n^2} \right] e^{i\beta z}$$

$$\tag{1.67}$$

The other term in Equation (1.65) is

$$\nabla^2 \overrightarrow{E}_t e^{i\beta z} = \nabla_t^2 \overrightarrow{E}_t e^{i\beta z} - \beta^2 \overrightarrow{E}_t e^{i\beta z} \tag{1.68}$$

Using the results above, Equation (1.65) becomes

$$-\nabla_t^2 \overrightarrow{E}_t + \nabla_t \left[\nabla_t \cdot \overrightarrow{E}_t - \frac{\nabla_t \cdot \left(n^2 \overrightarrow{E}_t \right)}{n^2} \right] - \frac{\omega^2}{c^2} n^2 \overrightarrow{E}_t = -\beta^2 \overrightarrow{E}_t \tag{1.69}$$

To obtain the exact solution, the above eigenvalue equation must be solved. The equation can be put in the form,

$$\begin{bmatrix} \overrightarrow{P}_{xx} & \overrightarrow{P}_{xy} \\ \overrightarrow{P}_{yx} & \overrightarrow{P}_{yy} \end{bmatrix} \begin{bmatrix} \overrightarrow{E}_x \\ \overrightarrow{E}_y \end{bmatrix} = -\beta^2 \begin{bmatrix} \overrightarrow{E}_x \\ \overrightarrow{E}_y \end{bmatrix} \tag{1.70}$$

15

where the different operators are.

$$\overrightarrow{P}_{xx}E_x = -\frac{\partial}{\partial x}\left[\frac{1}{n^2}\frac{\partial\left(n^2 E_x\right)}{\partial x}\right] - \frac{\partial^2 E_x}{\partial y^2} - \frac{\omega^2}{c^2}n^2 E_x \tag{1.71}$$

$$\overrightarrow{P}_{xy}E_x = -\frac{\partial}{\partial x}\left[\frac{1}{n^2}\frac{\partial\left(n^2 E_y\right)}{\partial y}\right] + \frac{\partial^2 E_y}{\partial x\partial y} \tag{1.72}$$

$$\overrightarrow{P}_{xy}E_x = -\frac{\partial^2 E_y}{\partial x^2} - \frac{\partial}{\partial y}\left[\frac{1}{n^2}\frac{\partial\left(n^2 E_y\right)}{\partial y}\right] - \frac{w^2}{c^2}n^2 E_y \tag{1.73}$$

$$\overrightarrow{P}_{yx}E_x = -\frac{\partial}{\partial y}\left[\frac{1}{n^2}\frac{\partial\left(n^2 E_x\right)}{\partial x}\right] + \frac{\partial^2 E_x}{\partial y\partial x} \tag{1.74}$$

The above equation is an egienvalue equation and the solution yields the transverse components of the electric field $\overrightarrow{E}$ for the mode and the corresponding propagation constant $\beta(\omega)$. $E_x(x,y)$ can be calculated from $E_x(x,y)$ and $E_y(x,y)$ as previously stated, and $\overrightarrow{H}$ field from the relation

$$\overrightarrow{H} = \frac{\left(\nabla\times\overrightarrow{E}\right)}{i\omega\mu_0} \tag{1.75}$$

For the piecewise uniform indices, all derivatives of the index can be dropped provided appropriate boundary conditions are conducted at all the interfaces.

1.7.1 The semi-vectorial approximation

If one transverse component (either E_x or E_y) dominates over other components in some cases of practical interest. We can assume that the other transverse field component is zero. For example, if we know E_x dominates, then we can assume that E_y is zero and solve the much simpler egienvalue equation,

$$\begin{aligned}
&\hat{P}_{xx}E_x = -\beta^2 E_x \\
&\Rightarrow -\frac{\partial}{\partial x}\left[\frac{1}{n^2}\frac{\partial n^2 E_x}{\partial x}\right] - \frac{\partial^2 E_x}{\partial y^2} - \frac{w^2}{c^2}n^2\left(x,y\right)E_x = -\beta^2 E_x
\end{aligned} \tag{1.76}$$

The above equation is refered to as semi-vectorial approximation. For piecewise uniform dielectrics, we can also write it as,

$$\begin{aligned}
&-\frac{\partial^2}{\partial x^2}E_x - \frac{\partial^2}{\partial y^2}E_x - \frac{w^2}{c^2}n^2\left(x,y\right)E_x = -\beta E_x \\
&\Rightarrow -\nabla_t^2 E_x - \frac{w^2}{c^2}n^2\left(x,y\right)E_x = -\beta^2 E_x
\end{aligned} \tag{1.77}$$

Assuming that we apply the necessary boundary conditions on $E_x(x,y)$ at all the dielectric interfaces for the x-component of the electric field. Following the

XX$_{VH}$	E	H
TE$_{00}$		
TM$_{00}$		
TM$_{01}$		
TE$_{01}$		
TE$_{10}$		
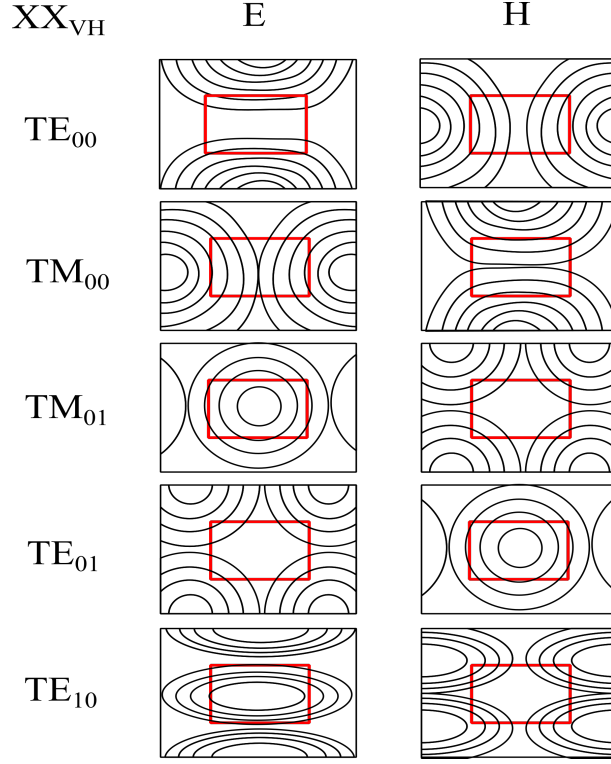
Figure 1.13: the electrical distribution for HE$_{pq}$ and TE$_{pq}$ modes

discovery of dominant $E_x(x, y)$ component, the remaining field components can be found as follows,

$$\nabla \cdot \left(n^2 \overrightarrow{E} \right) = 0$$

$$\Rightarrow E_z = \frac{i}{\beta} \frac{1}{n^2} \frac{\partial n^2 E_x}{\partial x} \tag{1.78}$$

$$\overrightarrow{H} = \frac{\left(\nabla \times \overrightarrow{E} \right)}{i \omega \mu_0}$$

$$\Rightarrow H_y = \frac{\beta}{\omega \mu_0} E_x - \frac{1}{\beta \omega \mu_0} \frac{\partial}{\partial x} \left[\frac{1}{n^2} \frac{\partial \left(n^2 E_x \right)}{\partial x} \right] \tag{1.79}$$

$$\Rightarrow H_x = \frac{1}{\beta \omega \mu_0} \frac{\partial}{\partial y} \left[\frac{1}{n^2} \frac{\partial \left(n^2 E_x \right)}{\partial x} \right]$$

$$\nabla \cdot \overrightarrow{H} = 0$$

$$\Rightarrow H_z = -\frac{1}{i \omega \mu_0} \frac{\partial E_x}{\partial y} \tag{1.80}$$

17

When the horizontal component of electric field dominates the modes are often called HE_{pq} modes or TE_{pq} modes. When the vertical component of electric field dominates the modes are called EH_{pq} modes or TM_{pq} modes. The two subscripts p and q denote the number of nodes that the dominant electric field component has in the horizontal and vertical directions, respectively. Figure 1.13 reports the some typical examples of the electrical distribution for HE_{pq} and TE_{pq} modes, where the p and q are selected as 0 or 1, respectively.

1.7.2 The scalar field approximation

If one transverse component dominates over other and the index differences between different regions of the structures are also relatively small, the semi-vectorial approximation can be used, and the normal electrical field component at all dielectric interfaces may likewise be eliminated from boundary conditions. For example, if we know a priori that $E_x(x, y)$ dominated then we can solve the equation,

$$-\frac{\partial^2}{\partial x^2} E_x(x, y) - \frac{\partial^2}{\partial y^2} E_x(x, y) - \frac{w^2}{c^2} n^2(x, y) E_x(x, y) = -\beta^2 E_x(x, y)$$

$$\Rightarrow -\nabla_t^2 E_x(x, y) - \frac{w^2}{c^2} n^2(x, y) E_x(x, y) = -\beta^2 E_x(x, y)$$

(1.81)

Provided that the field and its derivative are continuous through all dielectric interface. This is called the scalar field approximation. Once the domininat component has been found, the remaining field component can be easily found by using the case of the semi-vectorial approximation. Scalar field gives very accurate answers for the propagation vector $\beta(\omega)$ or the effective index $n_{eff}(\omega$ as long as one mode effective index is far away from the index at cut-off frequency. It is also very accurate in calculating mode confinement factors.

1.7.3 Slab waveguide approximation
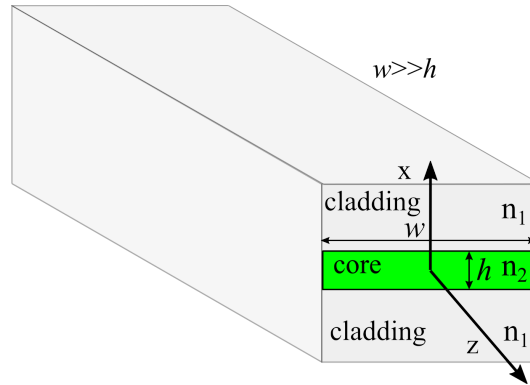
Figure 1.14: The concept of slab waveguide

If the width of waveguide is much larger than its thickness, the modes and effective indices can approximated calculated by a slab waveguide, as shows in Figure 1.14

The slab waveguide supports both TE and TM modes. For TE modes, the electric field can be written as,

$$\overrightarrow{E}(x,z) = \hat{y}E_0\phi(x)e^{i\beta z} \tag{1.82}$$

In the region with piecewise uniform index (i.e. core and cladding), ϕ satisfies,

$$\left[\frac{\partial^2}{\partial x^2} - \frac{\omega^2}{c^2}n^2(x)\right]\phi(x) = -\beta^2\phi(x) \tag{1.83}$$

For a given frequency ω, all solutions to the above equation can be found, which is an eigenvalue equation with eigenfunction $\phi(x)$ and eigenvalue $-\beta^2$. Once the electric field has been found, the magnetic field $\overrightarrow{H}$ can be found as follows,

$$\begin{aligned}\overrightarrow{H}(x,z) &= \frac{\nabla \times \overrightarrow{E}}{i\omega\mu_0} = \frac{\left(\hat{x}\frac{\partial}{\partial x} + i\beta\hat{z}\right) \times \overrightarrow{E}(x,y)}{i\omega\mu_0} \\ &= \left\{\frac{\hat{z}E_0}{i\omega\mu_0}\frac{\partial\phi(x)}{\partial x} - \hat{x}\frac{E_0\beta}{\omega\mu_0}\phi(x)\right\}e^{i\beta z}\end{aligned} \tag{1.84}$$

The boundary conditions for solving the above egienvalue equation are as follows:

1. y-component of the electric field is continuous at the core-cladding interfaces

2. z-component of the magnetic field is continuous at the core-cladding interfaces.

3. x-component of the magnetic field is continuous at the core-cladding interfaces

The integer index m (m=0, 1, 2, 3, ...) is used to mark solutions. As a result, the field for the TE_m mode is,

$$\overrightarrow{E}(x,y) = \hat{y}E_0\phi_m(x,\omega)e^{i\beta_m(\omega)z} \tag{1.85}$$

where the frequency ω dependence of the egienfunctions and the propagation vector β is clearly stated. For the TE modes we assume the solution,

$$\phi(x) = \begin{cases} C_1 e^{-\gamma(x-h/2)} & x \geq h/2 \\ \begin{cases} C_2 cos(kx) \\ C_2 sin(kx) \end{cases} & -h/2 \leq x \leq h/2 \\ C_1 e^{\gamma(x+h/2)} & x \leq -h/2 \end{cases} \tag{1.86}$$

Using the above solutions in the equation 1.83, we obtain

19

$$\left.\begin{array}{l} \beta^2 + k^2 = \dfrac{\omega^2}{c^2} n_2^2 \\[2mm] \beta^2 - \gamma^2 = \dfrac{\omega^2}{c^2} n_2^1 \end{array}\right\} \Rightarrow \sqrt{\dfrac{w^2}{c^2}(n_2^2 - n_1^2) - k^2} \tag{1.87}$$

Using the boundary conditions provides,

$$\tan\left(\frac{kd}{2}\right) = \frac{\gamma}{k} \text{ (cosine solutions - even TE modes)}$$
$$-\cot\left(\frac{kd}{2}\right) = \frac{\gamma}{k} \text{ (sine solutions - odd TE modes)} \tag{1.88}$$

Similarly, above analysis also can be used for the TM modes, provided,

$$\overrightarrow{E}(x, z) = \hat{y} H_0 \phi(x) e^{i\beta z} \tag{1.89}$$

$$\overrightarrow{E}(x, z) = \frac{\nabla \times \overrightarrow{H}}{-i\omega\varepsilon_0 n^2(x)} = \left\{ \frac{\hat{z} H_0}{i\omega\varepsilon_0 n^2(x)} \frac{\partial\phi(x)}{\partial x} + \hat{x} \frac{H_0\beta}{\omega\varepsilon_0 n^2(x)} \phi(x) \right\} e^{i\beta z} \tag{1.90}$$

$\phi(x)$ still satisfies 1.83, assume solution of the form,

$$\phi(x) = \begin{cases} C_1 e^{-\gamma(x - h/2)} & x \geq h/2 \\ \begin{cases} C_2 \cos(kx) \\ C_2 \sin(kx) \end{cases} & -h/2 \leq x \leq h/2 \\ C_1 e^{\gamma(x + h/2)} & x \leq -h/2 \end{cases} \quad \begin{cases} \beta^2 + k^2 = \frac{\omega^2}{c^2} n_2^2 \\ \beta^2 - \gamma^2 = \frac{\omega^2}{c^2} n_2^1 \end{cases} \tag{1.91}$$

by imposing the same boundary conditions as TE modes, we can get follows:

$$\tan\left(\frac{kd}{2}\right) = \frac{n_2^2 \gamma}{n_1^2} \text{ (cosine solutions - even TM modes)}$$
$$-\cot\left(\frac{kd}{2}\right) = \frac{n_2^2 \gamma}{n_1^2} \text{ (sine solutions - odd TM modes)} \tag{1.92}$$

In general, the behavior of the TM modes is similar to the TE modes.

1.8 Energy and power in 2D waveguides

The energy flow of electromagnetic field is provided by the complex Poynting vector,

$$\overrightarrow{S}(\overrightarrow{r}) = \frac{1}{2} Re\left[\overrightarrow{E}(\overrightarrow{r}) \times \overrightarrow{H} * (\overrightarrow{r})\right]$$
$$\overrightarrow{S}(\overrightarrow{r}) = \frac{1}{4}\left[\overrightarrow{E}(\overrightarrow{r}) \times \overrightarrow{H} * (\overrightarrow{r}) + \overrightarrow{E} * (\overrightarrow{r}) \times \overrightarrow{H}(\overrightarrow{r})\right] \tag{1.93}$$

The electric and magnetic fields for two dimensional waveguides are of the form

$$\overrightarrow{E}\left(x,y,z\right) = \left[\hat{x}E_x\left(x,y\right) + \hat{y}E_y\left(x,y\right) + \hat{z}E_z\left(x,y\right)\right]e^{i\beta z}$$
$$\overrightarrow{H}\left(x,y,z\right) = \left[\hat{x}H_x\left(x,y\right) + \hat{y}H_y\left(x,y\right) + \hat{z}H_z\left(x,y\right)\right]e^{i\beta z} \tag{1.94}$$

The total energy flow in a waveguide is obtained by integrating the Poyniting vector over the cross-section of the waveguide

$$P\left(z\right) = \iint \overrightarrow{S} \cdot \overrightarrow{z}\, dxdy = \frac{1}{4}\iint\left[\overrightarrow{E}\times\overrightarrow{H}^* + \overrightarrow{E}^*\times\overrightarrow{H}\right]\cdot\overrightarrow{z}\, dxdy$$
$$= \frac{1}{4}\iint\left[\overrightarrow{E}_t\times\overrightarrow{H}_t^* + \overrightarrow{E}_t^*\times\overrightarrow{H}_t\right]\cdot\overrightarrow{z}\, dxdy \tag{1.95}$$

Provided the materials to be dispersive, the energy per unit length of the waveguide is,

$$W\left(z\right) = \iint\left[\frac{1}{4}\frac{\partial\left(\omega\varepsilon_0\varepsilon\right)}{\partial\omega}\overrightarrow{E}\cdot\overrightarrow{E}^* + \frac{1}{4}\mu_0\overrightarrow{H}\cdot\overrightarrow{H}^*\right]dxdy =$$
$$\iint\left[\frac{1}{4}\varepsilon_0 n\left(2n_g^M - n\right)\overrightarrow{E}\cdot\overrightarrow{E}^* + \frac{1}{4}\mu_0\overrightarrow{H}\cdot\overrightarrow{H}^*\right]dxdy \tag{1.96}$$

Here, $n_g^M\left(\omega\right)$ is the index for material group, defined as,

$$n_g^M\left(\omega\right) = n\left(\omega\right) + \omega\frac{dn\left(\omega\right)}{d\omega} \tag{1.97}$$

The superscript "M" is used to avoid confusion with the optical mode's group index. The following relation can also be proven,

$$\frac{1}{4}\iint\varepsilon_0 n^2\overrightarrow{E}\cdot\overrightarrow{E}^* = \frac{1}{4}\iint\mu_0\overrightarrow{H}\cdot\overrightarrow{H}^* dxdy \tag{1.98}$$

Therefore, the energy per unit length can be written as,

$$W\left(z\right) = \frac{1}{2}\iint\varepsilon_0 nn_g^M\overrightarrow{E}\cdot\overrightarrow{E}^* dxdy \tag{1.99}$$

The effective index $n_{eff}(w)$ of a mode is,

$$\beta\left(\omega\right) = \frac{\omega}{c}n_{eff}\left(\omega\right) \tag{1.100}$$

21

The group velocity of a mode is,

$$\frac{1}{V_g(\omega)} = \frac{\partial \beta}{\partial \omega} \tag{1.101}$$

$$V_g(\omega) = \frac{c}{n_g(\omega)} \tag{1.102}$$

V_g is frequently expressed in terms of the group index of the mode,

$$\frac{n_g}{c} = \frac{W(z)}{P(z)} = \frac{\iint \varepsilon n n_g^M \overrightarrow{E} \overrightarrow{E}^* dx dy}{\iint Re\left[\overrightarrow{E}_t \times \overrightarrow{H}_t^*\right] \cdot \hat{z}} dx dy \tag{1.103}$$

1.9 Mode overlap ratio theory for hybrid waveguides

When a mode propagates from one waveguide to the second one, mode overlap (mode distribution match) ratio is introduced, which aims to measure the field overlap and power coupling between an input mode from one waveguide and all modes of a second waveguide. Mode overlap ratio Γ [4] that is theoretically derived from the orthonormal relation of egienmodes, Assuming $\{E_{tu}, H_{tu}\}$ and $\{E_{tv}, H_{tv}\}$ are normalized transverse optical fields of two egienmodes in a 2D dielectric waveguide (DW) propagating along $+ z$ direction with propagation constant β_u and β_v, respectively, they will satisfy the orthonormal relation:

$$\frac{1}{4}\iint \left[\overrightarrow{E}_{tu} \times \overrightarrow{H}_{tv}^* + \overrightarrow{E}_{tv}^* \times \overrightarrow{H}_{tu}\right] dx dy = \delta_{u,v} \tag{1.104}$$

where $[]_z$ indicates the component of a vector in z-direction, and $\delta_{u,v}$ is Kronecker delta function. In DW, all egienmodes form a full orthogonal function system. It means that optical field $\{E_{tm}, H_{tm}\}$ propagating in hybrid plasmonic waveguide (HPW) can be described as superposition of the egienmodes:

$$\overrightarrow{E}_{tm} = \sum_u a_u \overrightarrow{E}_{tu} \cdot \exp(-j\beta_u z), \overrightarrow{H}_{tm} = \sum_u a_u \overrightarrow{H}_{tu} \cdot \exp(-j\beta_u z) \tag{1.105}$$

The mode expansion coefficient (α_u) can be expressed as follows based on 1.104:

$$a_u \cdot \exp(-j\beta_u z) = b_u = \frac{1}{4}\iint \left[\overrightarrow{E}_{tm} \times \overrightarrow{H}_{tu}^* + \overrightarrow{E}_{tu}^* \times \overrightarrow{H}_{tm}\right]_z dx dy \tag{1.106}$$

$\gamma_u = |a_u|^2 = |b_u|^2$ represents the optical power flow in egienmode $\{E_{tu}, H_{tu}\}$. By normalizing γ_u with respect to the optical power flow of $\{E_{tm}, H_{tm}\}$, we can get the mode overlap ratio (Γ) between the optical field $\{E_{tm}, H_{tm}\}$ propagating in HPW and the egienmode field $\{E_{tu}, H_{tu}\}$ as

$$\Gamma = \frac{\left|\frac{1}{4}\iint\left[\overrightarrow{E}_{tm}\times\overrightarrow{H}_{tu}^*+\overrightarrow{E}_{tu}^*\times\overrightarrow{H}_{tm}\right]_z dx dy\right|^2}{\frac{1}{4}\iint\left[\overrightarrow{E}_{tm}\times\overrightarrow{H}_{tu}^*+\overrightarrow{E}_{tm}^*\times\overrightarrow{H}_{tm}\right]_z dx dy \cdot \frac{1}{4}\iint\left[\overrightarrow{E}_{tu}\times\overrightarrow{H}_{tu}^*+\overrightarrow{E}_{tu}^*\times\overrightarrow{H}_{tu}\right]_z dx dy} \tag{1.107}$$

1.10 Applications of polarization

Polarization of light has various applications in many subjects, such as chemistry, astronomy, optical communications, material science, and geology.

Polarized sunglasses are very popular for outdoor enthusiasts, fisherman, and boaters since their benefits reduce the glare of the sun. Sunglasses are usually coated with some chemical materials which can filter the glare by absorbing the incoming horizontal light, and creating openings for vertical light. Therefore, the images that we see with polarized sunglasses are darker than usual. When aerosols scatter sunlight pass through Earth's atmosphere, polarization can be seen in the skylight. In clear skies, the scattered light creates brilliance and color. This partial polarization of scattered light can be employed in images to darken the sky and increase contrast. This effect is most noticeable when two points on the sky meet at a 90° angle to the Sun. These phenomena are employed in the polarizing filters to improve the results of photography scenes that feature reflection or dispersion by the sky [5].

In navigation, sky polarization is employed for orientation. When neither sun nor stars were visible, the Pfund sky compass was employed in the proximity to the magnetic poles of the world (e.g. under daytime cloud or twilight). In addition, many animals can perceive some components of the polarized light (i.e. a linear horizontally polarized light). Since the linear polarization of skylight is always perpendicular to the incident direction of the sunlight, which is normally used for navigational purposes. For example, some insects use this information to guide their communicative dances [6].

The liquid-crystal display (LCD) technology principle depends on the linear polarization axis rotating through the liquid crystal array. Light first passes through a straight-lined polarized sheet from the backlight. This polarized light goes through the actual liquid crystal layer, which can be arranged in either pixels (for television or computer monitor) or in a format like a seven-segment display, or one with customized product symbols. A consistent right (or left) chirality, consisting essentially of small helixes, is produced in the liquid crystal layer, which causes circular birefringence and is designed to rotate the linear polarity at a 90-degree level. However, the molecules stretch out, reduce or lose the circular birefringence when the voltage is applied across a cell. While another linear polarizing sheet on the viewing side of the display, usually 90 degrees from the one behind the active layer. Thus the polarization of the transmitted light remains at the right angle to the front of the polarizer when the application of sufficient voltage removes the circular birefringence. However, without voltage, the 90-degree rotation of polarization precisely matches the front polarizer axis so that the light passes. Mid voltages cause the polarization axis to be immediately rotated, and the pixel has intermediate intensity. Displays based on this principle have become widely available and have become largely obsolete in most of TVs, computer monitors, and Video projectors. When polarization is applied for LCD screens, someone with polarized sunglass is immediately noticeable, and the display is often illustratable.

In a different sense, polarization creates and presents 3D movies. Three-

dimensional movies are formed by showing two movies simultaneously through two projectors. The two movies are filmed from two cameras located in different places. Each film is then projected onto a metal screen from different sides of the audience. The polarization axis of the polarizing filter used for the projector on the left may be oriented horizontally, while the polarizing filter used for the projector on the right may be aligned vertically. As a result, two slightly different movies are being projected on a screen. Each move is cast by polarized light with a perpendicular orientation to the other movie. After that, the audience is given glasses with two Polaroid filters. The polarization axis of each filter is different: one is horizontal and the other is vertical. As a result of this configuration of projectors and filters, the left eye sees the movie projected from the right projector, while the right eye sees the movie projected from the left projector. Thus, the viewer receives a perception of depth.

In geology, birefringence is a property that is widespread in crystals. Therefore, such property helps identify it. For example, this property is widely utilized in mineralogy, where polarization microscopes are used to identify minerals [7]. Polarization also occurs in sound waves in solid materials. Especially in seismology, three different polarizations propagate through the ground, including horizontally and vertically polarized seismic waves (shear waves), and longitudinal polarization (compressional waves). Investigating these polarization waves may help human beings to predict earthquakes and underground activities [8].

In astronomy, the investigation of polarized electromagnetic radiation provides much valuable information. Polarization occurs in radiation from coherent astronomical sources (i.e. hydroxyl or methanol), and incoherent sources such as large radio lobes in active galaxies and pulsar radio radiation, and is also imposed on starlight by scattering from interstellar dust. Polarization not only provides information on radiation sources and scattering, but also investigates the interstellar magnetic field via Faraday rotation [9]. The polarization of cosmic microwave background is being utilized to explore the early universe's mechanics [10, 11].

In material science, ellipsometry is a powerful tool for measuring the uniform surface's optical characteristics. It entails measuring the state of polarization of light after specular reflection from such a surface, which is usually performed as a function of incidence angle or wavelength. Because ellipsometry relies on reflection, the sample doesn't need to be transparent to light or have a visible reverse side. Ellipsometry can be used to calculate the complex refractive index of a bulk material's surface. It can also be used to figure out the parameters of one or more thin-film layers deposited on a substrate. Due to their reflection features, both the magnitude of the p and s polarization components, as well as their relative phase shifts can be predicted by ellipsometry. Except for the application in science and research, ellipsometers are often used in situ to manage production processes [12].

In engineering, stress-induced birefringence is a phenomenon that allows for the observation of strains in transparent materials. When viewed by two polarizers, the chromaticity of birefringence generally forms colored patterns. Internal stress created in the material is noticed as external forces are applied.

24

Furthermore, birefringence is frequently found due to tensions "locked-in" during the manufacturing process. This is well-known in cellophane tape, whose birefringence is caused by material stretching during the production process.

In radio antennas polarization is employed for receiving or transmitting the information. Radio antennas transmit or receive signals from a specific polarization, being entirely insensitive to converse polarization. In some cases, the polarization is a function of direction. Although the antennas have the possibility of linear, elliptical, and circular polarization, most are linearly polarized. Indeed, considerations of symmetry can show the polarization of the antenna entirely on a plane which includes the observer only in the direction of that plane. Such a feature applies in many cases that can easily deduce the polarization of an antenna from the intended propagation direction. Polarization is important in radio communication as the signal strength is reduced significantly if a horizontally polarized antenna is attempted, for instance, to receive a vertically polarized transmission. In satellite TV, this principle is used to double the capacity of the channel over a fixed frequency band. The same frequency channel can transmit two signals in opposite polarizations.

Because of presence of the soil, there are differences between horizontal and vertical polarization. The AM and FM radios usually use vertical polarization, while horizontal polarization is used for television. Horizontal polarization is avoided at low frequencies in particular. This is because the phase of a horizontally polarized wave is reversed after reflections by the ground. Therefore, the direct and reflected wave, which tends to cancel each other, is received by a remote station in the horizontal direction. Vertical polarization avoids this problem. Polarization is also crucial in transmitting radar pulses and radar reflection reception with one or another antenna. For example, circular polarization can prevent rainfall's backscattering of radar pulses. The same principle applies to dispersal by objects much less than wavy lengths like rainfall, just like a circularly polarized light reverses the handling of polarization. Reflecting that wave by an irregular metal object (such as an aircraft) will typically change the polarization and (part) receipt by the same antenna of the return wave.

In combination with the earth's magnetic field, the effect of free electrons in the ionosphere causes Faraday rotation, which is a kind of circular bireferentiality. This mechanism can rotate the linear polarization axis in interstellated space through electrons. The magnitude of the rotation of Faraday caused by such plasma in lower frequencies is greatly overwhelmed and therefore the effect of satellites on higher microwave frequencies is minimal. The transmission of medium or short waves is strongly affected after ionosphere refraction. As the path of a wave through the ionosphere, the earth's magnetic field vector along this path is rather unpredictable, an arbitrary orientation of the receiver is usually polarized on the wave transmitted through vertical (or horizontal) polarization.

It is well known that electromagnetic radiation carries a certain linear momentum in the direction of propagation. In addition, light carries a certain angular momentum if it is circularly polarized (or partially so). Compared with lower frequencies such as microwaves, the amount of angular momentum in light

is tiny and difficult to measure. However, it was utilized in an experiment to achieve speeds of up to 600 million revolutions per minute [13]

2 Wire grid reflecting polarizer for solar polarimetric observation

2.1 Background

2.1.1 Solar observations

Solar observation is the study of the Sun and its activity and relation to the Earth and the remainder of the Solar System, which provides much valuable information such as sun's temperature, chemical composition, dynamics, and plasma, creating opportunities for both science and technology. Solar observation is mainly focused on the extreme ultraviolet (EUV) and far ultraviolet (FUV) spectral range, ranging from 10 to 200 nm, as shown in Figure 2.1. FUV spectral region is one of the most useful regions for characterizing the energy, composition, and dynamics of the upper atmosphere of a planet. In solar physic missions, FUV remote sensing provides valuable insights into the upper atmosphere's structure, dynamics, input, and response, as well as its connections to the Sun, heliosphere, and magnetosphere via solar photons, magnetospheric magnetic and electric fields, and energetic particles. [14].
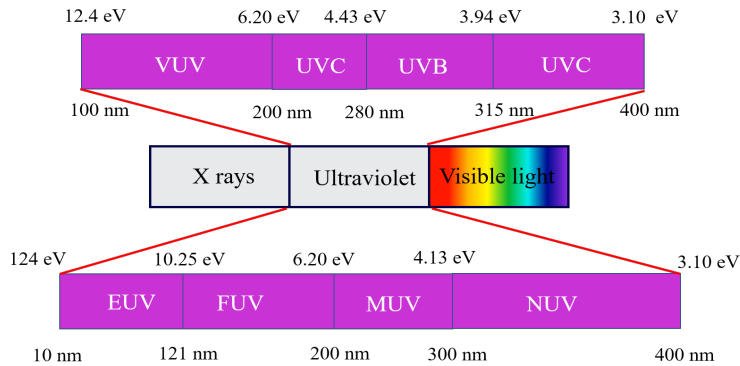

Figure 2.1: Subdivide ranges of UV spectrum according to ISO standard [15]

2.1.2 FUV polarimetric observation

Violent explosive activities such as solar flares, dark stripe bursts, and coronal mass ejections on the sun will have disastrous effects on high-tech fields such as aerospace, navigation, and communication. The energy bursts are mainly affected by the coronal magnetic field. FUV (90-200 nm) line polarization is an effective tool for the measurement of magnetic field vector of solar corona [16]. So far, many space missions have been launched for measuring Solar UV polarimetry, as is shown in Table 2.1. In 1976, Soviet Intercosmos satellite carried a UV spectro-polarimeter to record resonance-line polarization in the FUV wavelength region 121-150 nm of the chromospheric spectrum [17], which

demonstrated the feasibility of FUV polarization measurement in astronomical space. After that, 1980 Solar Maximum Mission performed the first polarimetric measurements in the solar spectrum below 200 nm [18]. SUMER/SOHU has explored the coronal magnetic fields via the Hanle effect on FUV resonance-line polarization of OVI, 103.2 nm [19]. The FUSP sounding-rocket payload was built to measure the Hanle effect in FUV resonance lines from hot star envelopes [20]. The Solar Ultraviolet Magnetograph Investigation sounding-rocket payload measures polarization in the UV lines generated in the transition area and higher chromosphere by Mg II 280 nm and C IV 154.8 nm [21]. These past missions have stimulated interest in solar and stellar FUV polarimetry, new missions, such as COMPASS [22], SolmeX [23], CLASP [24, 25] are also developing or proposed.

Table 2.1: Historical solar missions for FUV polarimetry

Missions	Launch time	FUV spectral region	Main optical elements
Soviet Intercosmos	1976	121-150 nm	Au and Al+MgF$_2$ coating
Solar Maximum Mission	1979	115-200 nm	MgF$_2$ waveplate
SUMER/SOHU	1996	100-160 nm	CVD-SiC coating
FUSP sounding-rocket	2003	105-145 nm	CaF$_2$ waveplate
SUMI sounding-rocket	2012	155 nm	MgF$_2$ waveplate
Solmex	2010	115-155 nm	MgF2 plate and Al+MgF$_2$ mirror
CLASP I	2015	121.6 nm	Al+MgF$_2$ mirrors

2.2   Motivation

Polarimetry in the far-ultraviolet (FUV) and extreme-ultraviolet (EUV) wavelength range is a technique that has recently grown in importance in many fields of modern science, including FUV/EUV ellipsometry [26], characterization and control of the beam polarization in synchrotrons [27–29] and free-electron laser sources [27, 30–33], and solar physics [34, 35]. A very interesting application in which the FUV polarimetry finds large employment is the measurement of solar magnetic field vector in the solar corona made via the Hanle effect [36] by using observation from space. Light associated to the FUV emission lines originating in the cromosphere and lower transition region, where the plasma has a temperature of $\log T \sim 4.6 - 5$, undergoes resonant scattering when propagating along the corona. Since the low density of the corona causes negligible depolarizing collisions between atoms, the resonant scattering induces a linear polarization with a degree that increases with the height from the solar surface, achieving relatively large values (up to 25%) [36, 37]. At the distances of $1.2 - 2$ solar radii from the Sun center, the magnetic field shows a magnitude in the $1 - 60$ G range, values high enough to produce a simultaneous alter-

ation (a reduction or an enhancement, depending on the scattering geometry) of the linear polarization degree and direction with respect to the case without the magnetic field. The bright lines in which the Hanle effect is particularly evident are the H_I Ly-α at 121.6 nm, the H_I Ly-β at 102.5 nm, the H_I Ly-γ at 97.2 nm and the O_{VI} doublet at 103.2 nm and 103.8 nm [38]. Considering these target lines, many examples of space missions with FUV polarimeters and spectro-polarimeters have been proposed, such as CLASP 1 [24,25], SolmeX [23] and COMPASS [22]. Nevertheless, the realization of such kind of instruments is still challenging, basically due to the technical difficulties encountered in the development of the main optical components.

Optical polarizers are among the most critical components in FUV polarimetric instrumentation mainly due to the small number of low-absorbent materials available in this spectral range. MgF_2 is perhaps the most used and studied material for its fair transparency at $\lambda > 115$ nm (i.e. the MgF_2 cutting-edge). Below this limit, LiF is the only other material with low absorption for $\lambda > 102.5$ nm, but its hygroscopicity highly degrades the transmittance just after a moderate humidity exposure [39]. Thus, in principle, among the lines previously listed only the H_I Ly-α can be manipulated with a polarizer working in transmission. For example, the birefringence of the MgF_2 bulk crystal makes the realization of transmissive polarizing beam-splitter feasible, like the Rochon or Wollaston prisms. In particular, MgF_2 Wollaston prisms were proposed for astronomical polarimetry in the FUV [40] even if the relatively small deviation angles achievable ($\simeq 20°$) require the adoption of an instrumental geometry characterized by large optical paths and, consequently, small throughput. Wiregrid polarizers (WGPs), which consist of periodic arrays of nano-metallic wires placed on a transmissive substrate, are an effective alternative to polarizing prisms. The anisotropic behavior given by the nano-metallic wires performs a high absorption of the radiation along a precise direction without affecting the transmittance of the orthogonal one. Although the WGPs are largely employed in the near ultraviolet ($\lambda > 193$ nm), visible and infrared [41], the extension to the FUV range, and in particular to the H_I Ly-α line, is currently a challenge of the nanotechnology [42].

As an alternative, polarizers based on optical coatings can be used when polarization is required at one specific wavelength, although they are usually characterized by a low transmittance. For instance, a fair transmissive linear polarizer tuned around 121.6 nm was obtained by realizing a stack of 3-4 bilayers of Al/MgF_2 [43]. Moreover, by exploiting the high reflectance of aluminum in this spectral range, a polarizing beam-splitter able to simultaneously select one polarization component by reflection and the perpendicular component by transmission has been fabricated [44]. The idea of adopting polarizing films working in reflection may give additional benefits. Firstly, at wavelengths longer than the MgF_2 cutting-edge the Al-protected mirrors show a reflectance up to 90% [45], which offers a good basis for the development of high efficiency polarizers [43,46–48]. Moreover, materials having good reflection properties also below the MgF_2 cutting-edge are available, enabling the possibility of developing polarizers for wavelengths shorter than 115 nm [49, 50].

Polarizing mirrors, which can reflect the desired polarization component with high efficiency, need to work with large incidence angles, sometimes greater than 70° [43], entailing instruments having polarization analyzer with grazing geometries and small throughput. In most cases, the configuration is based on the combination of various reflectance components. For example, the adoption of polarization-sensitive studies such as spin-polarized photoelectron spectroscopy and spectroscopic ellipsometry in synchrotron facilities has driven the research of new technological solutions [51, 52]. An example of a configuration based on a gold triple-reflection was reported in [53], which can achieve a polarization between 90% and 96% at the energy range from 2 eV to 40 eV. In addition, a triple- reflected gold polarizer for testing VUV ELIps capabilities in the VUV spectral region from 30 eV to 45 eV has been developed [54]. Nevertheless, compact reflective polarizers which can achieve extremely high polarization in the spectral energy below 10 eV are still difficult to realize.

2.3   Design and modeling

A different approach, which is still uninvestigated so far in the FUV range, consists of using reflective-WGPs [55]. By placing either reflective nano-wires on an absorptive substrate or absorptive nano-wires on a reflective substrate it is possible to achieve the anisotropic behavior in which a polarization component is efficiently reflected/absorbed whereas the orthogonal one is efficiently absorbed/reflected. Furthermore, since this method is not strictly connected to the interference process used in the thin polarizing films, the reflective-WGPs can act as a polarizer at different wavelengths. Such solution can provide very flexible and compact polarizers, which can be optimized for different incidence angles and that can work on a wide spectral range.

2.3.1   Structure and materials

Two different reflective-WGP concepts for the realization of a polarizer optimized at $\lambda = 121.6$ nm have been studied (Figure 2.2). As shown, the electric field of the impinging beam is split into two components, the transverse electric (TE), which is oriented along the wires, and the transverse magnetic (TM), which is perpendicular to the wires.

The first reflective-WGP concept is based on a high-reflective mirror optimized for a target wavelength (i.e. $\lambda = 121.6$ nm) on top of which absorptive nano-wires are exploited for removing the TM-component. The high reflectance is achieved by using an optically-thick Al layer (i.e. about 150 nm) over-coated by an optimized MgF_2 layer for preventing oxidation [45]. The optimization of the MgF_2 thickness was carried out using IMD software for an incidence angle of 45°, which is a typical incidence angle useful for folding mirrors in optical systems. The results are reported in Figure 2.3, where the reflectance at the working angle has been plotted versus the MgF_2 thickness (solid black curve). A thickness of 65 nm has been chosen because it produces a constructive interference and at the same time, ensures a good level of protection.
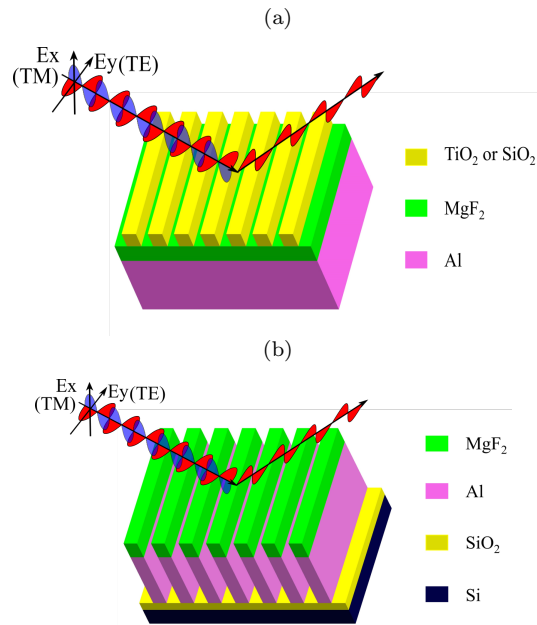
(a)

(b)

Figure 2.2: The two concept of reflective-WGP investigated: (a) model based on absorptive nano-wires, (b) model based on reflective nano-wires.
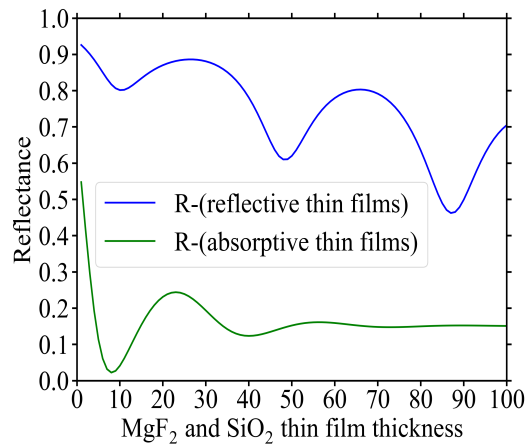

Figure 2.3: The reflectance of a MgF_2 layer on a Al substrate (blue curve) and of a SiO_2 layer on a Si substrate (red curve)

The nano-wires placed on top of the reflective bi-layers structure need to be fabricated using a material with low reflection and relative high absorption around the target wavelength. Such conditions suggests a family of materials whose refractive index has a real part n between 1 and 2 and a imaginary part k

between 0.5 and 1. Metals show a quite good reflectance in the FUV since they usually have a real part n close to zero and the imaginary part k greater than 1. On the other hand, fluorides are characterized by a high transparency due to the low value of the imaginary part of refractive index. Oxides, instead, are the materials which better meet the requirements for refractive index; among these, TiO_2 and SiO_2 have been selected as nano-wires' material candidates. The optical constants of the materials considered in this work are reported in Table 2.2 with the related references.

Table 2.2: Optical constants at $\lambda = 121.6$ nm of the materials considered in this work

Material	n	k	Reference
Al	0.0423	1.1404	[56]
MgF_2	1.7047	0.0180	[57]
SiO_2	1.9644	0.5793	[58]
TiO_2	1.1222	0.9157	[59]
Si	0.295	1.32	[60]

The second concept is based on high reflective nano-wires placed on a non-reflective substrate (Figure 2.2b), which acts as polarization selection by efficiently reflecting only the TE-component of the impinging electric field. In this case, efficient reflective nano-wires can be obtained starting from the same Al/MgF_2 mirror, which is etched in order to obtain the wires grating structure. Simulations used Si wafer as substrate which, however, typically shows a marked reflectance at $\lambda = 121.6$ nm (i.e. $>50\%$). In order to further reduce this value, a SiO_2 anti-reflection layer is added between the substrate and the reflective nano-wires. In Figure 2.3, the solid red line is the reflectance at $\lambda = 121.6$ nm of a SiO_2 layer deposited on a Si wafer as function of layer thickness, the working angle considered is still 45°. The thickness of 8 nm was selected because it allows to reduce the reflectance at a value $\simeq 3\%$.

2.3.2 Simulation description

The simulations of these structures at $\lambda = 121.6$ nm have been carried out in Wave Optics Module of COMSOL Multiphysics software by using the 2D boundary mode analysis. The solutions are based on finite element method (FEM) and the electric field is computed in all materials by solving via the following equation

$$\nabla \times (\mu_r^{-1} \nabla \times \overrightarrow{E}) - k_0 \left(\epsilon_r - \frac{j\sigma}{\omega\epsilon_0} \right) \overrightarrow{E} = 0 \qquad (2.1)$$

where $k_0 = \omega\sqrt{\mu_0\epsilon_0}$ is the wavenumber, μ_r and ϵ_r are the relative magnetic and dielectric permittivities of the medium, ϵ_0 is the vacuum electric permittivity and σ is the media conductivity. The 2D structure simulated is depicted in Figure 2.4a. The impinging beam excites the structure from the upper port (i.e. port 1, on-top of the vacuum media) inducing a back-reflected wave that

is evaluated by the port itself. The bottom port (i.e. port 2) acts as output port, implementing the bulk boundary condition for the substrate material. To reproduce the periodicity condition in the horizontal dimension, Floquet ports are used for the boundary conditions of the left and right sides. In our specific case the incident beam is linearly polarized and impinges on the structure at the nominal angle of 45°.

In the case of structures based on highly absorbing wires, three different shapes for such nano-wires were considered (see Figure 2.4b): the square, the isosceles triangle and a cosine. All these shapes can be easily described by using only three parameters: the pitch, w, the wires' width, w_1 and the wires' height, h. On the other hand, for the structure based on high-reflective nono-wires, only the square shape was investigated; in this case, the wires are unequivocally defined by the parameters w and w_1, because the wires' height is pre-determined by the high reflectance condition.
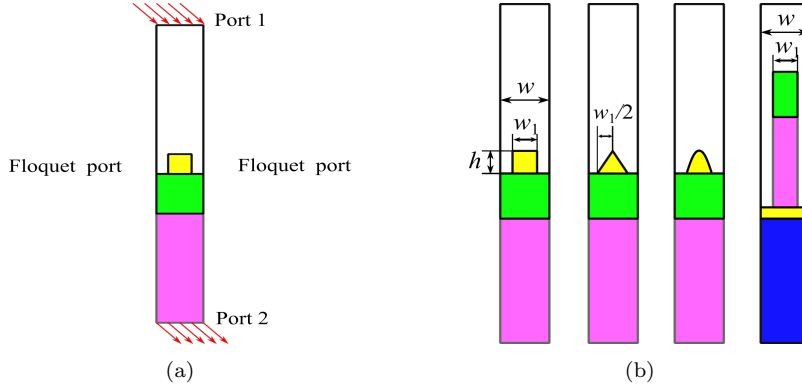

Figure 2.4: The 2-D boundary model used in the simulation. (a) The ports used for the boundary conditions. (b) The wires' shapes investigated in this work.

2.3.3 Scientific objectives

The performance of all structures were evaluated by considering the value of reflectance for the TE-component and the polarization degree defined as

$$P = \frac{R_{\mathrm{TE}} - R_{\mathrm{TM}}}{R_{\mathrm{TE}} + R_{\mathrm{TM}}} \tag{2.2}$$

where R_{TE} and R_{TM} are the reflectance for the TE and TM component, respectively. The maxima of the polarization degree function P for each structure was found by sweeping the parameters w, w_1 and, when necessary, h into the value ranges reported in Table 2.3. In this way, all local maxima were considered in the optimization process allowing for each the evaluation of the absolute TE-reflectance. Only the solutions having a nominal polarization degree P more than 99.5% and a R_{TE} more than 0.2 were taken into further consideration.

33

Table 2.3: Sweeping ranges used for the optimization of the WGP structures

WGP topology	Sweeping range
Absorptive wires	h: [1, 200] nm, w_1: [20, 200] nm, w: [w_1, 200] nm
Reflective wires	w_1: [20, 200] nm, w: [w_1, 200] nm

2.3.4 Optimization method

The optimization involved in this work is based on the design of experiments (DOE) method. DOE is very useful to study several impact factors and their interactions complexity in order to study the effect of all of them on one or more responses [61].

The desirability method is a method used for deciding the best condition for process improvement, allowing several responses to be optimized at the same time. As a result, the best responses conditions are obtained by minimizing, maximizing or seeking nominal values of requirements simultaneously, depending on the most convenient situation [62].

Where the value D evaluates is generally the levels of the combined set of responses. It is an index that also belonging to the interval [0, 1] and will be maximized when all responses approach as closely as its requirements. The closer of one D is to its respective specification limit, the closer the original responses are to their respective specification limits.

When a response maximization is needed, the transformation formula is shown in follow [63]:

$$d_i = \begin{cases} 0 & \hat{Y}_i < LSL \\ \left[\frac{\hat{Y}_i - L_i}{T_i - L_i}\right]^R & L_i \leq \hat{Y}_i \leq T_i \\ 1 & \hat{Y}_i \geq T_i \end{cases} \tag{2.3}$$

Where the L_i and T_i are the values of main and secondary target for the ith response, respectively. The R value suggests a preponderance of the superior limit (LSL). Values greater than unity should be applied when the response (Y_i) increases rapidly above L_i. Therefore, d_i grow slowly while the response value is maximized. Consequently, the ith response must be much greater than L_i to maximize D. When it is important to find values for the response below the fixed limits, $R<1$ can be used.

For the cases that the objective is to approach a target value, the transformation formulation can expressed as follows

$$d_i = \begin{cases} 0 & \hat{Y}_i < L_i \ or \ \hat{Y}_i > H_i \\ \left[\frac{H_i - \hat{Y}_i}{H_i - T_i}\right]^R & T_i \leq \hat{Y}_i \leq H_i \\ \left[\frac{\hat{Y}_i - L_i}{T_i - L_i}\right]^R & L_i \leq \hat{Y}_i \leq T_i \end{cases} \tag{2.4}$$

where the target response has two limitations: one maximum and one minimum value. The H_i is acceptable target for ith response.

2.4 Results and discussion

All the structures obtained from the optimization process are summarized in Table 2.4. Some of these show poor performance in terms of R_{TE} or P, making them unacceptable for the purpose of the present study. For example, the structures with cosine-shaped absorptive wires (i.e. design E and F in Table 2.4) as well as the SiO_2 triangle-shaped absorptive wires (i.e. design D) are not able to achieve the minimum requirements of TE-reflectance, although some of them give a very high polarization degree. The structure with SiO_2 rectangle-shaped absorptive wires (i.e. design B) is also discarded: despite this solution achieves the requirements in both the reflectance and polarization degree , it shows a ratio $\frac{w_1}{w} \simeq 0.96$ making this structure very challenging for the available manufacturing technologies. Designs A, C and G are the most promising

Table 2.4: Optimized parameters

| Absorptive WGPs					
Label	Wires' shape	Wires' material	Wires' parameters	R_{TE}	P
Design A	rectangle	TiO_2	$h = 38$ nm, $w_1 = 38$ nm, $w = 68$ nm	0.21407	99.970%
Design B	rectangle	SiO_2	$h = 115$ nm, $w_1 = 110$ nm, $w = 114$ nm	0.23700	99.857%
Design C	triangle	TiO_2	$h = 48$ nm, $w_1 = 69$ nm, $w = 71$ nm	0.25234	99.998%
Design D	triangle	SiO_2	$h = 64$ nm, $w_1 = 137$ nm, $w = 146$ nm	0.09093	99.993%
Design E	sine	TiO_2	$h = 96$ nm, $w_1 = 68$ nm, $w = 121$ nm	0.12225	99.999%
Design F	sine	SiO_2	$h = 89$ nm, $w_1 = 94$ nm, $w = 141$ nm	0.07771	99.580%
Reflective WGPs					
Design G	rectangle	Al/MgF_2	$w_1 = 39$ nm, $w = 80$ nm	0.30149	99.991%

structures in term of performance. In particular, all these structures have good performance in term of polarization factor P, although the designs based on absorptive nano-wires (i.e. A, and C) give a lower TE-reflectance than those based on reflective nano-wires (design G). In principle, in the structures based on absorptive nano-wires, the TE-component is efficiently reflected by the substrate and, with a lesser extent, from the wires themselves. In contrast, since the TM-component is perpendicular to the absorptive wires, the radiation propagates through the grid but the high absorption of the nano-wires strongly reduces the final reflectance. For a fixed material and wire shape, the attenuation of the TM-component (i.e. and then of the polarization factor P) is highly dependent on the grid pitch and wires' height. However, as all the designs presented in

this work are characterized by a w/λ ratio between 0.55–1.2, the gaps between the absorbent nano-wires have a size-scale such as to induce a lossy propagation towards the reflective substrate also for the TE wave. Consequently, the substrate contribution to the TE-reflectance dramatically degrades with the nano-wires volume fraction ($\propto w_1/w$) and their height. Thus, the overall efficiency of such structures is decreased by the non-negligible effects of losses affecting the TE-component of the radiation. In WGPs based on reflective wires, the TE-reflectance is only given by the nano-wires. The transparency of the MgF_2 at these wavelengths guarantees that the TE-radiation is well-reflected at the interface between MgF_2 and Al, with an additional small improvement given by the constructive interference of the MgF_2 layer. On the other hand, the TM-wave is transmitted through the metal wires grid because magnetic fields do not cause vibrations in the conducting electrons of the metallic grid. Although the TM-component undergoes some losses during the transmission, the TM-component is efficiently attenuated from the anti-reflective properties of the substrate. Therefore, the overall efficiency expected from reflective-wires structures is greater than that given by structures based on absorptive-wires.

2.4.1 Manufacturing feasibility and sensitivity analysis

The determination of the best solution also requires the evaluation of the sensitivity performance with respect to the values of the parameters w, w_1 and h obtained during the optimization process. Currently, WGPs with a pitch $\geq$ 100 nm can be easily manufactured with very high precision by using nano-imprinting lithography [64–67]. However, the fabrication of repeatable and precise WGPs with a pitch $\leq$ 100 nm is still a challenge, [68–72] mainly due to the high technical complexity and cost associated to the use of the techniques available in the industry so far, such as EUV lithography, laser writing, e-beam direct writing, or holographic interference in a production environment. Fortunately, many new methods have been proposed and are still under investigation in order to fabricate such periodical nanometric-pitched structures. For example, Liu et al. [73] fabricated a 38nm half-pitch grating over large areas by using combined immersion holography and low-temperature atomic spacer lithography. Pelletier et al. [74] fabricated a 16.5 nm half-pitch wire grid in a cheap way, through the use of a self-assembling diblock copolymer mask whereas Fan et al. [75] reported a patterning of line/spaces with an HP of 6 nm by using HSQ photoresist via EUV IL. All these results make the manufacturing of our WGPs feasible.
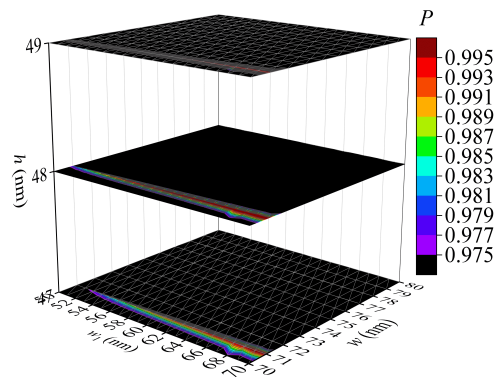
(a)

(b)
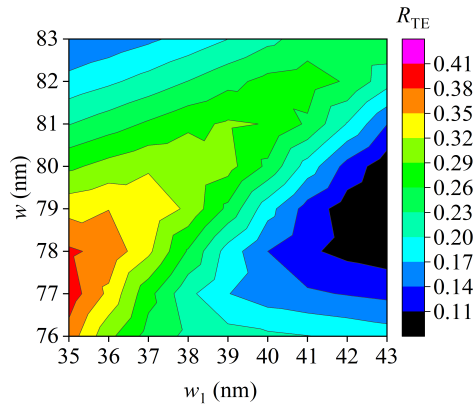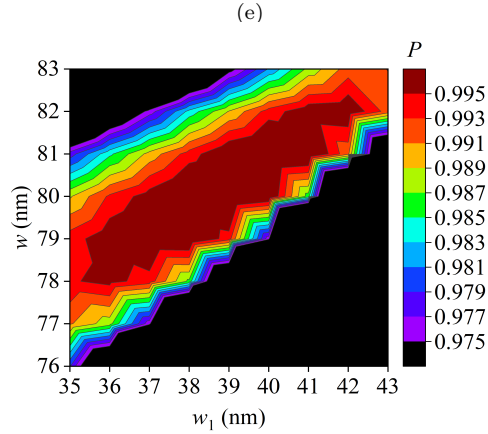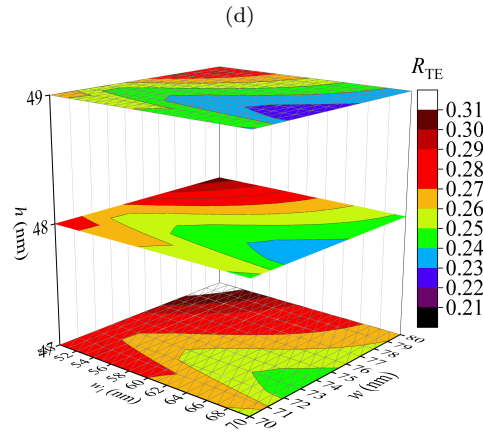

(c)

(d)

(e)

(f)
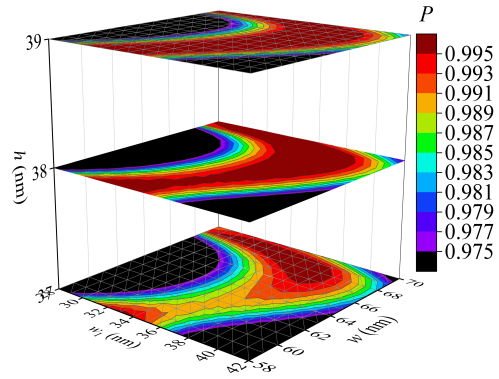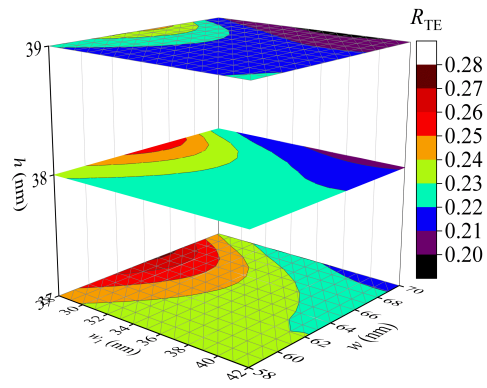
Figure 2.5: Sensitivity analysis for the Design A, C and G. (a) and (b): the polarization degree and the TE reflectance versus free parameters of Design A; (c) and (d): the polarization degree and the TE reflectance versus free parameters of Design C; (e) and (f): the polarization degree and the TE reflectance versus free parameters of Design G.

The sensitivity was investigated by sweeping w and w_1 parameters in the range $\pm 20\%$ from the nominal value with a step of 1 nm. Since the height of nano-wires is easily to be guaranteed in the model deposition processes, only a sweep of $\pm$ 1 nm from the nominal value was considered for the structures based on absorptive wires. The results obtained are reported in Figure 2.5. The evaluation of the robustness of a structure is based on the determination of the range within each parameter can vary to maintain a variation of the polarization degree P less than 2% with respect to the nominal value and the TE-reflectance higher than 20%. The acceptable ranges of the parameters w and w_1 computed for Design A, C and E are reported in Table 2.5.

Among the absorptive WGPs, Design A shows the highest acceptable range for both w and w_1 since the performance in term of polarization degree and TE-reflectance remain acceptable if the period w and the width w_1 fall in the range of 62-70 nm and 33-40 nm, respectively. In contrast, the polarization degree given by Design C is very sensitive to the structure periodicity, requiring a precision within 1 nm for the wires' period (see Table 2.5), which turns out to be very challenging for the current manufacturing technology. Finally, the reflective WGP of Design G shows an acceptable range of 79-82 nm for w and 37-40 nm for w_1: despite these limits are more stringent than Design A, this structure is still feasible and worthy of attention considering its high TE-reflectance.

Table 2.5: Acceptable range for w and w_1 which ensure a drop of the polarization degree P less than 2% with respect to the nominal value and the TE-reflectance higher than 20%.

Structure	w		w_1	
	nominal value	acceptable range	nominal value	acceptable range
Design A	68 nm	62 - 70 nm	38 nm	33 - 40 nm
Design C	71 nm	70 - 72 nm	69 nm	65 - 70 nm
Design G	80 nm	79 - 82 nm	39 nm	37 - 40 nm

2.4.2 Angular performance

Further features which may be of interest in many applications are the variation of the performance with respect to the incidence angle and the wavelength. Figure 2.6 reports the performance of the Design A and G as function of the incidence angle, still considering the nominal wavelength at 121.6 nm. Applying the criteria adopted for the nominal evaluation, the Design A is the most critical as the structure shows acceptable performance for incidence angles only range from 44° up to 50°. On the other hand, the performance of Design G are maintained over a large range of angles from 24°, where $R_{TE} = 0.705$, up to 49°.
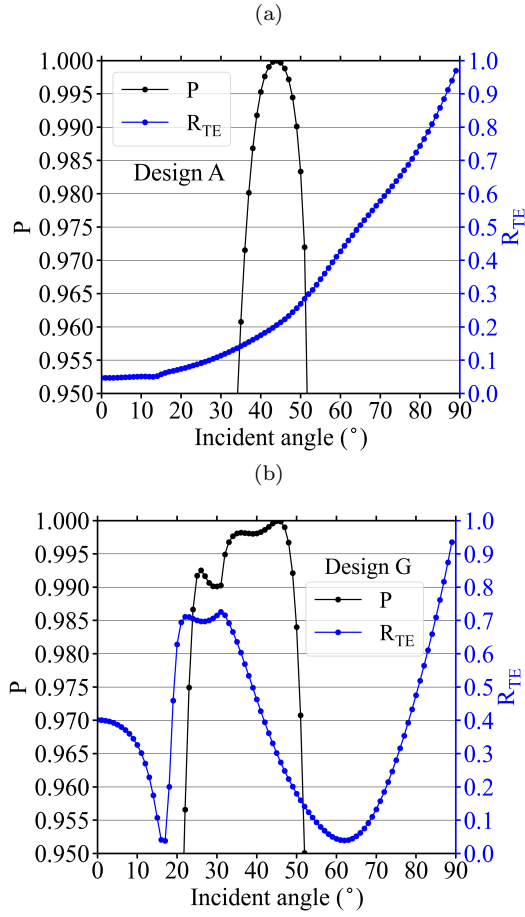
Figure 2.6: (a) polarization angular behavior of Design A, (b) polarization angular behavior of Design G

2.4.3 Spectral performance

Similarly, Figure 2.7 reports the performance change as function of the wavelength. In this case, both structures show a similar behaviour, although the Design G is better in term of TE-reflectance. In fact for the Design A the performance is acceptable in the wavelength range between 121.2 nm and 124.8 nm, while for the Design G the range increases from 118.6 nm up to 124.3 nm. The undesired losses which affect the TE-component in absorptive WGPs are highly dependent on the incident wavelength and angle, making this structure more sensitive to these parameters. Anyway, considering both angular and spectral performance, all those structures show valuable results although Design G is a little bit superior.
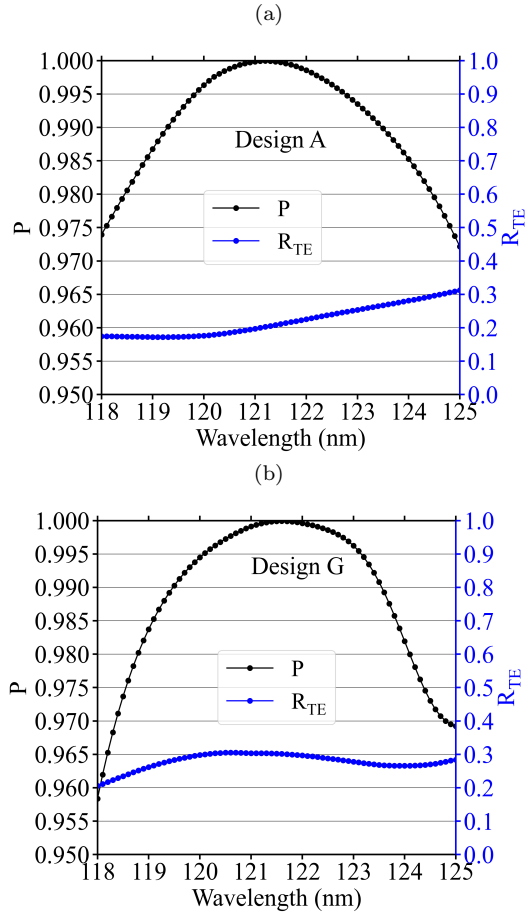
Figure 2.7: (a) wavelength behavior of Design A, (b) wavelength behavior of Design G

2.4.4 Nominal performance with other FUV polarizers

A comparison of the optimal structures' nominal performance with other experimental (T) or theoretical (E) demonstrated FUV reflecting polarizers are reported in Table 2.6. Polarizers based on MgF_2 plates and LiF_2 plates [76] tend to show lower TE reflectance. Au and silica mirrors' [76] polarization degree are easily reduced by the formation of surface films. Moreover, Au and silica mirrors need to work at a large incidence angle (i.e. $57.5°$ and $70°$). MgF_2/Al mirrors have been widely studied for realizing FUV polarizers, mainly due to their benefits in both polarization degree and TE reflectance [43, 47, 77, 78]. For example, three bilayers of MgF_2/Al realizes a TE reflectance of 0.69–0.725 and a polarization degree of 95.4%-97.2% [43], but their polarizing angles are also relatively large (i.e $65°$ and $70°$). Moreover, Al is easily to oxidize in the pro-

41

cess of MgF$_2$ deposition [47], the control of temperature becomes very crucial. In contrast, the proposed nano-wire reflecting polarizers showed a high polarization degree of 97.5% and large acceptance angles. In particular, the Design G provides an acceptance angle ranging from 24° to 49°, which would benefit future space missions.

Table 2.6: Nominal performance of optimal polarizers compared with other FUV reflecting polarizers

Structure	T/E	P	R/R$_{TE}$	Polarizing angles	long-term stability
Design A	T	>97.5%	>0.2	44°-50°	Relatively Good
Design G	T	>97.5%	>0.2	24°-49°	Relatively good
MgF$_2$ plate [76]	E	53%	0.2	45°	Reduced by formation of surface films
LiF$_2$ plate [76]	E	90%	0.11	60°	Reduced due to hygroscopic properties
Au mirrors [76]	E	68%	0.12	57.5°	Reduced by up to 20% by formation of surface films
Silica mirrors [76]	E	92%	0.29	70°	Reduced by up to 8% by formation of surface films
MgF$_2$/Al/MgF$_2$ [77]	T	97.31%	0.887	45°	Impacted by the temperature of MgF$_2$ deposition
(MgF$_2$/Al)$_2$ [47]	E	92%	0.69	66°	May be impacted by the temperature of MgF$_2$ deposition
(MgF$_2$/Al)$_3$ Sample 1 [43]	E	97.2%	0.69	65°	May be impacted by the temperature of MgF$_2$ deposition
(MgF$_2$/Al)$_3$ Sample 2 [43]	E	95.4%	0.725	70°	May be impacted by the temperature of MgF$_2$ deposition

2.5 Summary

In this chapter, the design of wire grid polarizers (WGP) intended for working at 121.6 nm wavelength (H Ly-α) have been investigated. Two different approaches were considered, one based on absorptive nano-wires on a Al/MgF$_2$ high-reflective mirror and the other one based on reflective nano-wires placed on a Si non-reflective substrate. The nominal performance required for considering

acceptable WGP solutions was a reflectance of 0.2 at the target wavelength and a polarization degree P of 99.9%.

Two promising structures were selected throughout the optimization process, both are composed of squared nano-wires. The first one, named Design A, is based on TiO_2 absorptive wires having a height of 38 nm, a width of 38 nm and placed with a pitch of 68 nm; simulations given a TE-reflectance of 21.4 % and a polarization degree P of 99.97% for this structure. Instead, the second structure, named Design G, is based on reflective wires obtained with the Al(150 nm)/MgF_2(65 nm) bi-layer with a width of 39 nm and a pitch of 80 nm; with this structure, a TE-reflectance of 30.1% and a polarization degree P of 99.99% can be achieved.

The robustness of the performance with respect to the width and pitch variation were investigated for the two promising structures. This evaluation is based on the determination of the range within each parameter can vary to maintain a variation of the polarization degree P less than 2% with respect to the nominal value and the TE-reflectance higher than 20%. For Design A, the performance remain acceptable when the pitch and width in the range of 62-70 nm and 33-40 nm whereas for the Design G in the range 79-82 nm and 37-40 nm, respectively. In conclusion, despite the Design G has a narrower ranges of robustness, this structure is the preferable candidate since it shows the best performance. This choice is further strengthened by comparing the angular and spectral ranges within which the performance remain acceptable: 44° up to 50° and 121.2 nm and 124.8 nm for Design A against 24° to 49° and 118.6 nm up to 124.3 nm for Design G.

3 TiN-based TM-pass waveguide polarizer for optic fiber communications

3.1 Background

3.1.1 Historical development of optical fiber communication

Optical fiber communication has been developed more than two centuries and is still under investigation. In the 1790s, a French engineer named Claude Chappe invented the first communication system, known as the 'optical telegraph'. In 1880, Alexander Graham Bell patented a photophone, which is used for speech transmission using a beam of light. In the 1920s, Engilsh J.L. Baird and American C. W. Hansell performed an experiment for images transmission using arrays of uncoated fiber cables. In the 1950s, A.V Heel and H. Hopkins developed a clear cladding with a lower refractive index to protect a raw glass. These achievements lead to the development of the flexible fiberscope, which is widely used in medical field.

By 1960, glass-clad fibers had reached an attenuation of 1 dB/m. This is suitable for imaging applications, especially in medical fields, but not for data transmission. The discovery of lasers in the 1960s opened a new area in modern optics, known as Photonics. Maiman demonstrated an experimental optical amplifier using lasers in the electromagnetic spectrum. However, the stability of long-distance lasers operating in millimeter-wace was reduced since the atmospheric turbulences such as clouds, rains, and frogs.

1970, Meaurer, KecK, and Schultz produced single-mode fused silica fibers operating at the wavelength of 633 nm, which shown a attenuation less than 2dB/km. This paved the way for long-distance optical communication. In 1997, multi-mode fibers were proposed and having a refractive index gradient between fiber core and cladding. This kind of fiber has an attenuation approximate 2dB/km operating at 850 nm. In the early 1980s, the first long-distance networks transatlantic backbone were established for telecommunication based on single-mode fiber and operate at 1300 nm. Even today, this technology is used as one of the industry standards for optical communications.

3.1.2 Generation of light wave systems

Optical fiber communication systems or light wave systems have been developed for many years and experienced 5 generations based on its operating wavelength and performance, as shows in Table 3.1.

Table 3.1: Five generations of light wave systems

Generation	wavelength (μm)	Fiber Type	Bite Rate	Fiber losses	Repeater Spacings
1st (1970s)	0.85	Multimode	2-45 Mbps	≥ 1	≃ 10 km
2nd (Early 80s)	1.3	Multimode	45-90 Mbps	0.5-1.0	≃ 40 km
3rd (late 80s)	1.55	Single mode	≥ 1.7 Gbps	≃ 3	≃ 60-70 km
4th (Early 90s)	1.45-1.62 (Typical 1.55)	Single mode (dispersion-shifted)	≥ 2.4 Gbps	≃ 0.2	≃ 80 km
5th (In 2000s)	1.50-1.57 (Typical 1.55)	Single mode +Fiber Amplifier	≥ 2.4 Gbps	0.1-0.2	≃ 100 km

1. ***First generation***. In the 1970s, the earliest optical fiber communication systems were produced and operating at the wavelength approximate 850 nm, the researchers used infrared LED and GaAs semiconductor lasers as optical source, a silica fiber as optical medium, and inexpensive photodetectors. These systems offered a data transmission rates of 50-100 Mbps with repeater spacing of 10 km. However, it suffered from a high attenuation (3 dB/km) and thus became less popular.

2. ***Second generation***. In the early 1980s, optical fiber systems were designed to operate near 1300 nm with lower loss (less than 1 dB/km). InGaAsP semiconductor lasers and detectors, as well as sing-mode fibers are employed, which allowed for 1-2 Gbps transmission data rates with repeater spacing greater than 40-50 km.

3. ***Third Generation***. In the 1990s, silica fibers operating at a wavelength of 1550 nm were produced, with minimum theoretical attenuation of 0.2 dB/km. These optical fiber transmission networks could deliver data rates of over 2.4 Gbps with repeater spacing more than 100 km.

4. ***Fourth Generation***. The spectral region for optical fiber communications extending from 1300 to 1650 nm with the implementation of the wavelength-division multiplexing (WDM) technique for enhanced data rate capacity and optical amplification methods for employing larger repeater spacings. By the year 2001, the light wave WDM systems provide 10 Tbps data rate within a repeater spacing of 60-80 km. In-line erbium-doped fiber amplifiers are used to compensate for the fiber losses.

5. ***Fifth Generation***. Following the availability of dry fibers, Roman amplification techniques, optical solitons. The spectral region extended its spectral region from 1300-1650 nm, enabling thousands of WDM channels to operate simultaneously at speeds of 40-160 Gpbs.

3.2   Motivation

The sophisticated optical fiber communications depends on many different key components such as optical transmitters, optical receivers, amplifiers, and various types of electronics. These optical and electronic components are typical examples of photonic integrated circuits (PLCs). In the last decade, Photonic Integrated Circuits (PICs) based on silicon attracts widespread interest for their suitability in many applications, such as optical sensing and communication [79,80], quantum photonics [81], and nonlinear optics [82]. This is mainly due to their compatibility with conventional CMOS technologies, high processing control, low cost, and high volume manufacturing. Most of these photonic devices are based on the silicon on insulator (SOI) technology, which exploits light confinement in a Si waveguide deposited onto SiO_2 structure, which is embedded in a cladding material, typically SiO_2 or air [83]. The high index-contrast between the silicon core and the cladding material enables the high-density integration of photonic components and generally introduces significant polarization dependence [84]. This feature causes the polarizaion-sensitive issues such as polarization mode dispersion (PMD), polarization dependent loss (PDL) and polarization depedent wavelength shift (PDWS) [85], degrading their practical performance, especially in the devices and systems operating with a single polarization (SP) such as on-chip photonic building blocks [86], fiber-optic gyroscope, electro-optic switching arrays, and optical communication modules [87]. Any deterioration in the purity of the operating polarization may result in significant performance degradation. Therefore, precise control of the polarization state of light is necessary in these optical circuits integration.

To overcome this issue, one of the promising solutions is to use polarization diversity schemes (PDSs), in which polarization-handling elements, such as polarizing beam splitters (PBSs) [88–91] and rotators (PRs) [92–95] are used to separately manipulate the TE and TM components. The working principle of PDSs is straightforward. A PBS is used to separate the impinging light into two orthogonal linearly-polarized beams (i.e. the TE and TM beams). The electric-field oscillation direction of one of them is then rotated into the orthogonal direction by using a PR, making it parallel to the other component. The two beams are separately processed by two identical PICs. A second PR is then used to restore the original polarization state of the beam. However, the polarization diversity scheme using both PBSs and PRs will increase the complexity and footprint of the whole device. An example of polarization diversity scheme in which the length of polarization splitter and rotator (PSR) is over 600 μm [79]

As a simple and efficient solution, polarizers are among the most important components for realizing high-dense PICs since their anisotropic behavior, which results in suppressing the undesired polarization state and making the desired one pass through.

When dealing with polarizers, the key features which must be taken into consideration are low insertion loss (IL), high extinction ratio (ER), compact footprint and ease of manufacture. So far, various types of polarizers based on

different concepts have been proposed. An example of TE-pass polarizer based on shallowly-etched SOI ridge waveguide has been proposed by Dai et all. [96], where an extinction ratio as high as 25 dB over a 100 nm wavelength range has been achieved with a 1mm-long polarizer. Also, TE and TM polarizers can be realized through sub-wavelength grating waveguides (SWG), where the SWG is designed to specifically support Bloch mode for one polarization state, which can in turn propagate with low losses, while working as a Bragg reflector for the orthogonal one, that is consequently reflected. For example, Guan et all. [97] fabricated and experimentally verified a TM-pass SWG of ~9 μm length with measured extinction ratio of ~27 dB and the less loss of ~0.5 dB at the central wavelength 1550 nm. Another SWG was reported by Xiong et all, which realizes an extinction ratio 30 dB and an average insertion loss of 0.4 dB [98], but with a relative long device length of 60 μm. In recent years, surface plasmon polaritons (SPPs) opened up the possibility to achieve ultracompact devices. Many different designs have been proposed, such as metal-insulator-metal (MIM) structures [85, 99–101], directional couplers (DCs) [102–104] and and hybrid plasmonic waveguides (HPWs) [105]. Polarizers based on special materials such as graphene [106–109], and vandium dioxide (VO_2) [110] are also reported. However, the graphene-based polarizer faced some uncertainties in the experiment, such as the shape, size, number of layers, and purity of graphene [111]. VO_2 as a phase-change material (PCM) needs a cooling process to return its insulating phase, whose phase-transition is volatile [112]. On the other hand, titanium Nitride (TiN) turns out to have many advantages, such as high thermal stability, bio-compatibility and manifacturability by epitaxial growth on a large number of substrates [113], and it is in turn a CMOS compatible material; it is, indeed, already employed in HPWs. An example of TM-pass plasmonic polarizer has been proposed by Azzam et all [114], which provides an IL of 1 dB and an ER of 20 dB at a 2.84-μm-long device. However, this extinction ratio is relatively low compared to previously mentioned designs, in fact, an higher extinction ratio would enhance the bit-error ratio (BER), reducing the number of errors and improving transmission efficiency [115]. Moreover, this TiN-based TM-pass polarizer uses a silicon dioxide layer surrounding the silicon core, which is challenging to be manufactured.

3.3 Design and modeling

3.3.1 Structure and materials

In this work, a different design of TM-pass hybrid plasmonic waveguide polarizer (HPW) is presented. The proposed polarizer and its cross-sectional view along the coupling are shown in Figure 3.1. A silicon waveguide of width w and height h is placed on top of the SiO_2 substrate, as in a typical SOI platform. Two TiN strips of width w_1, height h_1 and length L are placed sideways parallel to the main waveguide and separated by a distance g. A subsequent SiO_2 cladding was deposited to cover the whole structure. The two TiN strips act the attenuation of the TE-mode propagating in the silicon waveguide. Consequently, if the

strips are long enough, the TE-mode is fully absorbed. On the other hand, the TM-mode can propagate on the Si waveguide with a small attenuation.
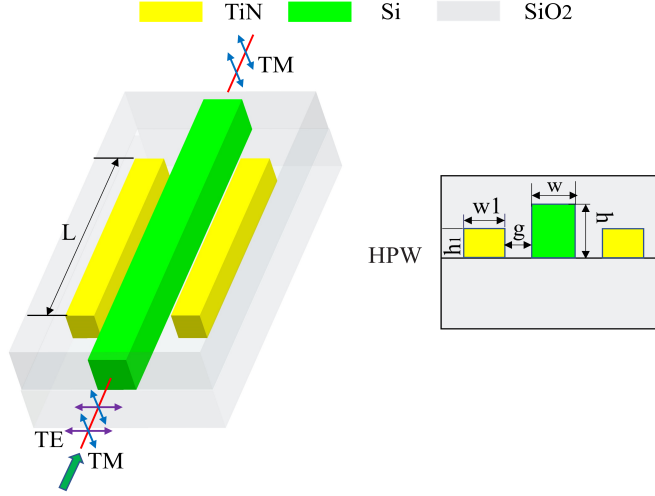

Figure 3.1: Concept and cross-section view of the proposed TM-pass waveguide.

3.3.2   Simulation description

The optimization of this device is carried out using the Wave Optics Module of Comsol Multiphysics via a Finite Element Method (FEM). Both 2D and 3D simulations are performed at the target wavelength of 1.55 µm. The refractive index of Si and SiO_2 considered in this work are 3.478 [116] and 1.444 [117], respectively.While at the workig wavelength, SiO_2 and Si have real refraction index, TiN has both a real and imaginary component, retrieved by the following dielectric function [118]:

$$\epsilon(\omega) = \epsilon_b - \frac{(\omega_p)^2}{\omega(\omega + i\gamma_p)} + \frac{f_1\omega_1^2}{(\omega_1{}^2 - \omega^2 - i\omega\gamma_1)} \ , \tag{3.1}$$

where $\epsilon_b = 2.485$, $\omega_p = 5.953$ eV , $\omega_1 = 3.954$ eV, $\gamma_p = 0.5142$ eV, $\gamma_1 = 2.4852$ eV, $f_1 = 2.0376$.

Firstly, a 2D simulation has been carried out to determine the optimal dimensions $w \times h$ of the central Si waveguide without considering the lateral TiN strips. Afterwards, 3D simulations have been used for the optimization of the TiN strips dimension $h_1 \times w_1 \times L$ and their distance g from Si waveguide, pursuing the maximization the value of extinction ratio (ER) and the minimization of the insertion loss (IL) as defined:

$$\text{ER} = 10 \log_{10} \frac{P_{\text{TM}}}{P_{\text{TE}}} \tag{3.2}$$

48

$$\text{IL} = -10 \log_{10} \frac{P_{\text{TM}}}{P_{\text{input}}} \tag{3.3}$$

where P_{TM} and P_{TE} are the TM and TE output powers, respectively, and P_{input} is the input one. An efficient TM-pass polarizer requires the TE mode to be attenuated as much as possible while the TM mode propagates with minimal losses. Such requirement results in a high extinction ratio and a simultaneously low insertion loss. Assuming w_1 set to 1 μm, which is a value large enough to induce the plasmonic effect, the 3D simulation goal is to find the optimal gap g between TiN strip and Si core, the length L of TiN strips, and the thickness h_1 of TiN strips.

3.4 Results and discussion

3.4.1 Optimization of silicon waveguide dimensional parameters

Figure 3.2 reports the mode effective refractive index (n_{eff}) computed for the TE and TM polarization states varying both the Si waveguide width and height from 100 nm to 400 nm, and support the selection of the dimension of the Si waveguide in order to allow/prevent the propagation of TE and TM modes. A mode can propagate along the waveguide if its effective refractive index is greater than that of the cladding material, which is 1.44 for this case. In Figure 3.2 TM mode is always at a cut-off when h is 100 nm, while a height greater than 300 nm allows its propagation. For what concern the TE mode, it propagates for all h values only when the waveguide width is larger than approximately 250 nm. A value of
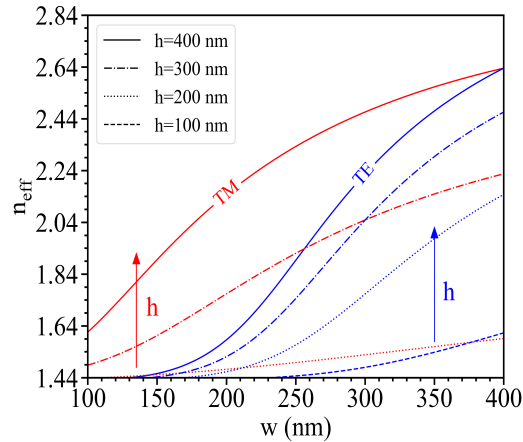

Figure 3.2: The mode characteristics of DW versus dimension parameters

220 nm is adopted in the present study, as such number is commonly used in SOI devices because of the numerous projects carried out in wafer foundries [119]. Moreover, Azzam and Obayya [114] report the considerable results of a TiN-based TM-pass plasmonic polarizer having the silicon waveguide width of such

size. Waveguide height between 300 nm and 400 nm are also very common value in SOI devices: for instance, some polarization beam splitters [120–122] and TM-pass polarizer [123] have been proven to perform well with a height of 340 nm. At this width, both TM and TE propagates.

3.4.2 Optimization of free geometrical parameters

Figure 3.3 reports the ER and the IL versus the three geometrical parameters L, g and h_1 for a fixed width and height value $w = 220$ nm and $h = 340$ nm respectively. The gap g between TiN strips and Si waveguide ranges with a step of 20 nm, while the strip height h_1 ranges with a step of 10 nm. Dots refer to values obtained with sampling step reduced to 5 nm. Different graphs
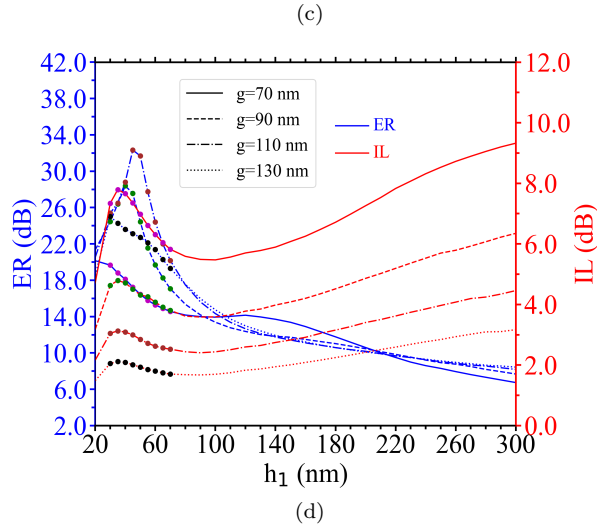
(a)

(b)
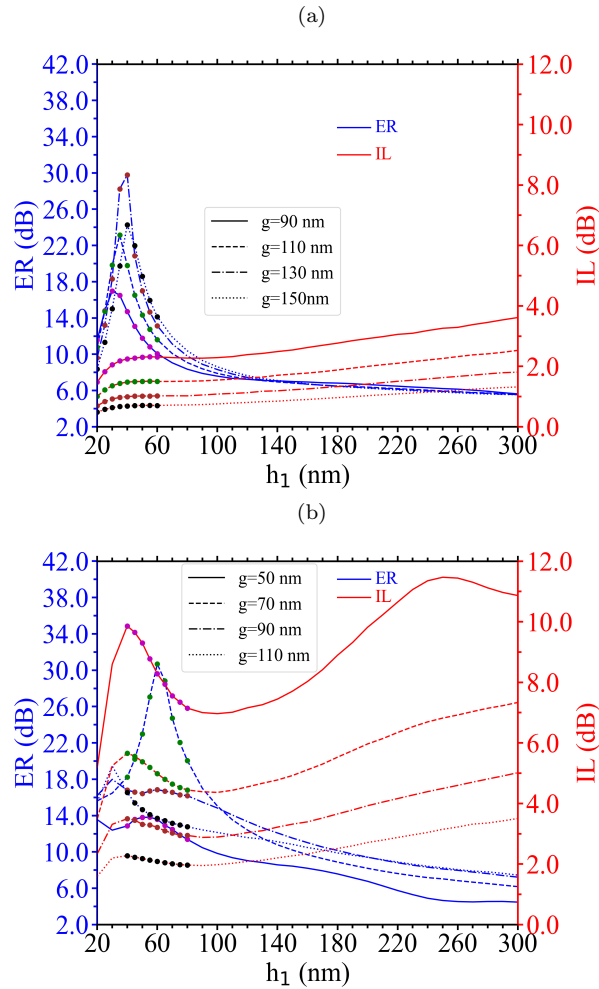
Figure 3.3: Extinction ratio and insertion loss versus free geometrical parameters: (a) $L = 2$ μm (b) $L = 3$ μm, (c) $L = 4$ μm, (d) $L = 5$ μm

correspond to the TiN strip lengths L ranging from 2 to 5 μm. For a given strip length L, the IL decreases as the gap g increases; this behaviour can be explained considering that the TM-component propagating in the SiO_2 slightly interacts with the TiN strips: both TiN-Si strips gap g and length L of TiN strips increase the propagation losses for TM. For given L and g values, the IL generally increases as the h_1 increases, although the curve initially shows a local maximum peak. A different behaviour characterized the ER versus h_1 curve, as for a given L, it shows a global maximum for any g; A different behaviour characterized the ER versus h_1 curve, as for a given L, it shows a

51

global maximum for any g. In Figure 3.4 a more detailed analysis around the g peak reported in Figure 3d by minimizing the variation step of g and h_1 into 1 nm (See Table 3.2). The optimal structure has been selected (See figure 3.4), being that realizing an ER of 60.7 dB and an IL of 2.23 dB with $L=$ 5 µm, $g = 136$ nm, and $h_1 = 44$ nm. This evaluation is based on the criteria: ER $\geq$ 30 dB, IL $\leq$ 3 dB.

Table 3.2: Sweeping ranges near the promising solution

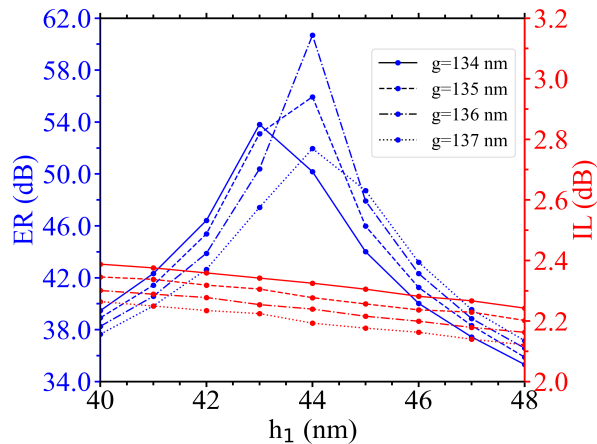| Promising solution	Sweeping ranges
L = 5 µm, g = 130 nm, h_1 = 40 nm	g: [110,150] nm, h_1: [30, 50] nm.

Figure 3.4: Extinction ratio and insertion loss versus free geometrical parameter in the promising areas: $L = 5$ µm, w = 220 nm, h = 340 nm.

3.4.3   A Comparison with some previous works on TM-pass polarizer

A comparison of this nominal performance with the TM-pass waveguide polarizers experimental and theoretical results available in literature is summarized in Table 3.3. Wu [124], Saber [125], and Prakash et al [134] reported a high extinction ratio TM-pass polarizer, respectively, but their designs are very challenging to fabricate. Moreover, Wu et al. [124] suffered from a relatively long device length (i.e 30 µm). Hu et al. [129] and Yuan et al. [135] reported a TM-pass waveguide polarizer with an ER of 40 dB and 45 dB, respectively; nevertheless, they are not CMOS compatible. Zhou et al [136] fabricated a TM-pass polarized with a extinction ratio of 40 dB, but this design is based on a hyperuniform disordered photonic structure (HUDPS) in which the fabrication process is time-consuming and probably expensive, making it difficult

Table 3.3: Nominal performance compered with TM-pass polarizer reported in literature.

	E/T	ER (dB)	IL (dB)	Length (μm)	Bandwidth (nm)	CMOS compatiblity
This work	T	60.7	2.23	5	140	Yes
Wu et al [124]	T	51.83	0.08	30	61	Yes
Saber et al [125]	T	45.4	1.7	8.8	72	Yes
Xu et al [126]	T	31.63	0.18	5.2	155	Yes
Rui et al [127]	T	28.3	0.4	10	65	No
Saber et al [128]	T	30.11	3.08	15	21.5	Yes
Bai et al [123]	T	25.6	0.088	2.5	Not mentioned	No
Hu et al [129]	T	40	3	150	200	No
Kim et al [130]	E	34	1	4	200	Yes
Zhang et al [131]	T	24	0.97	12	110	Yes
Elkader et al [132]	E	22	0.11	1	260	Yes
Dhingra et al [133]	T	38	0.05	20	200	Yes
Azzam et al [114]	T	20	1	2.84	Not mentioned	Yes
Prakash et al [134]	T	45	0.6	5	120	Yes
Yuan et al [135]	T	45	1	7.5	120	No
Zhou et al [136]	E	40	0.4	12.9	24	Yes
Sanchez et al [110]	T	15	3	1	60	Yes
Guan et al [137]	E	15.2	0.84	3.9	100	No
Guan et al [97]	E	27	0.5	9	60	Yes

to commercialize. On the contrary, this work realizes an ER as high as 60.7 dB in a compact length of only 5 µm and it is relatively to realize. Thus, the proposed structure is candidate to provide the highest ER ever reported in a very compact device.

3.4.4 The electric field distribution and power flow for optimal structure

In Figure 3.5 reports the electrical field distribution of TE and TM mode for both the DW and HPW, as well as the TE and TM mode power transmission flow from top view. It is vividly shown that the optical filed of TM mode in DW is mainly confined in silicon waveguide while in HPW it experienced a little bit loss since the slight interaction with TiN strips. In contrast, the optical field of TE mode in DW is mainly distributed in SiO$_2$ cladding, while in HPW it experienced a large mode distribution mismatch since the hybrid plasmonic effect, which further induces significant reflection loss [123]. When TM/TE mode transmission power is launched at the input port, the TE mode is quickly
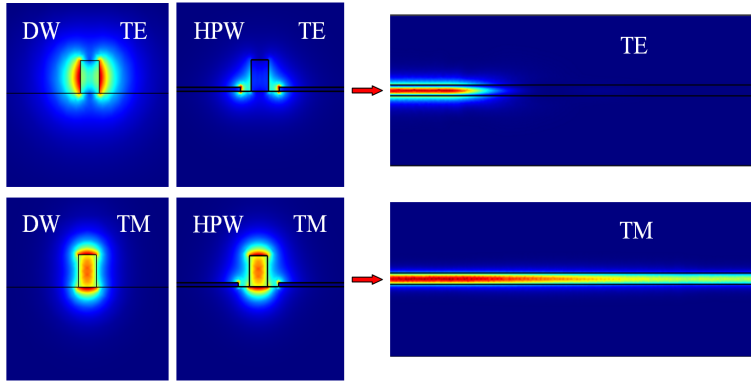
Figure 3.5: The electrical field distribution of TE and TM mode for both the DW and HPW, as well as the TE and TM mode power transmission flow from top view, for optimal structure

eliminated while TM mode is passed with a small amount of attenuation.

3.4.5 Wavelength behavior
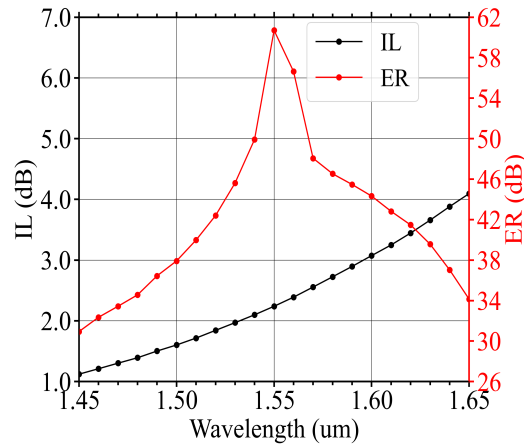
Figure 3.6: The IL and ER as a function of wavelength for optimal structure.

A further feature which may be of interest is the spectral performance. The ER and IL of the optimal structures is investigated in the wavelength region that ranges from 1.45 μm to 1.65 μm (Figure 3.6). It is found that the optimal structure performs well in a broadband wavelength range. For example, using the criteria: ER ≥ 30 dB and IL ≤ 3 dB, the wavelength guarantee this performance ranges from 1.45 μm to 1.59 μm, which is over 140 nm.

3.4.6 Manufacturing feasibility and sensitivity analysis

In evaluating the performance of the promising structures, it is needed to consider the challenges in manufacturing. Therefore, the tolerances of the optimal structure are investigated. It's worth noting that strips length L is relatively easy to guarantee from the manufacturing perspective, so only the variations of g and h_1 are considered. ER and IL values for changes of g and h_1 within ± 12

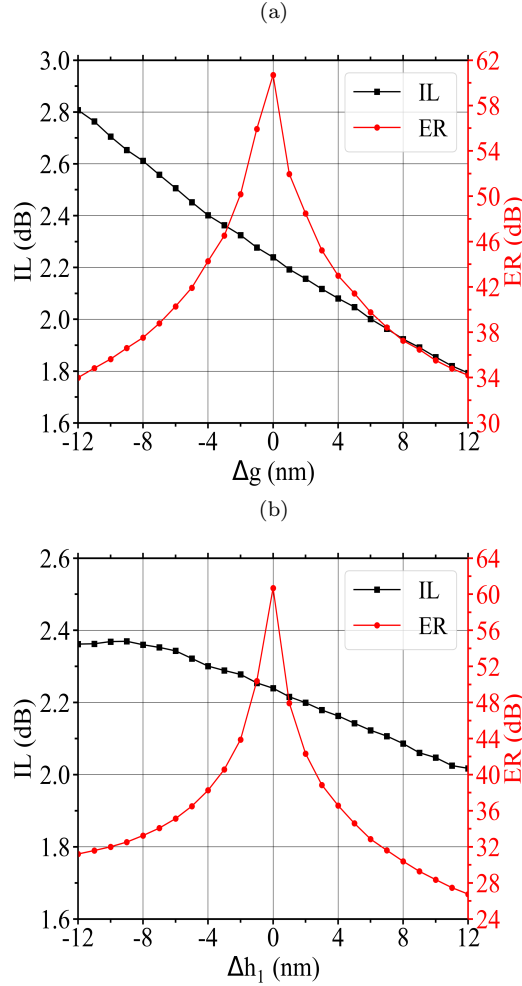Figure 3.7: The sensitivity of extinction ratio and insertion loss to free parameters g and h_1. (a) and (b) panels report the results for optimal structure

nm of each nominal value are reported in Figure 3.7, respectively. It can be seen that the IL is gradually decreases as both the g and h_1 increase, actually being more sensitive to g than h_1. The ER initially increases, peaks at a certain value

and then falls. The optimal structure realizes the largest ER of 60.7 dB and an IL of 2.23 dB at the nominal value of g and h_1. Let's still considering the criteria that previously established, variations of Δg and Δh_1 to the nominal value that can guarantee such performance are range from -12 to 12 nm and -12 to 8 nm, respectively.

The optimal structure could be fabricated on a SOI wafer and the silicon waveguide could be formed using electron-beam lithography (EBL) [138] or 193 nm DUV lithography [139], followed by a plasma reactive ion etching (RIE) process. TiN could be generated by plasma-assisted atomic layer deposition (PA-ALD) [140] or plasma-enhanced atomic layer deposition (PEALD) [141]. The SiO_2 cladding can be deposited using plasma-enhanced chemical vapor deposition (PECVD) [138]. Different SOI wafers typically have a different non-uniformity for the silicon layer thickness. For example, 200 mm wafers have a non-uniformity with a 3δ of ± 6 nm [142], but 300 mm wafers with a 3δ of ± 1 nm is realized [143]. The linewidth uniformity in the 193 DUV lithograph process is controlled with a 3δ of ± 8 nm [144]. These variations significantly impact the performance of the device.

3.5   Summary

In this work, A CMOS compatible TM-pass waveguide polarizer has been proposed and optimized at the target wavelength of 1.55 μm. Both 2D simulation and 3D simulation have been taken into consideration. The nominal performance required for the considered device is a higher extinction ratio and a lower insertion loss.

The optimal structure with the $g = 136$ nm, $h_1 = 44$ nm, and $L = 5$ um is selected, which realized an extinction ratio as high as 60.7 dB and an insertion loss of 2.23 dB. This extinction ratio is one of the highest values ever reported in a 5 μm device length. The spectral performance and sensitivity of the optimal structure is also investigated. These evaluations are based on the criteria: ER ≥ 30 dB and IL ≤ 3 dB. The wavelength that can provide such performance ranges from 1.45 to 1.59 μm. The robustness performance remains acceptable when the Δg, Δh_1 range from -12 to 12 nm and -12 to 8 nm, respectively.

Through analysis, this structure is relatively compact and easy to be fabricated, thus providing a good application prospect for high-dense PLCs.

4 Experiment preparation and fabrication plan

For the fabrication and characterization of optimal structures in the future, we contacted with the laboratory of Microfabrication, Institute of Physics, CAS, which posses many advanced manufacturing equipment and totally meet our requirements. According to sample requirements of the test platform in Institute for Photonics and Nanotechnologies (CNR-IFN) and Southern University of Science and Technology, a fabrication plan has been worked for each optimal structure and the specific manufacturing technical route is reported.

The process of nanofabrication usually needs to be treated with many different techniques and precise alignment. For example, Electron beam evaporation (E-beam), thermal evaporation, Plasma-enhanced chemical vapor deposition (PECVD), atomic layer deposition (ALD) are widely used in thin films deposition. These techniques are based on different working principles and deal with a variety of materials. Nano-imprinting lithography, direct laser writing, atomic spacer lithography, electron beam lithography (EBL), and extreme ultraviolet lithography (EUVL) are frequently used to define the desired patterns on photoresists. Some of these techniques allow for very small patterns, down to tens of nanometers in size. In particular, EUV lithography offer a pattern resolution down to several nanometers, this property enables the mass production of high-dense and high-performance semiconductors. Reactive ion etching (RIE) and Inductively Coupled Plasma Reactive-Ion Etching (ICP-RIE) are frequently used to remove the materials that are not protected by photoresist. The final step in the nanofarbication process is the photoresist removal, and microwave plasma remover is often used.

4.1 The general process of nanofabrication

The basic procedure of nanofabrication process is composed of substrate preparation, photoresist application, exposure and developing, etching, and photoresist removal.

Substrate preparation

The first step is to clean the surface of the wafer since it usually carried some organic or inorganic contaminations, which may result in defects in the patterns and cause poor adhesion between substrate and photoresist. Chemical treatment is usually used for removing contaminations on a substrate, such as hydrogen peroxide, trichloroethylene, acetone, and methanol [145]. Then, the wafer needs to experienced a dehydration bake to remove any moisture that may exist on the surface, typically treated at a temperature of 200° C to 400°C, lasting for 30 to 60 minutes. Finally, a adhesion promoter is added to improve adhesion between photoresist and substrate. It can react chemically with surface silanol and produce an organic functional substance, thus providing a good adhesion to photoresist. The most widely used substance for a adhesion promoters is Hexamethyl disilizane (HMDS).

Photoresist coating and bake

A thin, uniform photoresist with well controlled thickness is realized by a process of spin coating. The photoresist is rendered onto the liquid, which is then spun at a high speed on a turntable to produce the required film after the solid components are dissolved in a solvent. Precise thickness control and uniformity requirements, as well as low defect density call for particular attention to be paid to this process, where the photoresist thickness and uniformity are significantly impacted by a large number of parameters, such as spin speeds, times, the volume of resist dispensed, and the substrate topography.

After coating, the photoresist film contains 20-40% by weight solvent. Hence, a prebake is needed to remove excess solvent. The main purpose of this work is to stabilize the resist film. The solvent in unbaked photoresist films can be removed by evaporation at room temperature, affecting the characteristics of resist film with time. The majority of solvent is eliminated when the photoresist is baked, and the film becomes stable at room temperature. Removing solvent from a resist will cause four major effects: (1) reduce the film thickness, (2) improve adhesion, (3) Post-exposure bake and development properties are changed, (4) The film becomes less tacky, making it less vulnerable to contamination. There are several methods used for baking photoresists. Oven bake is a typical method. However, currently, hot plate is a more popular method to be used.

Alignment and exposure

The principle of operating a pattern on photoresist is the exposure light causes a chemical change that allows for removing some part of photoresist in a high resolution. There are several typical lithography methods: contact lithography, proximity lithography, and projection lithography (See Figure 4.1). Contact lithography use a photomask to contact photoresist directly and thus print the needed pattern. One example that making use of this principle is Nanoimprint technology. Although contact lithography offer a high resolution, but usually suffered from mask damage. Proximity printing will reduce the mask damage by keeping a distance between the mask and wafer. However, the resolution is limited, making it insufficient for today's mass production. At present, projection lithography is the most widely used method.

Projection lithography is to make an image of the mask projected onto the wafer. The most critical tools in a projection lithography are scanning and step-and repeat systems. Reflective optics (i.e., mirrors rather than lenses) are used to project a slit of light from the mask onto the wafer while simultaneously moving the mask and wafer. Exposure dose is impacted by many factors, such as the intensity of the light, the slit width, and scan speed. Over the past decades, scanners and steppers are dominate the lithographic patterning. The principle of scanners and steppers with different techniques are reported in Figure 4.2, respectively. It can be seen that the step-and-scan method exposes the complete 4 x reduction mask by using a fraction of a typical stepper field and scanning it
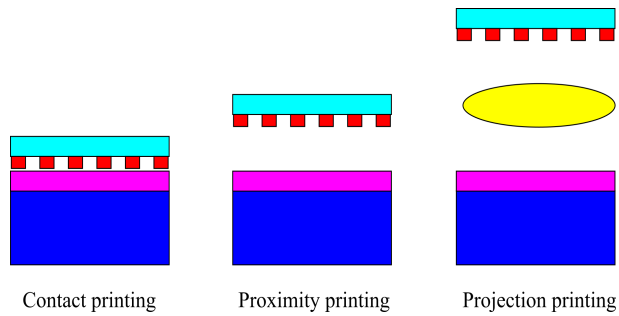
Contact printing   Proximity printing   Projection printing

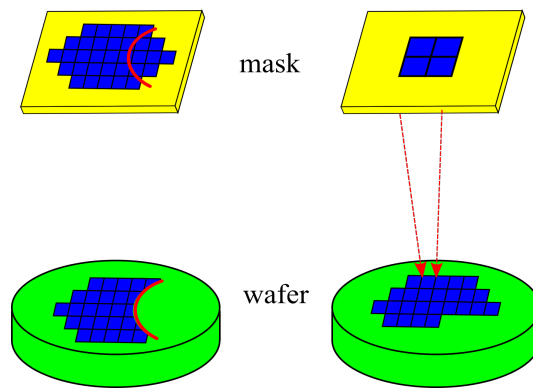Figure 4.1: Lithography methods

mask

wafer

Figure 4.2: The concept of scanners and steppers

in one direction. After then, the wafer is stepped to a new spot, and the scan is repeated.

Post-exposure bake and development

Post-Exposure Bake

Figure 4.3: The function of post-exposure bake

After UV light exposure, a post-exposure bake (PEB) is performed to reduce the standing wave effect induced by incident light's destructive and constructive

interference. The high temperature ($100°$ - $130°$) utilized are thought to produce photoactive compound diffusion, flattening down the standing wave ridges, as depicts in Figure 4.3.

Development is among the most critical steps in the photoresist process. Most photoresists use aqueous bases as developers. The interactions between resist and developers determine the photoresist shape and linewidth in a large extent. The employment of developers to photoresist plays a significant role in controlling the uniformity and process latitude. Various development methods have been proposed such as batch development, spin development, and spray development. In some scenario, a combination of these techniques are also used.

The resulting wafer is then "hard baked" to solidifies the resist to endure the harsh environment of implantation or etching. This process can make the image more thermally stable.

Etching

Etching is the process of transferring pattern into substrate by removing the upper layer of the substrate in the regions that are unprotected by photoresist. Dry etching techniques are commonly used in semiconductor production because they can be made anisotropic to avoid substantial undercutting of the photoresist pattern. It is noted that the linewidth of the pattern should be less or similar to that of thickness. Wet etch procedures are usually isotropic, which is important in microelectromechanical systems because suspended objects need to be "released" from the underlying layer.

Strip

The last step is to remove the remaining photoresist. This process often adopts a liquid "resist stripper", which chemically changes the resist, making it no longer adheres to the substrate. Another method uses a plasma containing oxygen to oxidize resist. This process is named ashing and resembles dry etching.

4.2 The equipment for manufacturing the optimal polarizers

4.2.1 Thin films deposition

The first step of the experiment is to deposit thin films on top of the wafer. E-beam, magnetron sputtering, ALD, and PECVD are introduced, which meet the requirements for the deposition of the desired materials. Al could be deposited by magnetron sputtering process [146], MgF_2 can be deposited using either E-beam evaporation [147] or Atomic layer deposition (ALD) [148], TiO_2 could be deposited by either E-beam evaporation [149]or magnetron sputtering [150], TiN could be deposited by ALD [151], and SiO_2 could be deposited by Plasma-enhanced chemical vapor deposition (PECVD) [152].

Electron beam evaporation is a type of Physical Vapor Deposition (PVD) in which the target material is strike with an electron beam and then to be used as coating. The electron beam is produced from a charged tungsten filament guided by electric and magnetic fields to strike the source material at the crucible and evaporate it in a vacuum environment. When the source material is heated to a thermal energy (less than 1 eV), the atoms of the source material will leave and reach the substrate, thus creating a coating on the substrate surface. The working distance is usually ranges from 300 mm to 1000 mm. Figure 4.4 indicates the structure and the principle of an E-Beam evaporator.

The E-beam evaporation device is mainly composed of two parts: an electron source and a depositing chamber. Electrons are generated from electron sources by thermionic emission. A negative high voltage (typically -4 to -10 KV) is employed to accelerate them as electron beams and an electromagnetic field is applied to deflect them into the crucible, which holds the evaporant material. The deposition chamber is where the target materials are evaporated, moved to the substrate, and deposited. The basic theory of evaporation rate for both liquid and solid surfaces was developed from early attempts to characterize evaporation processes using the kinetic theory of gases. The governed equation is

$$\Gamma_{ev} = 3.513 \times 10^{22} \frac{P_v}{\sqrt{MT}} \; molecules/cm^2 sec \qquad (4.1)$$

where the P_v is vapor pressure, M is molecular weight and T is the temperature. E-Beam evaporation offers much benefits in comparison with other deposition methods, such as high deposition rates, high material utilization efficiency, and low contamination for target material. The deposition rate can range from 0.1 nm/min to 100 nm/min, leading to a high-density film and a high adhesion to the substrate. The E-beam system only heats the target material instead of the entire crucible, resulting in less crucible contamination. In particular, a multiple crucible E-Beam evaporators can apply numerous layers of coating from different target materials without breaking the vacuum, making it adaptable to a variety of lift-off masking processes.

Magnetron sputtering is the other PVD process used for thin film deposition, by ejecting atoms from target material and condensing them onto the substrate in a high vacuum environment. A magnetron sputtering system and its working principle are reported in in Figure 4.5. A chamber is first evacuated to high vacuum in a conventional sputtering process to reduce the partial pressures and potential contaminants. After the base pressure has been established, the sputtering gas that makes up the plasma is pumped into the chamber, and overall pressure is controlled via a pressure control system. The sputtering electrons of the target material are accelerated away from the cathode, creating collisions with inert gas ions such as (Ar+). Such forceful collision make these ejected atoms travel to the substrate and start to condense into a film. As more atoms accumulated on the substrate, they begin to connect each other at the molecular level, generating an atomic layer that is tightly bounded. The thickness of such atoms layers depends on the sputtering time, allowing for the creation of accurate layered thin-film structures. There is a strong magnetic
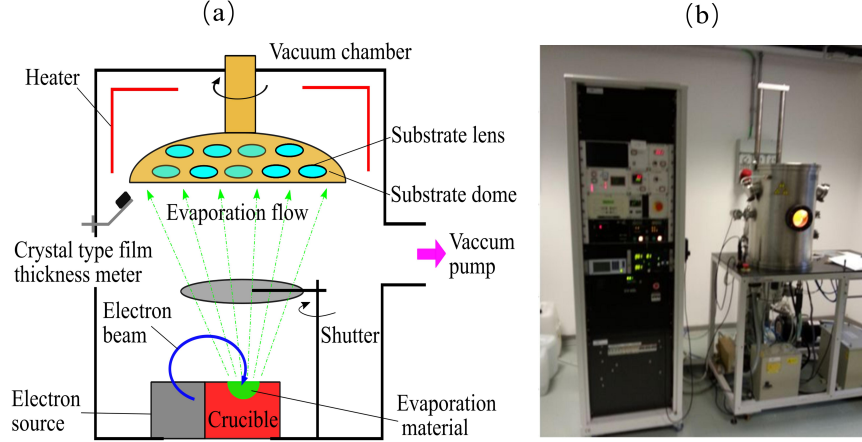
Figure 4.4: (a) The working principle of an E-beam evaporation device, (b) IONVAC e-beam and Joule evaporation system at CNR-IFN [153]

field near the target region in the magnetron sputtering system, which makes electrons travel linearly along magnetic flux lines. This has the advantage of confining the plasma to an area near the target, preventing damages to the thin film being created. Furthermore, electrons travel for a longer distance, increasing the likelihood of additional ionization of Argon atoms.

Sputtering field S is a key parameters to evaluate the sputtering efficiency, which is defined as

$$S = \frac{\text{Number of sputtered atoms}}{\text{Incident particle}} \qquad (4.2)$$

Sputtering process in the linear collision-cascade has been investigated by many researchers, but the commonly accepted theory is provided by Sigmund [154,155]. The Sigmund theory established specific sputtering field at both high and low energies, as show follows

$$S = \frac{3\alpha 4 M_1 M_2 E}{4\pi^2 (M_1 + M_2)^2 U_s} (E < 1keV) \qquad (4.3)$$

$$S = 0.168\pi\alpha\beta\frac{Z_1 Z_2 q^2 M_1 S_n(\epsilon)}{(M1 + M2)U_s} (E > 1keV) \qquad (4.4)$$

Where α is the measured efficiency of momentum transfer in collisions. M_1 and M_2 are molecular weight for struck atoms and target atoms, respectively,
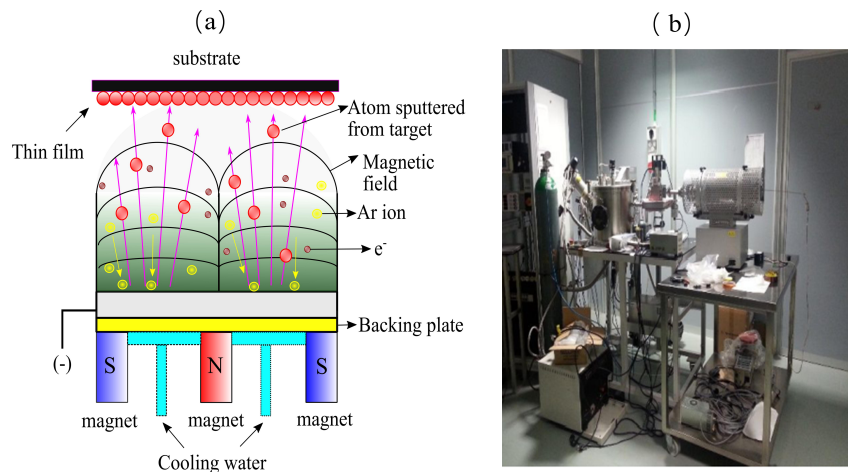
Figure 4.5: (a) The working principle of magnetron supttering, (b) RF magnetron facility at CNR-IFN, Padova [153]

E is the threshold energy required to transfer to target atoms, U_s is the binding energy of pushing atoms into the surface, q is the electrical charge, and β is the effective radius (0.1Å to 0.2Å) from over which electrons screen nuclear charge during collisions, $S_n(\epsilon)$ is defined as nuclear stopping power. Atomic layer deposition (ALD) is a thin film deposition technology that employs a gas-phase chemical process in a sequential manner. It is also a subclass of CVD. In ALD reactions, the precursors are used to react with surface of a material to generate the required substance. The precursors are pulsed alternately, one at a time in a sequential, self-limiting manner to avoid gas phase reactions (See figure 4.6a), which is a distinguish feature of ALD. The consecutive surface reactions are self-terminated, allowing for controlled growth of the desired material. Even on difficult 3D structures, such unique self-limiting development mechanism can achieve excellent conformality and thickness uniformity [157].

Dose times (the time a surface is being exposed to a precursor) and purge time (the time left in between doses for the precursor to evacuate the chamber) are used to describe the ALD process. ALD process is mainly evaluated by their growth per cycle, an ALD cycle is the does-purge-dose-purge sequence of a binary ALD process. In ALD, each reaction must be given enough time to obtain the complete adsorption density. The process has reached saturation when this occurs. The time will be determined by two important factors: the precursor pressure and the sticking probability [158]. The rate of adsorption
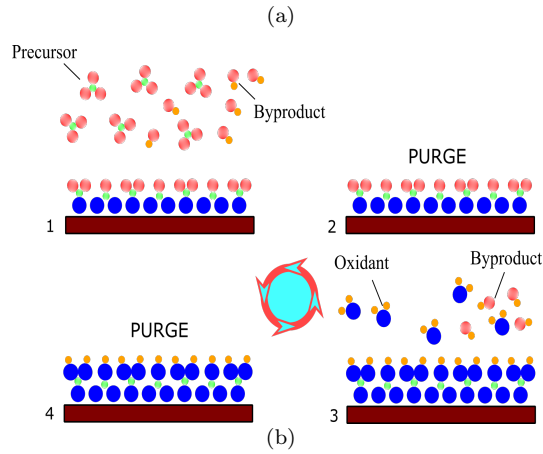
Figure 4.6: (a) The working principle of ALD, (b) Savannah-100 ALD system in the laboratory of Microfabrication, Institute of Physics, CAS [156]

per unit of the surface area is given by

$$R_{abs} = S * F \tag{4.5}$$

where the R_{abs} is the adsorption rate, S is the sticking probability, and F is the incident molar flux. ALD is played a significant role in fabricating semiconductor devices. The main reason is that ADL provides much benefits in producing very thin, conformal films with well controlled thickness and composition at the atomic level. ALD has many different types, such as thermal ALD, Plasma ALD, photo-assisted ALD, metal ALD, and catalytic ALD. These ALDs usually working in different conditions and using different precursors and reactants. Figure 4.6b reports a Savannah 100 Atomic Layer Deposition (ALD) system, which is able to deposit very conformal and precise thicknesses of various thin films.

Plasma Enhanced Chemical Vapor Deposition (PECVD) is a chemical vapor deposition that can deposit the thin films of various materials at a lower temperature. The process use the plasma to drive the reactions between the

species and the substrate, and thus forming the layer. Figure 4.7a shows a typical schematic diagram of PECVD systems, a flow of gas is entered the chamber and filled the space of two electrodes (a ground electrode and an RF-energized electrode), The reactant gases are excited into a plasma by capacitive coupling between the electrodes, which causes a chemical reaction and resulting in the reaction substance being deposited on the substrate. Such plasma has far more reactive components than conventional gaseous plasma, allowing reactions to take place at lower temperatures (between 100 and 400 °C), increasing the rate of deposition and, in some situations, even increasing the efficiency of certain reactions. The process is repeated in the PECVD system until the coating is reaches the required thickness and the reaction byproducts are removed by a pump below the chamber.
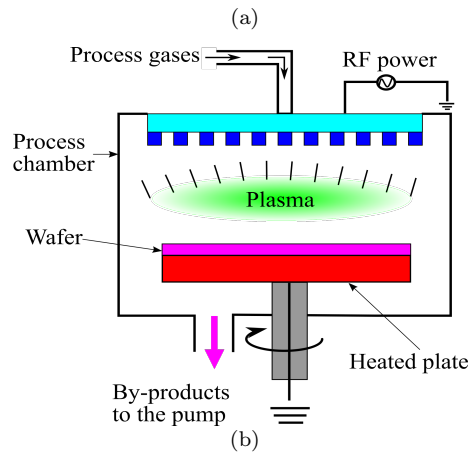

Figure 4.7: (a) The schematic process of a PECDV system, (b) the Inductively coupled plasma ICP-PECVD system (SI 500D) in the laboratory of Microfabrication, Institutes of Physics, CAS [156]

Figure 4.7b shows an Inductively coupled plasma (ICP) PECVD system, which could be used for depositing the materials consist of silicon nitride (SixNy), silicon dioxide (SiO$_2$), silicon oxy-nitride (SiOxNy), silicon carbide (SiC), and amorphous silicon (α-Si).

4.2.2   Photoresist spin-coating

Photoresist coating is a critical step in the fabrication of nano-devices. When dealing with a smooth surface. Spin-coating is typically used to form the thin films with the thickness down to nanoscales. A basic principle is shown in Figure 4.8 and a BSC-100 spin coating system is given in Figure 4.9, the resist is injected from the resist dispenser and then placed on top of the substrate, which is rotating at a speed of several 1000 rpm. The centrifugal force distributed the resist into a uniform film of the required thin film thickness. Excess resist is spun off the substrate edge. Simultaneously, a part of resist evaporates from the resist film, so that on the one hand, the thinning of the resits film is stopped, and on the other hand, the resist film is sufficient stable to prevent elapsing during subsequent wafer processing.
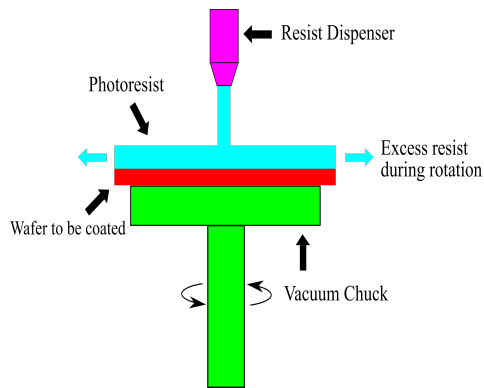

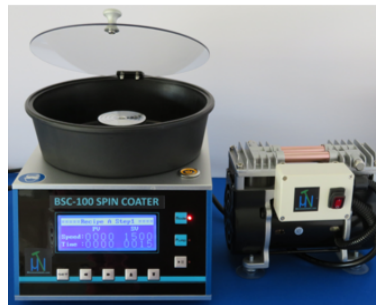Figure 4.8: The schematic diagram of spin-coating

Figure 4.9: BSC-100 spin coating system [156]

When dealing with relatively complicated 3D structures in which the spin coating is not technically feasible, the spray coating is used. A basic principle is reported in Figure 4.10 and a SCC-200 spray system is given in Figure 4.11. The resist film is generated from atomized photoresist with a droplet sizes. The droplets formed on the surface of the substrate through a nitrogen-filled nozzle or ultrasonic atomisation, where they are combined into a closed resistor film. There are some limitations in spray coating. The resist film is not very uniform in the surface of textured structure since the micro-turbulence, the resist film is generally thin at the top edges and thick in the grooves near the sidewalls. It's also difficult to form a very thin resist film (i.e < 1 um) because the landing position of droplets follows a statistical distribution.

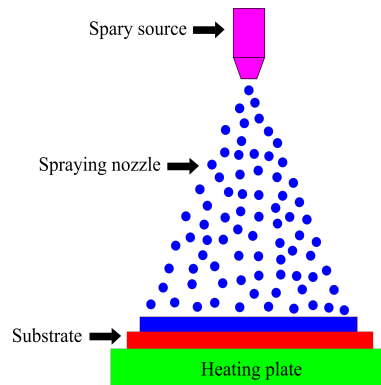Figure 4.10: The schematic diagram of spray-coating

Figure 4.11: SSC-200 spray coating system [156]

4.2.3 UV exposure

Electron-beam lithography

Electron-beam lithography (EBL) is a tool used for printing a pattern into a surface covered with resist by a tightly focused electron beam, which can

selectively remove the exposed or non-exposed region of resist in a developing. EBL allows for drawing very small patterns, usually with a resolution down to several nanometers. Subsequently, the exposed area can be further processed by etching. Unlike other photolithography technologies, EBL can write the pattern directly from the stored data instead of using pre-existing patterned mask, enabling the fabrication of nano-structrues in low volume. However, when dealing with a large exposure area, EBL is a relatively expensive and time-consuming method.
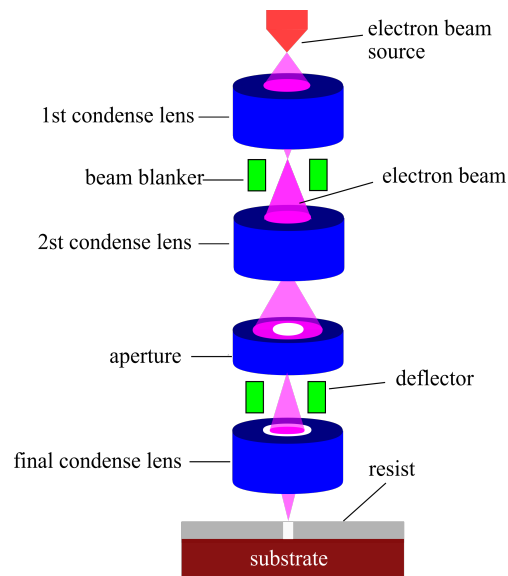

Figure 4.12: The structure of a typical electron beam lithography system

Figure 4.13: Electron beam lithography system JBX-6300FS, the laboratory of Microfabrication, Institute of Physics, CAS [156]

Figure 4.12 shows the typical structure of an electron beam lithography system. Electron beams are generated from electron beam source, and then tightly focused by condense lens onto photoresist to form an extremely small spot. A high-speed data processing system transfers the data from the hard disk to the blanking control system and beam deflector system. The beam blanker turns on and off the beam to print the pattern, and the deflector helps to print in the designated position. The desired pattern is achieved based on both electron beam movement and stage movement.

Table 4.1: The technical index for JBX-6300FS electron beam lithography system

Voltage	100 KV
SEM resolution	2 nm
Minimal linewidth	8 nm
Splicing accuracy	20 nm
Sample stage	equipped with 2-6 inch wafers

Figure 4.13 is an electron beam lithography system (JBX-6300FS), the main technical index is shown in table 4.1. It can be observed that the minimal linewidth can reach 8 nm, and stage allows for wafer size ranging from 2 to 6 inches. These features enable the fabrication of promising polarizers.

Extremely ultraviolet lithography

For more effective processing of lagre areas in microelectronic devices. Extremely ultraviolet lithography is frequently used, which is a technique that uses a EUV light wavelength near 13.5 nm to transfer the patterns to the substrate with a resist. It allows the small patterns with a half-pith below 20 nm that can't be achieved by traditional lithography technologies. Such cutting-edge EUV lithography system is considered the principal technology to create smaller, faster and powerful chips.

Figure 4.14 shows a schematic diagram of an EUV exposure system. A CO_2 pulse laser is used to generate 13.5 nm radiation, which is gathered using collection optics. The light from collective optics is shaped, directed by collective optics, and then illuminates the photomask mounted on a high scan-speed vacuum stage. The illumination optics consist of multilayer-coated normal incidence mirrors and grazing incidence mirrors. The mask is coated with a multilayer reflective coating and an absorber layer, etched into the creation of circuit layer. The process from mask to projection optics, which transfer a image of mask pattern with a demagnification (i.e. 4:1) to a recording wafer. The projection optics usually consist of six multilayer coated near-normal incidence mirrors. The final image is projected onto a silicon wafer with a photoresist. The wafer is also mounted on a vacuum-based stage with high scan speed. All these sub-systems from plasma source to wafer stage operate in a vacuum environment [159, 160].
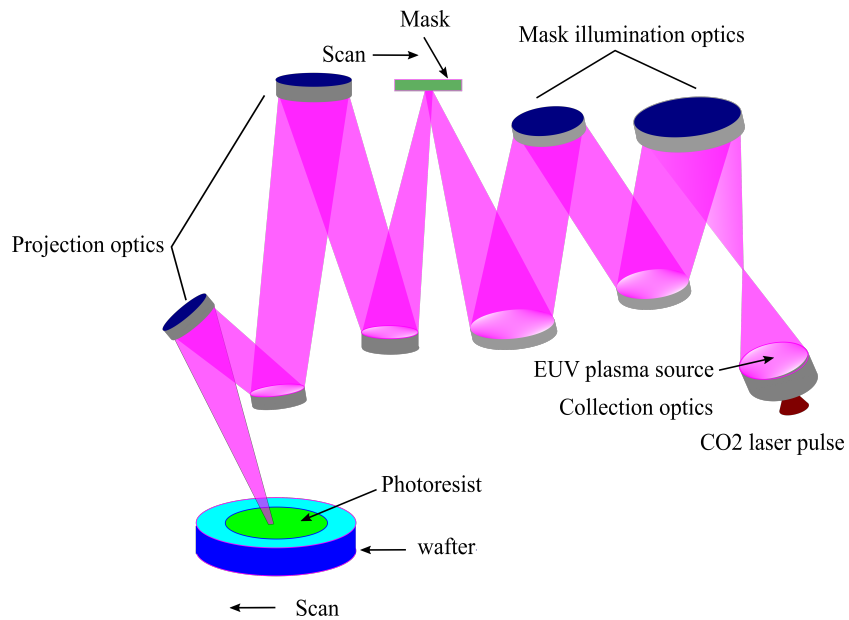
Figure 4.14: The schematic diagram of an EUV exposure system
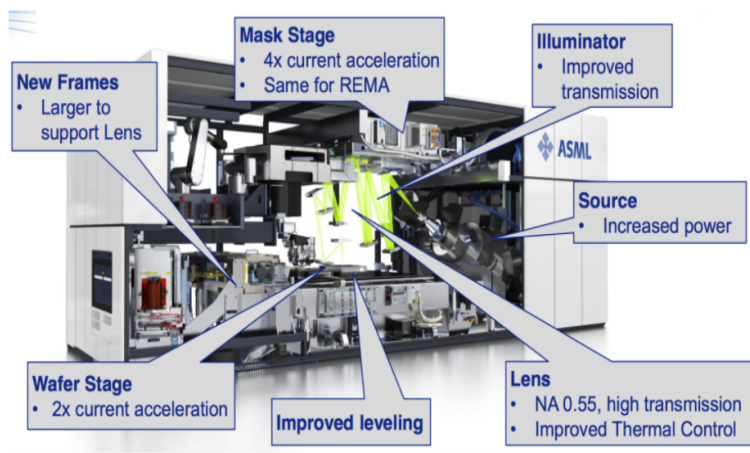
Figure 4.15: The EUV lithograph that used in Taiwan Semiconductor Manufacturing Company (TSMC) [161]

Figure 4.15 shows EUV lithography used for processing high-performance chips on Taiwan Semiconductor Manufacturing Company (TSMC), which is the dominant for 5N node's mass production, and the critical parts are depicted in the graph.

In order to achieve extremely high resolution patterns (i.e. ≤4 nm), EUV

interference lithography is used. The basic principle of EUV interference lithography is shown in Figure 4.16, where the inherent diffracted beam produces the pattern and is recorded by the photoresist. Assuming that the period of transmission grating is P and the diffracted angle is θ for the m diffraction order, following the Bragg equation, we obtained the interference pattern with the period T [162].
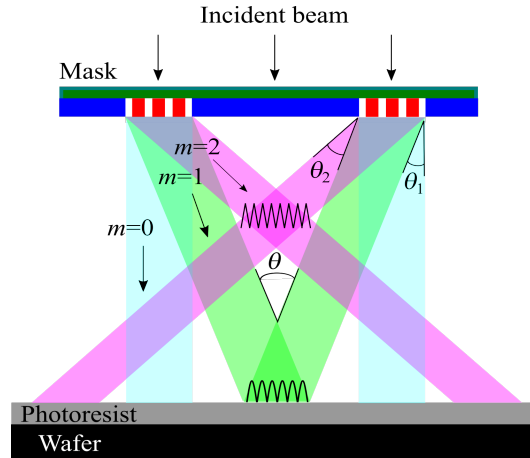

Figure 4.16: The scheme of EUV interference lithography. The EUV radiation incident at a transmission mask from the top. The mask was fabricated with transmission diffraction gratings. The diffracted beams generate an interference pattern which is projected onto the photoreisit on top of wafer

Figure 4.17: Extremely Ultraviolet Interference Lithography (EUV-IL) at Center for NanoTechnology, University of Wisconsin-Madison, Madison, WI, USA 53706 [163]

$$T = \frac{\lambda}{2\sin\theta} = \frac{P}{2m} \tag{4.6}$$

71

It can be noticed that the periodicity of the aerial image has a demagnification at 2:1 in comparison with the periodicity of diffraction grating for the first-order. This feature provides a very high resolution for EUV interference lithography. The distance g between the transmission mask and sample is given by

$$g = \frac{d}{2 \tan \theta} \tag{4.7}$$

where the d is the distance between the centers of two diffraction gratings on the mask. On the other hand, the zero-ordered diffracted beams are transmitted directly through the grating and don't cause overlap on the interference area. The second-order diffracted beams produce interference at a smaller distance from the mask and show a low diffraction efficiency. In most conditions, the first-order diffracted beam interference is relatively easy to be employed since its high diffraction efficiency [164]. Figure 4.17 reports an EUV interference lithography in the University of Wisconsin-Madison.

4.2.4 Etching

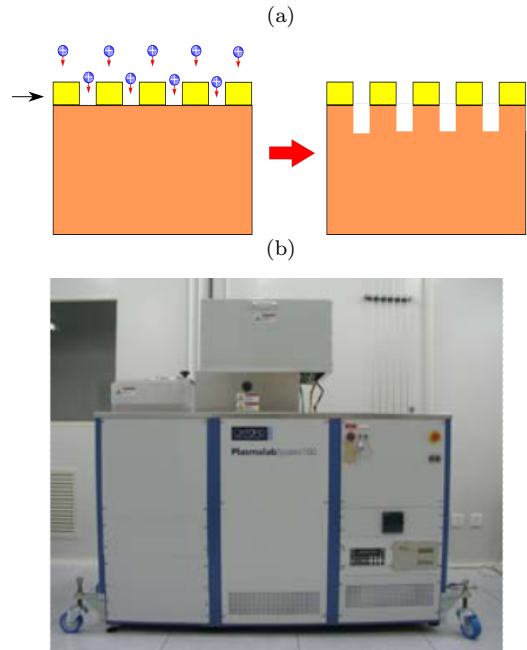
Figure 4.18: (a) The principle of reactive ion etching (RIE), (b)inductively coupled plasma reactive ion etching system (PlasmalabSystem 100), Laboratory of Microfabrication, Institute of Physics, CAS [156]

Reactive ion etching (RIE) is a technique that used for etching materials by reactive gas discharges. The basic principle of RIE is shown in Figure 4.18a, the

gas plasma generates the charged ions to impinge the structure shaped by UV exposure. The areas are not protected by photoresist will chemically react to the incident ions, and form the desired structure. In some cases, deep reactive ion etching (DRIE) is needed since it allows the high rate etching of deep structures. The etching process enables the chemical-physical removal of both isotropic and anisotropic etchings. In addition, RIE provides good results for the structure with very small dimensions. Therefore, this technology is widely used for the production of topographical micro-nano devices.

A typical RIE system is composed of a vacuum chamber, a wafer platter installed in the bottom of the vacuum chamber. The process gases enter through a small inlet at the top of the chamber. The by-products are exit through vacuum pump system in the bottom. Figure 4.18b shows an inductively coupled plasma reactive ion etching system. In such RIE system, the plasma is generated by a strong RF (radio frequency) electromagnetic field, the oscillating electric field ionizes the gas molecules by stripping them of electrons. The main technical indexes are reported in table 4.2, it can be seen that the minimal linewidth in this system can reach 30 nm, and the ratio of depth to width can reach 30:1. In comparison, in promising structures, the minimal linewidth is 30 nm and the largest ratio of depth to with is approximately 7. This demonstrates the desired grating structures could be realized.

Table 4.2: The main technical index of inductively coupled plasma reactive ion etching system (PlasmalabSystem 100)

Gas	Cl_2,BCl_3,$SiCl_4$, HBr, CH_4, O_2,Ar, CF_4, CHF_3, C_4F_8, SF_6
Sample sizes	up to 4 inches
Maximum RF power	RIE: 6000 W
Temparature conntrol range	-130°C-150°C
Etching material	Si, SiO_2, III-V semiconductors, Oxides
Etching precision	The minimal linewidth 30 nm, the largest ratio between the depth and width 30:1, adjustable angle in the inclination of sidewall 85°-92°

4.2.5 Photoresist Striping

The final step in nanofabrication is often the removal of photoresist, which aims to eliminate the photoresist material from the wafer as quickly as possible. The stripping method falls into three types: organic stripping, inorganic stripping, and dry stripping. Organic stripping uses chemicals to destroy the structure of the resist layer. The most widely-used organic strippers are phenol-based. Inorganic stripping is to heat the sulfuric acid and oxidant to finish the removal, usually remove the resist from non-metalized wafers. Dry stripping removes the photoresist by dry etching using a plasma equipment, which exhibits advantages such as safety, no metal ion contamination, and less tendency to attach under-

lying substrate layers. Figure 4.19a reports a microwave plasma photoresist remover (PS210). It is carried out under low-pressure plasma where the plasma reacts with the organic layer and burns the photoresist to ash (See Figure 4.19b.

(a)

(b)
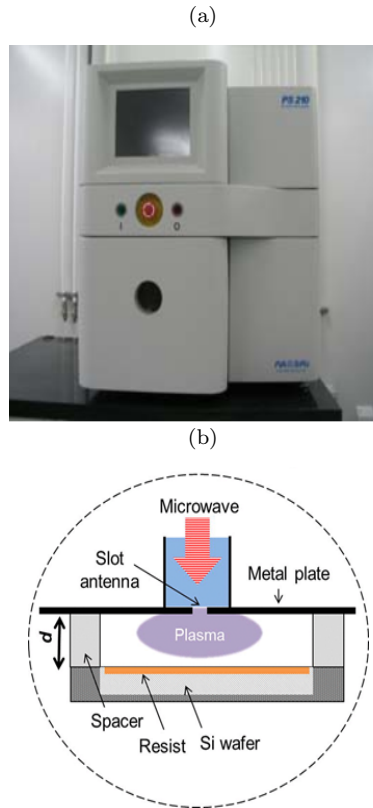
Figure 4.19: (a) The working principle of microwave plasma remover [165], (b) Microwave plasma remover (PS210), Laboratory of Microfabrication, Institute of Physics, CAS [156]

4.3   Manufacturing Solutions for optimal reflected WGPs

Considering the manufacturing equipment we introduced, different manufacturing technical routes have been worked out for optimal polarizers. Figure 4.20 and 4.21 show the specific dimension parameters and the required precision for Design A and Design G, respectively. The needed exposure area of grating is 1cm×1cm on top of the wafer.
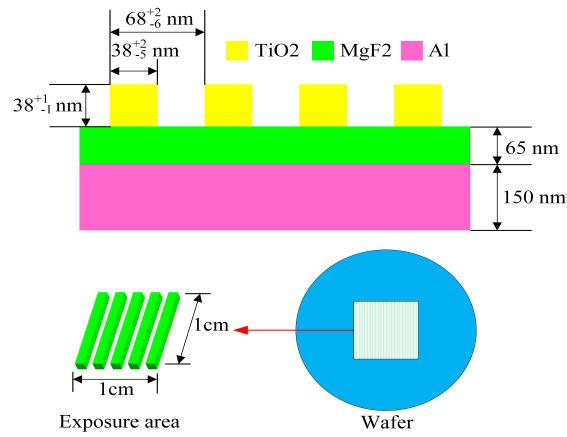
Figure 4.20: The process parameters and precision for the Design A
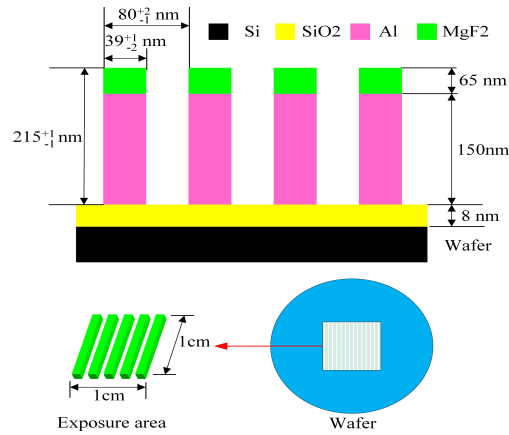
Figure 4.21: The process parameters and precision for the Design G

Two different technical routes are proposed for the fabrication of Design A. The two technical routes are depicted in Figure 4.22 and 4.23, respectively. In the first route, the initial work is to choose a proper wafer and deposit the Al/MgF_2 thin films. Then a spin-coating is carried out and a subsequent UV exposure to define the TiO_2 grating patterns, followed by a TiO_2 deposition. Finally, remove the remaining photoresist on the wafer. In the second route, the initial work of depositing Al/MgF_2 thin films is similar and then a TiO_2 thin film deposited on top of Al/MgF_2 thin films directly. Then a spin-coating is performed and a UV exposure to define the TiO_2 pattern on photoresist. A subsequent etching process is carried out to remove the TiO_2 that are not protected by photoresist and form the TiO_2 grating. After removing the remaining photoresist, the desired structure is obtained. Both the two methods allow for

75

the fabrication of desired structures, but the first method may provide a higher precision since the etching process usually brings some irregular shape in the position of sidewalls.

For the optimal structure Design G, only one solution is considered, mainly because of its relatively complicated structure and deep nanowire. In particular, the deep nanowire is easier to be realized by an etching process. Therefore, the solution involving the etching process is prefered. As is shown in Figure 4.24, the initial work is to deposit all the thin films (i.e SiO_2 /Al/MgF_2) on the wafer. Then a spin-coating is carried out and a subsequent UV exposure to define the pattern of nanowires. The next step is an etching process to form the desired Al/MgF_2 grating. After remove the remaining photoresist, the desired structure is obtained.
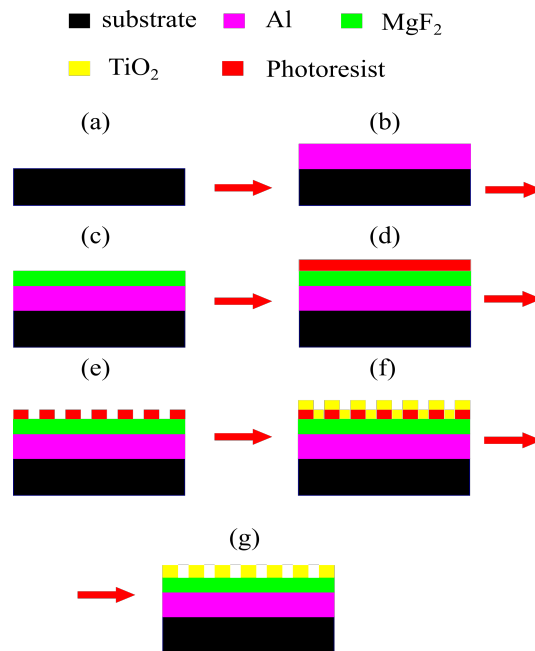
Figure 4.22: The first manufacture technical route of design A
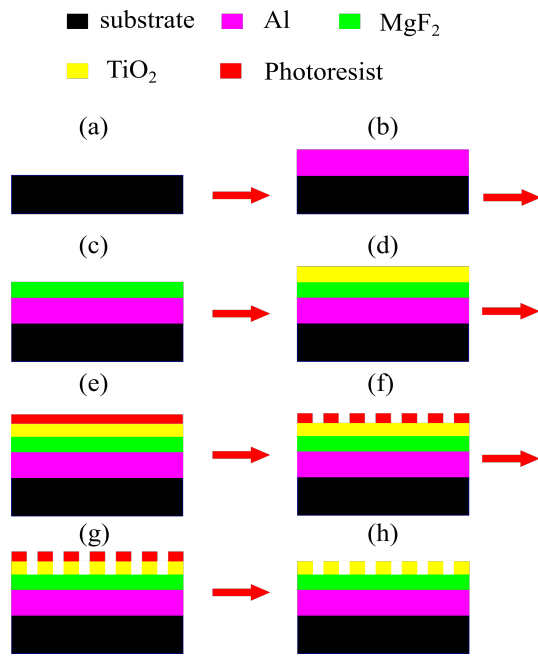
Figure 4.23: The second manufacture technical route of design A
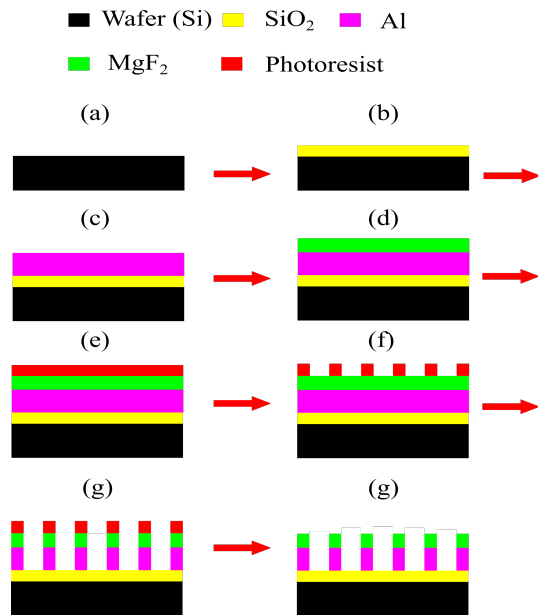
Figure 4.24: The manufacture technical route of Design G

77

4.4 Manufacturing Solution for optimal TM-pass waveguide polarizer
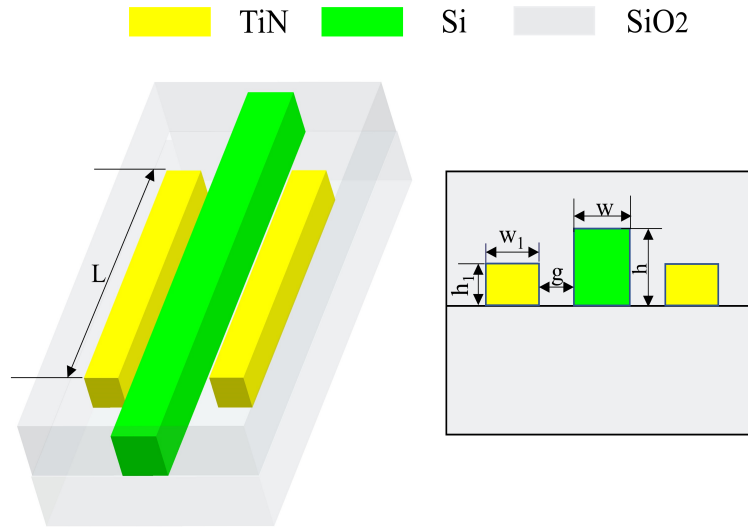
	Geometrical parameters and the tolerance for free parameters					
	w (nm)	h (nm)	w_1 (um)	h_1 (nm)	g (nm)	L (um)
Optimal structure	220	340	1	44^{8}_{-12}	136^{12}_{-12}	5

Figure 4.25: The process parameters and tolerance of optimal TM-pass polarizer

The geometric paramaters of optimal TM-pass polarizers and their tolerance to free parameters are reported in Figure 4.25. By using previously introduced equipment, such polarizers also could be manufactured. The manufacturing process is shown in Figure 4.26. Firstly, selecting a standard SOI wafer with a 340 nm top silicon layer, a photoresist was spun coated on top of the wafer, and electron beam lithography (EBL) was used to create the Si waveguide pattern. Then a etching process was performed to obtain the Si waveguide and still retaining the photoresist on top of that. A subsequent spray-coating process is performed since a 3D structure needs to be coated. Again, UV exposure is exploited to define the pattern of the TiN stips, followed by a TiN deposition. After removing the photoresist, a SiO_2 layer was covered to form the desired structures.
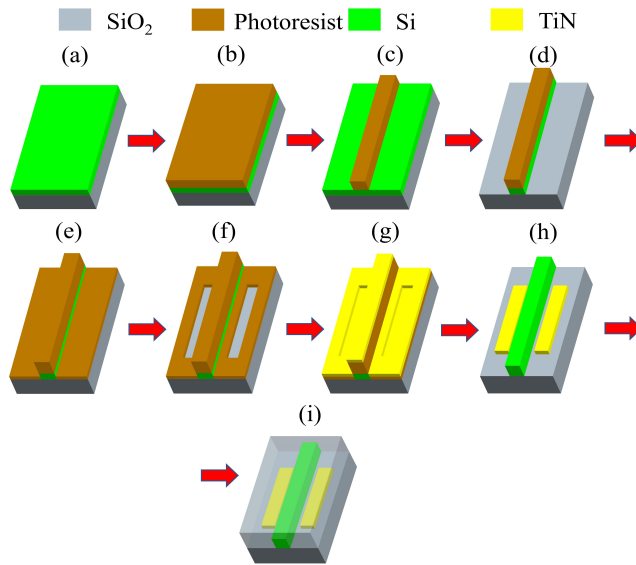
Figure 4.26: The fabrication process of TM-pass waveguide polarizer

5 conclusion

Control of the polarization state of the light is key element in many different applications. In this work, we designed and optimized two different types of polarizers for light manipulation at far ultraviolet and near infrared spectrum region, respectively. One is work at the Hydrogen Lyman α line 121.6 nm to perform polarimetric observation on the Sun. The other one is work at 1.55 um to realize high-dense PLCs for next generation of optical fiber communications. All of these works are carried out in Comsol multiphysics via a finite element method. The optimal structures are selected and the manufacturing feasibility are discussed. In view of the equipment in the Laboratory of Microfabrication, Institute of Physics, CAS and CNR-IFN, Padova, the fabrication plan is worked out.

For the observation at Hydrogen Lyman α line, two different concepts of reflected WGPs have been proposed and optimized. One is based on high-absorptive nano-wires placed on top high reflected thin films, the second one is based on high-reflective nano-wires placed on top high absorptive thin films. Different shapes and materials for the nano-wires are considered. The desired performance is a polarization degree greater than 99.5% and a simultaneous TE-reflectance greater than 0.2. Two very promising structures have been selected and both of them are composed of squared nano-wires. The first one is based on TiO2 absorptive nano-wires, named desgin A, having a height of 38 nm, a width of 38 nm, and a pitch of 68 nm, giving a polarization degree of 99.97% and a TE-reflectance of 21.4%. The other structure is based on the high reflective wires Al(150 nm)/MgF2 (65 nm) bi-layer, named design G, having a width of 39 nm and a pitch of 80 nm. This structures exhibits a polarization degree of 99.99% and a TE-reflectance of 30.1%. The robustness of the two promising polarizers with respect to the wires' width and pitch variation were investigated. This evaluation is based on the determination of the range within each parameter can vary to maintain a variation of the polarization degree P less than 2% with respect to the nominal value and the TE-reflectance higher than 20%. For Design A, the performance remain acceptable when the pitch and width in the range of 62–70 nm and 33–40 nm whereas for the Design G in the range 79–82 nm and 37–40 nm, respectively. In conclusion, despite the Design G has a narrower ranges of robustness, this structure is the preferable candidate since it shows the best performance. This choice is further strengthened by comparing the angular and spectral ranges within which the performance remain acceptable: 44° up to 50° and 121.2 nm and 124.8 nm for Design A against 24° to 49° and 118.6 nm up to 124.3 nm for Design G. Finally, the fabrication plan have been worked out. Two different manufacturing technical routes are proposed for Design A. The main difference is that one needs a etching process to pattern the TiO_2 nano-wires while the other one uses thin films deposition to obtain TiO_2 nano-wires. One manufacturing technical route is proposed for Desgin G since the deep Al/MgF_2 nano-wires is relatively easy to guarantee by a etching process.

For realizing high-dense PLCs at 1.55 μ, a hybrid plamonic waveguide TM-

pass polarizer has been proposed and optimized. This device is based on silicon on insulator (SOI) platform and placed two TiN strips parallel to the main silicon waveguide, a subsequent SiO_2 cladding is deposited to cover the whole structure. The working principle is the generated TE mode is gradually attenuated by two TiN strips while the TM mode is able to pass with a small amount of attenuation. The desired performance is a high extinction ratio, a low insertion loss, a small footprint, and easy to manufacture. Firstly, a 2D simulation is carried out to investigate the mode characteristics of the silicon waveguide, which helps to select the optimal Si waveguide dimensional parameters. Then a 3D simulation is performed to obtain the other optimal geometrical parameters by considering the value of extinction ratio and insertion loss, as well as device length. The structure with the $g = 136$ nm, $h_1 = 44$ nm, $L = 5$ um, $h = 340$ nm, and $w = 220$ nm, is selected as optimal structure, which realizes an extinction ratio as high as 60.7 dB and an insertion loss of 2.23 dB. To the best of our knowledge, this extinction ratio is the highest value ever reported. The optimal structure's spectral performance and sensitivity to free parameters are also investigated. These evaluations are based on the criteria: ER $\geq$ 30 dB and $\leq$ 3 dB. The wavelength that can provide such performance ranges from 1.45 to 1.59 µm. The robustness performance remains acceptable when the Δg, Δh_1 range from -12 to 12 nm and -12 to 8 nm, respectively.

Our finds believe that the proposed wire grid reflecting polarizers and TM-pass waveguide polarizers have a great potential for widely using in corresponding applications. Further work is the manufacturing and the characterization of these optimal polarizers to provide more convinced data and put them into real application.

Publications during my PhD

ISI journals

1. Zhao, Zhuan, Alain Jody Corso, and Maria Guglielmina Pelizzo. "Nanowire Grid Reflecting Polarizers for Ultraviolet Applications." IEEE Photonics Journal 12.6 (2020): 1-11.

2. Zhao, Zhuan, Giovanni Santi., Alain Jody Corso, and Maria Guglielmina Pelizzo. "Demonstration a high-extinction ratio TiN-based TM-pass hybrid plasmonic waveguide." Optica Applicata (Under review).

Proceedings to conference

1. Zhao, Z., Tessarolo, E., Corso, A. J., & Pelizzo, M. G. (2020, April). Optical Simulation of Triangular Wired Grid Polarizer for Far Ultraviolet Applications. In IOP Conference Series: Materials Science and Engineering (Vol. 809, No. 1, p. 012024). IOP Publishing.

References

[1] Eugene Hecht. *Optics, 5e*. Pearson Education India, 2002.

[2] David L Windt. Imd—software for modeling the optical properties of multilayer films. *Computers in physics*, 12(4):360–370, 1998.

[3] Farhan Rana. Semiconductor optoelectronics. *Cornell University. Lecture notes*, 2016.

[4] Qingzhong Deng, Qiaojing Yan, Lu Liu, Xinbai Li, Jurgen Michel, and Zhiping Zhou. Robust polarization-insensitive strip-slot waveguide mode converter based on symmetric multimode interference. *Optics Express*, 24(7):7347–7355, 2016.

[5] George Bekefi and Alan Hildreth Barrett. *Electromagnetic vibrations, waves, and radiation*. Mit Press, 1977.

[6] J David Pye. *Polarised light in science and nature*. CRC Press, 2015.

[7] Randy O Wayne. *Light and video microscopy*. Academic Press, 2019.

[8] Seth Stein and Michael Wysession. *An introduction to seismology, earthquakes, and earth structure*. John Wiley & Sons, 2009.

[9] WHT Vlemmings. A review of maser polarization and magnetic fields. *Proceedings of the International Astronomical Union*, 3(S242):37–46, 2007.

[10] Latham A Boyle, Paul J Steinhardt, and Neil Turok. Inflationary predictions for scalar and tensor fluctuations reconsidered. *Physical review letters*, 96(11):111301, 2006.

[11] Max Tegmark. What does inflation really predict? *Journal of Cosmology and Astroparticle Physics*, 2005(04):001, 2005.

[12] Masud Mansuripur. *Classical optics and its applications*. Cambridge University Press, 2002.

[13] Yoshihiko Arita, Michael Mazilu, and Kishan Dholakia. Laser-induced rotation and cooling of a trapped microgyroscope in vacuum. *Nature communications*, 4(1):1–7, 2013.

[14] Larry J Paxton, Robert K Schaefer, Yongliang Zhang, and Hyosub Kil. Far ultraviolet instrument technology. *Journal of Geophysical Research: Space Physics*, 122(2):2706–2733, 2017.

[15] ISO Standard. 21348."definitions of solar irradiance spectral categories.".

[16] Silvano Fineschi, Richard B Hoover, Juan M Fontenla, and Arthur BC Walker II. Polarimetry of extreme ultraviolet lines in solar astronomy. *Optical Engineering*, 30(8):1161–1168, 1991.

[17] JO Stenflo, D Dravins, N Wihlborg, A Bruns, VK Prokof'ev, IA Zhitnik, H Biverot, and L Stenmark. Search for spectral line polarization in the solar vacuum ultraviolet. *Solar Physics*, 66(1):13–19, 1980.

[18] BE Woodgate, EA Tandberg-Hanssen, EC Bruner, JM Beckers, JC Brandt, W Henze, CL Hyder, MW Kalet, PJ Kenny, EtD Knox, et al. The ultraviolet spectrometer and polarimeter on the solar maximum mission. *Solar Physics*, 65(1):73–90, 1980.

[19] N-E Raouafi, P Lemaire, and S Sahal-Bréchot. Detection of the o vi 103.2 nm line polarization by the sumer spectrometer on the soho spacecraft. *Astronomy and Astrophysics*, 345:999–1005, 1999.

[20] Kenneth H Nordsieck and Walter M Harris. Ultraviolet astronomical polarimetry: some results and prospects. In *Ultraviolet and X-Ray Detection, Spectroscopy, and Polarimetry III*, volume 3764, pages 124–133. International Society for Optics and Photonics, 1999.

[21] Edward A West, Jason G Porter, John M Davis, G Allen Gary, Douglas M Rabin, Roger J Thomas, and Joseph M Davila. Overview of the solar ultraviolet magnetograph investigation. In *Instrumentation for UV/EUV Astronomy and Solar Missions*, volume 4139, pages 350–361. International Society for Optics and Photonics, 2000.

[22] Silvano FINESCHI. Compass: proposta all'esa per la cosmic vision 2007. Technical report, OA Torino, 2008.

[23] Hardi Peter, L Abbo, V Andretta, F Auchère, A Bemporad, F Berrilli, V Bommier, A Braukhane, R Casini, W Curdt, et al. Solar magnetism explorer (solmex). *Experimental Astronomy*, 33(2-3):271–303, 2012.

[24] Ryouhei Kano, Takamasa Bando, Noriyuki Narukage, Ryoko Ishikawa, Saku Tsuneta, Yukio Katsukawa, Masahito Kubo, Shin-nosuke Ishikawa, Hirohisa Hara, Toshifumi Shimizu, et al. Chromospheric lyman-alpha spectro-polarimeter (clasp). In *Space Telescopes and Instrumentation 2012: Ultraviolet to Gamma Ray*, volume 8443, page 84434F. International Society for Optics and Photonics, 2012.

[25] Noriyuki Narukage, David E McKenzie, Ryoko Ishikawa, Javier Trujillo-Bueno, Bart De Pontieu, Masahito Kubo, Shin-nosuke Ishikawa, Ryouhei Kano, Yoshinori Suematsu, Masaki Yoshida, et al. Chromospheric layer spectropolarimeter (clasp2). In *Space Telescopes and Instrumentation 2016: Ultraviolet to Gamma Ray*, volume 9905, page 990508. International Society for Optics and Photonics, 2016.

[26] T. Saito, K. Ozaki, K. Fukui, H. Iwai, K. Yamamoto, H. Miyake, and K. Hiramatsu. Vacuum ultraviolet ellipsometer using inclined detector as analyzer to measure stokes parameters and optical constants — with results for aln optical constants. *Thin Solid Films*, 571:517 – 521, 2014. 6th International Conference on Spectroscopic Ellipsometry (ICSE-VI).

[27] B. Watts, L. Thomsen, and P.C. Dastoor. A simple polarimeter for quantifying synchrotron polarization. *Journal of Electron Spectroscopy and Related Phenomena*, 151(3):208 – 214, 2006.

[28] Clemens von Korff Schmising, David Weder, Tino Noll, Bastian Pfau, Martin Hennecke, Christian Strüber, Ilie Radu, Michael Schneider, Steffen Staeck, Christian M Günther, et al. Generating circularly polarized radiation in the extreme ultraviolet spectral range at the free-electron laser flash. *Review of Scientific Instruments*, 88(5):053903, 2017.

[29] Tetsuo Harada and Takeo Watanabe. Reflectance measurement of euv mirrors with s-and p-polarized light using polarization control units. In *International Conference on Extreme Ultraviolet Lithography 2018*, volume 10809, page 108091T. International Society for Optics and Photonics, 2018.

[30] Eléonore Roussel, Enrico Allaria, Carlo Callegari, Marcello Coreno, Riccardo Cucini, Simone Di Mitri, Bruno Diviacco, Eugenio Ferrari, Paola Finetti, David Gauthier, Giuseppe Penco, Lorenzo Raimondi, Cristian Svetina, Marco Zangrando, Andreas Beckmann, Leif Glaser, Gregor Hartmann, Frank Scholz, Joern Seltmann, Ivan Shevchuk, Jens Viefhaus, and Luca Giannessi. Roussel2017. *Photonics*, 4(2), 2017.

[31] Laurent Nahon and Christian Alcaraz. Su5: A calibrated variable-polarization synchrotron radiation beam line in the vacuum-ultraviolet range. *Appl Opt*, 43(5):1024–1037, 2004.

[32] P Finetti, E Allaria, B Diviacco, C Callegari, B Mahieu, J Viefhaus, M Zangrando, G De Ninno, G Lambert, E Ferrari, et al. Polarization measurement of free electron laser pulses in the vuv generated by the variable polarization source fermi. In *X-Ray Free-Electron Lasers: Beam Diagnostics, Beamline Instrumentation, and Applications II*, volume 9210, page 92100K. International Society for Optics and Photonics, 2014.

[33] Enrico Allaria, Bruno Diviacco, Carlo Callegari, Paola Finetti, Benoît Mahieu, Jens Viefhaus, Marco Zangrando, Giovanni De Ninno, Guillaume Lambert, Eugenio Ferrari, et al. Control of the polarization of a vacuum-ultraviolet, high-gain, free-electron laser. *Physical Review X*, 4(4):041040, 2014.

[34] Pierre-Marie Robitaille and Dmitri Rabounski. Polarized light from the sun: Unification of the corona and analysis of the second solar spectrum–further implications of a liquid metallic hydrogen solar model. *PROGRESS*, 11:236, 2015.

[35] Noriyuki Narukage, Masahito Kubo, Ryohko Ishikawa, Shin-nosuke Ishikawa, Yukio Katsukawa, Toshihiko Kobiki, Gabriel Giono, Ryouhei Kano, Takamasa Bando, Saku Tsuneta, et al. High-reflectivity coatings

for a vacuum ultraviolet spectropolarimeter. *Solar Physics*, 292(3):40, 2017.

[36] Silvano Fineschi, Richard B. Hoover, Juan M. Fontenla, and Arthur B. C. Walker II. Polarimetry of extreme ultraviolet lines in solar astronomy. *Optical Engineering*, 30(8):1161 – 1168, 1991.

[37] Jan Olof Stenflo. *Applications of the Hanle Effect in Solar Physics*, pages 237–281. Springer US, Boston, MA, 1991.

[38] S. Fineschi. Space-based Instrumentation for Magnetic Field Studies of Solar and Stellar Atmospheres. In G. Mathys, S. K. Solanki, and D. T. Wickramasinghe, editors, *Magnetic Fields Across the Hertzsprung-Russell Diagram*, volume 248 of *Astronomical Society of the Pacific Conference Series*, page 597, Jan 2001.

[39] S. Wilbrandt, O. Stenzel, H. Nakamura, D. Wulff-Molder, A. Duparré, and N. Kaiser. Protected and enhanced aluminum mirrors for the vuv. *Appl. Opt.*, 53(4):A125–A130, Feb 2014.

[40] C. Neiner, D. Baade, A. Fullerton, C. Gry, G. Hussain, A. Lèbre, J. Morin, P. Petit, J. O. Sundqvist, A. ud Doula, A. A. Vidotto, G. A. Wade, and The UVMag consortium. Uvmag: stellar formation, evolution, structure and environment with space uv and visible spectropolarimetry. *Astrophysics and Space Science*, 354(1):215–227, Nov 2014.

[41] Thomas Siefke, Stefanie Kroker, Kristin Pfeiffer, Oliver Puffky, Kay Dietrich, Daniel Franta, Ivan Ohlídal, Adriana Szeghalmi, Ernst-Bernhard Kley, and Andreas Tünnermann. Materials pushing the application limits of wire grid polarizers further into the deep ultraviolet spectral range. *Advanced Optical Materials*, 4(11):1780–1786, 2016.

[42] M Pancrazzi, F Landini, C Baccani, M Romoli, V Noce, M Focardi, C Casini, A Dinescu, G Adam, A Scippa, et al. Updates on the pencil project. *Nuovo Cimento C Geophysics Space Physics C*, 42, 2019.

[43] Juan I Larruquert, A Marco Malvezzi, Angelo Giglia, José A Aznárez, Luis Rodríguez-de Marcos, José A Méndez, Paolo Miotti, Fabio Frassetto, Giuseppe Massone, Stefano Nannarone, et al. Reflective and transmissive broadband coating polarizers in a spectral range centered at 121.6 nm. *Journal of Optics*, 16(12):125713, 2014.

[44] Juan I Larruquert, A Marco Malvezzi, Luis Rodríguez-de Marcos, Angelo Giglia, Nuria Gutiérrez-Luna, Lucía Espinosa-Yáñez, Carlos Honrado-Benítez, José A Aznárez, Giuseppe Massone, Gerardo Capobianco, et al. Polarizers tuned at key far-uv spectral lines for space instrumentation. In *EUV and X-ray Optics: Synergy between Laboratory and Space V*, volume 10235, page 102350K. International Society for Optics and Photonics, 2017.

[45] Luis V. Rodríguez De Marcos, Juan I. Larruquert, José A. Méndez, Nuria Gutiérrez-Luna, Lucía Espinosa-Yá nez, Carlos Honrado-Benítez, José Chavero-Royán, and Belén Perea-Abarca. Optimization of mgf2-deposition temperature for far uv al mirrors. *Opt. Express*, 26(7):9363–9372, Apr 2018.

[46] Juan I Larruquert, A Marco Malvezzi, Angelo Giglia, José A Aznárez, Luis Rodríguez-de Marcos, José A Méndez, Paolo Miotti, Fabio Frassetto, Giuseppe Massone, Gerardo Capobianco, et al. Polarizers for a spectral range centered at 121.6 nm operating by reflectance or by transmittance. In *EUV and X-ray Optics: Synergy between Laboratory and Space IV*, volume 9510, page 951008. International Society for Optics and Photonics, 2015.

[47] Françoise Bridou, Mireille Cuniot-Ponsard, J-M Desvignes, Alexander Gottwald, Udo Kroth, and Mathias Richter. Polarizing and non-polarizing mirrors for the hydrogen lyman-α radiation at 121.6 nm. *Applied Physics A*, 102(3):641–649, 2011.

[48] Jongmin Kim, Muamer Zukic, Michele M Wilson, and Douglas G Torr. Design and fabrication of a reflection far-ultraviolet polarizer and retarder. In *X-Ray and Ultraviolet Polarimetry*, volume 2010, pages 93–103. International Society for Optics and Photonics, 1994.

[49] Luis V. Rodríguez De Marcos, Juan I. Larruquert, José A. Méndez, Manuela Vidal-Dasilva, Sergio García-Cortés, Nuria Gutiérrez-Luna, Lucía Espinosa-Yá nez, Carlos Honradobenítez, and José Chavero-Royán. Lyman-β narrowband coatings with strong lyman-α rejection. *Opt. Express*, 26(19):25166–25177, Sep 2018.

[50] J. I. Larruquert, L. V. Rodríguez de Marcos, J. A. Méndez, P. J. Martin, and A. Bendavid. High reflectance ta-c coatings in the extreme ultraviolet. *Opt. Express*, 21(23):27537–27549, Nov 2013.

[51] Minghong Yang. Yang2007. *JOURNAL OF OPTICS A: PURE AND APPLIED OPTICS*, 9, 2007.

[52] Gillian Black, Xiaoyu Cui, Sergey Gorovikov, Feizhu He, Grant Henneberg, Michael A MacDonald, Brian Yates, and Lucia Zuin. Euv stokes reflection polarimeter using gold coated mirrors for use up to 150 ev photon energy. In *Advances in Metrology for X-Ray and EUV Optics VIII*, volume 11109, page 111090G. International Society for Optics and Photonics, 2019.

[53] MD Neumann, C Cobet, H Kaser, M Kolbe, A Gottwald, M Richter, and N Esser. A synchrotron-radiation-based variable angle ellipsometer for the visible to vacuum ultraviolet spectral range. *Review of Scientific Instruments*, 85(5):055117, 2014.

[54] Shirly Espinoza, Fabio Samparisi, Fabio Frassetto, Steffen Richter, Mateusz Rebarz, Ondrej Finke, Martin Albrecht, Matej Jurkovic, Ondrej Hort, Nicola Fabris, et al. Characterization of the high harmonics source for the vuv ellipsometer at eli beamlines. *Journal of Vacuum Science & Technology B, Nanotechnology and Microelectronics: Materials, Processing, Measurement, and Phenomena*, 38(2):024005, 2020.

[55] John M Papalia, Douglas H Adamson, Paul M Chaikin, and Richard A Register. Silicon nanowire polarizers for far ultraviolet (sub-200 nm) applications: Modeling and fabrication. *Journal of Applied Physics*, 107(8):084305, 2010.

[56] D.Y. Smith, E Shiles, and Mitio Inokuti. The optical properties of metallic aluminum. In Edward D. Palik, editor, *Handbook of Optical Constants of Solids*, pages 369 – 406. Academic Press, Burlington, 1997.

[57] Luis V. Rodríguez de Marcos, Juan I. Larruquert, José A. Méndez, and José A. Aznárez. Self-consistent optical constants of mgf2, laf3, and cef3 films. *Opt. Mater. Express*, 7(3):989–1006, Mar 2017.

[58] Luis V Rodríguez-de Marcos, Juan I Larruquert, José A Méndez, and José A Aznárez. Self-consistent optical constants of sio 2 and ta 2 o 5 films. *Optical Materials Express*, 6(11):3622–3637, 2016.

[59] Daniel Franta, David Nečas, and Ivan Ohlídal. Universal dispersion model for characterization of optical thin films over a wide spectral range: application to hafnia. *Appl. Opt.*, 54(31):9108–9119, Nov 2015.

[60] D Palik Edward and I Palik. Handbook of optical constants of solids, 1985.

[61] Douglas C Montgomery. Design and analysis of experiments. ed. *John Wiley & Sons*, 52:218–286, 2001.

[62] Jianlong Wang and Wei Wan. Application of desirability function based on neural network for optimizing biohydrogen production process. *International Journal of Hydrogen Energy*, 34(3):1253–1259, 2009.

[63] Ful-Chiang Wu. Optimization of correlated multiple quality characteristics using desirability function. *Quality engineering*, 17(1):119–126, 2004.

[64] Jian Jim Wang, Lei Chen, Xiaoming Liu, Paul Sciortino, Feng Liu, Frank Walters, and Xuegong Deng. 30-nm-wide aluminum nanowire grid for ultrahigh contrast and transmittance polarizers made by uv-nanoimprint lithography. *Applied physics letters*, 89(14):141105, 2006.

[65] Jian Jim Wang, Frank Walters, Xiaoming Liu, Paul Sciortino, and Xuegong Deng. High-performance, large area, deep ultraviolet to infrared polarizers based on 40 nm line/78 nm space nanowire grids. *Applied physics letters*, 90(6):061104, 2007.

[66] Fantao Meng, Gang Luo, Ivan Maximov, Lars Montelius, Jinkui Chu, and Hongqi Xu. Fabrication and characterization of bilayer metal wire-grid polarizer using nanoimprint lithography on flexible plastic substrate. *Microelectronic Engineering*, 88(10):3108–3112, 2011.

[67] Earl E Scime, Erik H Anderson, David J McComas, and Mark L Schattenburg. Extreme-ultraviolet polarization and filtering with gold transmission gratings. *Applied optics*, 34(4):648–654, 1995.

[68] Seh-Won Ahn, Ki-Dong Lee, Jin-Sung Kim, Sang Hoon Kim, Joo-Do Park, Sarng-Hoon Lee, and Phil-Won Yoon. Fabrication of a 50 nm half-pitch wire grid polarizer using nanoimprint lithography. *Nanotechnology*, 16(9):1874, 2005.

[69] RR Kunz, M Rothschild, and MS Yeung. Large-area patterning of 50 nm structures on flexible substrates using near-field 193 nm radiation. *Journal of Vacuum Science & Technology B: Microelectronics and Nanometer Structures Processing, Measurement, and Phenomena*, 21(1):78–81, 2003.

[70] D. J. Resnick, W. J. Dauksher, D. Mancini, K. J. Nordquist, T. C. Bailey, S. Johnson, N. Stacey, J. G. Ekerdt, C. G. Willson, and S. V. Sreenivasan. Imprint lithography for integrated circuit fabrication. *Journal of Vacuum Science & Technology B Microelectronics & Nanometer Structures*, 21(21):2624 – 2631, 2003.

[71] Clark Pentico, Eric Gardner, Douglas Hansen, and Ray Perkins. 52.4: New, high performance, durable polarizers for projection displays. In *SID Symposium Digest of Technical Papers*, volume 32, pages 1287–1289. Wiley Online Library, 2001.

[72] Feng Hua, Yugang Sun, Anshu Gaur, Matthew A Meitl, Lise Bilhaut, Lolita Rotkina, Jingfeng Wang, Phil Geil, Moonsub Shim, John A Rogers, et al. Polymer imprint lithography with molecular-scale resolution. *Nano letters*, 4(12):2467–2471, 2004.

[73] Xiaoming Liu, Xuegong Deng, Paul Sciortino, Mike Buonanno, Frank Walters, Ron Varghese, Joel Bacon, Lei Chen, Nada O'Brie, and Jian Jim Wang. Large area, 38 nm half-pitch grating fabrication by using atomic spacer lithography from aluminum wire grids. *Nano letters*, 6(12):2723–2727, 2006.

[74] Vincent Pelletier, Koji Asakawa, Mingshaw Wu, Douglas H Adamson, Richard A Register, and Paul M Chaikin. Aluminum nanowire polarizing grids: Fabrication and analysis. *Applied physics letters*, 88(21):211114, 2006.

[75] Daniel Fan and Yasin Ekinci. Photolithography reaches 6 nm half-pitch using extreme ultraviolet light. *Journal of Micro/Nanolithography, MEMS, and MOEMS*, 15(3):033505, 2016.

[76] Stanislaw Chwirot, Síle Nic Chormaic, Darek Dziczek, and James Slevin. Efficient polarization analyzer for lyman α radiation. *Applied optics*, 32(9):1583–1589, 1993.

[77] Jongmin Kim, Muamer Zukic, and Douglas G Torr. Multilayer thin-film design as far-ultraviolet polarizers. In *Multilayer and Grazing Incidence X-Ray/EUV Optics for Astronomy and Projection Lithography*, volume 1742, pages 413–422. International Society for Optics and Photonics, 1993.

[78] M Casti, S Fineschi, G Capobianco, F Landini, M Romoli, E Antonucci, V Andretta, G Naletto, G Nicolini, D Spadaro, et al. Calibration of the liquid crystal visible-light polarimeter for the metis/solar orbiter coronagraph. In *Space Telescopes and Instrumentation 2018: Optical, Infrared, and Millimeter Wave*, volume 10698, page 1069831. International Society for Optics and Photonics, 2018.

[79] Tymon Barwicz, Michael R Watts, Miloš A Popović, Peter T Rakich, Luciano Socci, Franz X Kärtner, Erich P Ippen, and Henry I Smith. Polarization-transparent microphotonic devices in the strong confinement limit. *Nature Photonics*, 1(1):57–60, 2007.

[80] Leiming Wu, Jun Guo, Hailin Xu, Xiaoyu Dai, and Yuanjiang Xiang. Ultrasensitive biosensors based on long-range surface plasmon polariton and dielectric waveguide modes. *Photonics Research*, 4(6):262–266, 2016.

[81] Joshua W Silverstone, Damien Bonneau, Kazuya Ohira, Nob Suzuki, Haruhiko Yoshida, Norio Iizuka, Mizunori Ezaki, Chandra M Natarajan, Michael G Tanner, Robert H Hadfield, et al. On-chip quantum interference between silicon photon-pair sources. *Nature Photonics*, 8(2):104–108, 2014.

[82] Xiaoping Liu, Richard M Osgood, Yurii A Vlasov, and William MJ Green. Mid-infrared optical parametric amplifier using silicon nanophotonic waveguides. *Nature Photonics*, 4(8):557–560, 2010.

[83] Daoxin Dai, Liu Liu, Shiming Gao, Dan-Xia Xu, and Sailing He. Polarization management for silicon photonic integrated circuits. *Laser & Photonics Reviews*, 7(3):303–328, 2013.

[84] Daoxin Dai, Liu Liu, Lech Wosinski, and SAHS He. Design and fabrication of ultra-small overlapped awg demultiplexer based on/spl alpha/-si nanowire waveguides. *Electronics Letters*, 42(7):400–402, 2006.

[85] Ying Huang, Shiyang Zhu, Huijuan Zhang, Tsung-Yang Liow, and Guo-Qiang Lo. Cmos compatible horizontal nanoplasmonic slot waveguides te-pass polarizer on silicon-on-insulator platform. *Optics express*, 21(10):12790–12796, 2013.

[86] Humaira Zafar, Mutasem Odeh, Anatol Khilo, and Marcus S Dahlem. Low-loss broadband silicon tm-pass polarizer based on periodically structured waveguides. *IEEE Photonics Technology Letters*, 32(17):1029–1032, 2020.

[87] Chyong-Hua Chen, Lin Pang, Chia-Ho Tsai, Uriel Levy, and Yeshaiahu Fainman. Compact and integrated tm-pass waveguide polarizer. *Optics Express*, 13(14):5347–5352, 2005.

[88] Fan Zhang, Han Yun, Yun Wang, Zeqin Lu, Lukas Chrostowski, and Nicolas AF Jaeger. Compact broadband polarization beam splitter using a symmetric directional coupler with sinusoidal bends. *Optics Letters*, 42(2):235–238, 2017.

[89] Xiao Sun, J Stewart Aitchison, and Mo Mojahedi. Realization of an ultra-compact polarization beam splitter using asymmetric mmi based on silicon nitride/silicon-on-insulator platform. *Optics Express*, 25(7):8296–8305, 2017.

[90] Dong Wook Kim, Moon Hyeok Lee, Yudeuk Kim, and Kyong Hon Kim. Planar-type polarization beam splitter based on a bridged silicon waveguide coupler. *Optics Express*, 23(2):998–1004, 2015.

[91] Jian Wang, Di Liang, Yongbo Tang, Daoxin Dai, and John E Bowers. Realization of an ultra-short silicon polarization beam splitter with an asymmetrical bent directional coupler. *Optics letters*, 38(1):4–6, 2013.

[92] Liu Liu, Yunhong Ding, Kresten Yvind, and Jørn M Hvam. Silicon-on-insulator polarization splitting and rotating device for polarization diversity circuits. *Optics express*, 19(13):12646–12651, 2011.

[93] Linfei Gao, Yijie Huo, Kai Zang, Seonghyun Paik, Yusi Chen, James S Harris, and Zhiping Zhou. On-chip plasmonic waveguide optical waveplate. *Scientific reports*, 5(1):1–6, 2015.

[94] Daoxin Dai and Hao Wu. Realization of a compact polarization splitter-rotator on silicon. *Optics letters*, 41(10):2346–2349, 2016.

[95] Daigao Chen, Xi Xiao, Lei Wang, Wen Liu, Qi Yang, and Shaohua Yu. Highly efficient silicon optical polarization rotators based on mode order conversions. *Optics letters*, 41(5):1070–1073, 2016.

[96] Daoxin Dai, Zhi Wang, Nick Julian, and John E Bowers. Compact broadband polarizer based on shallowly-etched silicon-on-insulator ridge optical waveguides. *Optics express*, 18(26):27404–27415, 2010.

[97] Xiaowei Guan, Pengxin Chen, Sitao Chen, Peipeng Xu, Yaocheng Shi, and Daoxin Dai. Low-loss ultracompact transverse-magnetic-pass polarizer with a silicon subwavelength grating waveguide. *Optics letters*, 39(15):4514–4517, 2014.

[98] Yule Xiong, Dan-Xia Xu, Jens H Schmid, Pavel Cheben, and N Ye Winnie. High extinction ratio and broadband silicon te-pass polarizer using subwavelength grating index engineering. *IEEE Photonics Journal*, 7(5):1–7, 2015.

[99] Zhoufeng Ying, Guanghui Wang, Xuping Zhang, Ying Huang, Ho-Pui Ho, and Yixin Zhang. Ultracompact te-pass polarizer based on a hybrid plasmonic waveguide. *IEEE Photonics Technology Letters*, 27(2):201–204, 2014.

[100] Tien Khee Ng, Mohammed Zahed Mustafa Khan, Ahmad Al-Jabr, and Boon S Ooi. Analysis of cmos compatible cu-based tm-pass optical polarizer. *IEEE Photonics Technology Letters*, 24(9):724–726, 2012.

[101] Jing Wang, Minghao Qi, Yi Xuan, Haiyang Huang, You Li, Ming Li, Xin Chen, Qi Jia, Zhen Sheng, Aimin Wu, et al. Proposal for fabrication-tolerant soi polarization splitter-rotator based on cascaded mmi couplers and an assisted bi-level taper. *Optics express*, 22(23):27869–27879, 2014.

[102] Bin Ni and Jinbiao Xiao. Plasmonic-assisted te-pass polarizer for silicon-based slot waveguides. *IEEE Photonics Technology Letters*, 30(5):463–466, 2018.

[103] Bin Ni and Jinbiao Xiao. A compact silicon-based te-pass polarizer using three-guide directional couplers. *IEEE Photonics Technology Letters*, 29(19):1631–1634, 2017.

[104] Hang Guan, Ari Novack, Matthew Streshinsky, Ruizhi Shi, Qing Fang, Andy Eu-Jin Lim, Guo-Qiang Lo, Tom Baehr-Jones, and Michael Hochberg. Cmos-compatible highly efficient polarization splitter and rotator based on a double-etched directional coupler. *Optics express*, 22(3):2489–2496, 2014.

[105] MZ Alam, J Stewart Aitchison, and M Mojahedi. Compact and silicon-on-insulator-compatible hybrid plasmonic te-pass polarizer. *Optics letters*, 37(1):55–57, 2012.

[106] Jin Tae Kim and Choon-Gi Choi. Graphene-based polymer waveguide polarizer. *Optics express*, 20(4):3556–3562, 2012.

[107] Chunying Guan, Shuqiang Li, Yize Shen, Tingting Yuan, Jing Yang, and Libo Yuan. Graphene-coated surface core fiber polarizer. *Journal of Lightwave Technology*, 33(2):349–353, 2015.

[108] Xiang Yin, Xianmin Ke, Lin Chen, Tian Zhang, Junhao Li, Zhongshu Zhu, and Xun Li. Ultra-broadband te-pass polarizer using a cascade of multiple few-layer graphene embedded silicon waveguides. *Journal of Lightwave Technology*, 34(13):3181–3187, 2016.

[109] Qiaoliang Bao, Han Zhang, Bing Wang, Zhenhua Ni, Candy Haley Yi Xuan Lim, Yu Wang, Ding Yuan Tang, and Kian Ping Loh. Broadband graphene polarizer. *Nature photonics*, 5(7):411–415, 2011.

[110] L Sánchez, S Lechago, and P Sanchis. Ultra-compact te and tm pass polarizers based on vanadium dioxide on silicon. *Optics Letters*, 40(7):1452–1455, 2015.

[111] Shijie Zhang, Zongwen Li, and Fei Xing. Review of polarization optical devices based on graphene materials. *International journal of molecular sciences*, 21(5):1608, 2020.

[112] Santiago García-Cuevas Carrillo, Geoffrey R Nash, Hasan Hayat, Martin J Cryan, Maciej Klemm, Harish Bhaskaran, and C David Wright. Design of practicable phase-change metadevices for near-infrared absorber and modulator applications. *Optics express*, 24(12):13563–13573, 2016.

[113] Nathaniel Kinsey, Marcello Ferrera, Gururaj V Naik, VE Babicheva, Vladimir M Shalaev, and Alexandra Boltasseva. Experimental demonstration of titanium nitride plasmonic interconnects. *Optics express*, 22(10):12238–12247, 2014.

[114] Shaimaa I Azzam and SSA Obayya. Titanium nitride-based cmos-compatible te-pass and tm-pass plasmonic polarizers. *IEEE Photonics Technology Letters*, 28(3):367–370, 2015.

[115] Bob Hasenick. The increasing importance of extinction ratio in telecommunications. *lightwaveonline. com (October 2005)*, 2018.

[116] Calvin D Salzberg and John J Villa. Infrared refractive indexes of silicon germanium and modified selenium glass. *JOSA*, 47(3):244–246, 1957.

[117] CZ Tan. Determination of refractive index of silica glass for infrared wavelengths by ir spectroscopy. *Journal of Non-Crystalline Solids*, 223(1-2):158–163, 1998.

[118] Gururaj V Naik, Vladimir M Shalaev, and Alexandra Boltasseva. Alternative plasmonic materials: beyond gold and silver. *Advanced Materials*, 25(24):3264–3294, 2013.

[119] Lukas Chrostowski and Michael Hochberg. *Silicon photonics design: from devices to systems*. Cambridge University Press, 2015.

[120] Chenlei Li and Daoxin Dai. Compact polarization beam splitter for silicon photonic integrated circuits with a 340-nm-thick silicon core layer. *Optics Letters*, 42(21):4243–4246, 2017.

[121] Yawen Huang, Zhao Tu, Xuaxiang Yi, Yanping Li, and Xingjun Wang. Polarization beam splitter based on cascaded step-size multimode interference coupler. *Optical Engineering*, 52(7):077103, 2013.

[122] Lu Liu, Qingzhong Deng, and Zhiping Zhou. Manipulation of beat length and wavelength dependence of a polarization beam splitter using a sub-wavelength grating. *Optics letters*, 41(21):5126–5129, 2016.

[123] Bowen Bai, Lu Liu, Ruixuan Chen, and Zhiping Zhou. Low loss, compact tm-pass polarizer based on hybrid plasmonic grating. *IEEE Photonics Technology Letters*, 29(7):607–610, 2017.

[124] Shengbao Wu, Jinxin Hao, Zhicheng Zhao, and X Steve Yao. Low loss and high extinction ratio all-silicon tm-pass polarizer with reflection removal enabled by contra-mode conversion bragg-gratings. *Optics Express*, 29(17):27640–27652, 2021.

[125] Md Ghulam Saber, David V Plant, and Nicolás Abadía. Broadband all-silicon hybrid plasmonic tm-pass polarizer using bend waveguides. *AIP Advances*, 11(4):045219, 2021.

[126] Zhengying Xu, Tao Lyu, and Xiaohan Sun. Interleaved subwavelength gratings strip waveguide based tm pass polarizer on soi platform. *IEEE Photonics Journal*, 12(2):1–10, 2020.

[127] Ruixuan Chen, Bowen Bai, and Zhiping Zhou. Low-loss hybrid plasmonic tm-pass polarizer using polarization-dependent mode conversion. *Photonics Research*, 8(7):1197–1202, 2020.

[128] Md Ghulam Saber, Nicolás Abadía, and David V Plant. Cmos compatible all-silicon tm pass polarizer based on highly doped silicon waveguide. *Optics express*, 26(16):20878–20887, 2018.

[129] Xiao Hu and Jian Wang. Ultrabroadband compact graphene–silicon tm-pass polarizer. *IEEE Photonics Journal*, 9(2):1–10, 2017.

[130] Dong Wook Kim, Moon Hyeok Lee, Yudeuk Kim, and Kyong Hon Kim. Ultracompact transverse magnetic mode-pass filter based on one-dimensional photonic crystals with subwavelength structures. *Optics express*, 24(19):21560–21565, 2016.

[131] Jingjing Zhang, Junbo Yang, Linmei Liang, and Wenjun Wu. Broadband tm-mode-pass polarizer and polarization beam splitter using asymmetrical directional couplers based on silicon subwavelength grating. *Optics Communications*, 407:46–50, 2018.

[132] Ahmed El-Sayed Abd-Elkader, Mohamed Farhat O Hameed, Nihal FF Areed, Hossam El-Din Mostafa, and Salah SA Obayya. Ultracompact azo-based te-pass and tm-pass hybrid plasmonic polarizers. *JOSA B*, 36(3):652–661, 2019.

[133] Nikhil Dhingra and Francesco Dell'Olio. Ultralow loss and high extinction ratio tm-pass polarizer in silicon photonics. *IEEE Photonics Journal*, 12(6):1–11, 2020.

[134] Chandra Prakash and Mrinal Sen. Optimization of silicon-photonic crystal (phc) waveguide for a compact and high extinction ratio tm-pass polarization filter. *Journal of Applied Physics*, 127(2):023101, 2020.

[135] Shuai Yuan, Yi Wang, Qingzhong Huang, Jinsong Xia, and Jinzhong Yu. Ultracompact tm-pass/te-reflected integrated polarizer based on a hybrid plasmonic waveguide for silicon photonics. In *11th International Conference on Group IV Photonics (GFP)*, pages 183–184. IEEE, 2014.

[136] Wen Zhou, Yeyu Tong, Xiankai Sun, and Hon Ki Tsang. Ultra-broadband hyperuniform disordered silicon photonic polarizers. *IEEE Journal of Selected Topics in Quantum Electronics*, 26(2):1–9, 2019.

[137] Xiaowei Guan, Peipeng Xu, Yaocheng Shi, and Daoxin Dai. Ultracompact broadband tm-pass polarizer using a silicon hybrid plasmonic waveguide grating. In *Asia Communications and Photonics Conference*, pages ATh4A–2. Optical Society of America, 2013.

[138] Bowen Bai, Fenghe Yang, and Zhiping Zhou. Demonstration of an on-chip te-pass polarizer using a silicon hybrid plasmonic grating. *Photonics Research*, 7(3):289–293, 2019.

[139] Shankar Kumar Selvaraja, Patrick Jaenen, Wim Bogaerts, Dries Van Thourhout, Pieter Dumon, and Roel Baets. Fabrication of photonic wire and crystal circuits in silicon-on-insulator using 193-nm optical lithography. *Journal of lightwave technology*, 27(18):4076–4083, 2009.

[140] SBS Heil, E Langereis, F Roozeboom, MCM Van De Sanden, and WMM Kessels. Low-temperature deposition of tin by plasma-assisted atomic layer deposition. *Journal of the Electrochemical Society*, 153(11):G956, 2006.

[141] Mikko Ritala, Markku Leskelä, Jan-Pieter Dekker, Cees Mutsaers, Pekka J Soininen, and Jarmo Skarp. Perfectly conformal tin and al2o3 films deposited by atomic layer deposition. *Chemical Vapor Deposition*, 5(1):7–9, 1999.

[142] Shankar Kumar Selvaraja. *Wafer-scale fabrication technology for silicon photonic integrated circuits*. PhD thesis, PhD thesis, Ghent University, 2011.

[143] Yuichiro Tanushi, Tomohiro Kita, Munehiro Toyama, Miyoshi Seki, Keiji Koshino, Nobuyuki Yokoyama, Minoru Ohtsuka, Akinobu Sugiyama, Ei-ichi Ishitsuka, Tsukuru Sano, et al. Uniform characteristics of si-wire waveguide devices fabricated on 300 mm soi wafers by using arf immersion lithography. In *10th International Conference on Group IV Photonics*, pages 105–106. IEEE, 2013.

[144] Shankar Kumar Selvaraja, Wim Bogaerts, Pieter Dumon, Dries Van Thourhout, and Roel Baets. Subnanometer linewidth uniformity in silicon nanophotonic waveguide devices using cmos fabrication technology. *IEEE Journal of Selected Topics in Quantum Electronics*, 16(1):316–324, 2009.

[145] X-A Zhao, E Kolawa, and M-A Nicolet. Reaction of thin metal films with crystalline and amorphous al2o3. *Journal of Vacuum Science & Technology A: Vacuum, Surfaces, and Films*, 4(6):3139–3141, 1986.

[146] M Muralidhar Singh, G Vijaya, MS Krupashankara, BK Sridhara, and TN Shridhar. Deposition and characterization of aluminium thin film coatings using dc magnetron sputtering process. *Materials Today: Proceedings*, 5(1):2696–2704, 2018.

[147] Luis V Rodríguez De Marcos, Juan I Larruquert, José A Méndez, Nuria Gutiérrez-Luna, Lucía Espinosa-Yáñez, Carlos Honrado-Benítez, José Chavero-Royán, and Belén Perea-Abarca. Optimization of mgf 2-deposition temperature for far uv al mirrors. *Optics express*, 26(7):9363–9372, 2018.

[148] Tero Pilvi, Timo Hatanpää, Esa Puukilainen, Kai Arstila, Martin Bischoff, Ute Kaiser, Norbert Kaiser, Markku Leskelä, and Mikko Ritala. Study of a novel ald process for depositing mgf 2 thin films. *Journal of Materials Chemistry*, 17(48):5077–5083, 2007.

[149] M. H. Habibi, N. Talebian, and J. H. Choi. The effect of annealing on photocatalytic properties of nanostructured titanium dioxide thin films. *Dyes & Pigments*, 73(1):103–110, 2007.

[150] C. J. Tavares, J. Vieira, L. Rebouta, G. Hungerford, P. Coutinho, V. Teixeira, J. O. Carneiro, and A. J. Fernandes. Reactive sputtering deposition of photocatalytic tio2 thin films on glass substrates. *Materials Science and Engineering B*, 138(2):139–143, 2007.

[151] Kai-Erik Elers, Jerry Winkler, Keith Weeks, and Steven Marcus. Ticl4 as a precursor in the tin deposition by ald and peald. *Journal of the Electrochemical society*, 152(8):G589, 2005.

[152] Bogart and K. Ha. Plasma enhanced chemical vapor deposition of sio2 using novel alkoxysilane precursors. *Journal of Vacuum Science & Technology A: Vacuum, Surfaces, and Films*, 13(2):476–480, 1995.

[153] Mewael Giday Sertsu. Development and metrology of extreme ultraviolet and soft x-ray multilayer mirrors. 2016.

[154] LF Burlaga. Magnetic fields and plasmas in the inner heliosphere: Helios results. *Planetary and Space Science*, 49(14-15):1619–1627, 2001.

[155] Peter Sigmund. Theory of sputtering. i. sputtering yield of amorphous and polycrystalline targets. *Physical review*, 184(2):383, 1969.

[156] Fabrication facility. Laboratory of microfabrication, institute of physics, cas. `http://lmf.iphy.ac.cn/instruments.php`.

[157] Saleem Hashmi. *Comprehensive materials processing*. Newnes, 2014.

[158] Hans-Jürgen Butt, Karlheinz Graf, and Michael Kappl. *Physics and chemistry of interfaces*. John Wiley & Sons, 2013.

[159] David Attwood. *Soft x-rays and extreme ultraviolet radiation: principles and applications*. Cambridge university press, 2000.

[160] B.J. Rice. 2 - extreme ultraviolet (euv) lithography. In Martin Feldman, editor, *Nanolithography*, pages 42–79. Woodhead Publishing, 2014.

[161] Ramish Zafar. Tsmc's true euv lithography will be on n5 node for 2x transistor density. `https://wccftech.com/tsmc-5nm-7nm-fabrication-details`, 2019. Aug 18, 2019.

[162] Nassir Mojarad, Jens Gobrecht, and Yasin Ekinci. Interference lithography at euv and soft x-ray wavelengths: Principles, methods, and applications. *Microelectronic Engineering*, 143:55–63, 2015.

[163] Artak Isoyan, Yang-Chun Cheng, Fan Jiang, John Wallace, Mikhail Efremov, Paul Nealey, and Franco Cerrina. Progress in extreme ultraviolet interferometric lithography at the university of wisconsin. In *Emerging Lithographic Technologies XII*, volume 6921, page 69212R. International Society for Optics and Photonics, 2008.

[164] Li Wang, Daniel Fan, Vitaliy A Guzenko, and Yasin Ekinci. Facile fabrication of high-resolution extreme ultraviolet interference lithography grating masks using footing strategy during electron beam writing. *Journal of Vacuum Science & Technology B, Nanotechnology and Microelectronics: Materials, Processing, Measurement, and Phenomena*, 31(6):06F602, 2013.

[165] Tatsuo Ishijima, Kohei Nosaka, Yasunori Tanaka, Yoshihiko Uesugi, Yousuke Goto, and Hideo Horibe. A high-speed photoresist removal process using multibubble microwave plasma under a mixture of multiphase plasma environment. *Applied Physics Letters*, 103(14):142101, 2013.